Order Number 9230478

A numerical study of mixed and forced convection in a vertical packed tube and a packed channel

Chowdhury, Ashrafuddin, Ph.D.

University of Hawaii, 1992

U·M·I

300 N. Zeeb Rd.
Ann Arbor, MI 48106

A NUMERICAL STUDY OF MIXED AND FORCED CONVECTION IN A VERTICAL PACKED TUBE AND A PACKED CHANNEL

A DISSERTATION SUBMITTED TO THE GRADUATE DIVISION OF THE UNIVERSITY OF HAWAII IN PARTIAL FULFILLMENT OF THE REQUIREMENTS FOR THE DEGREE OF

DOCTOR OF PHILOSOPHY

IN

MECHANICAL ENGINEERING

MAY 1992

By

Ashrafuddin Chowdhury

Dissertation Committee :

Ping Cheng, Chairperson
Hi Chang Chai
Deane H. Kihara
Junku Yuh
Charles L. Bretschneider

ABSTRACT

A detailed numerical investigation has been performed for forced and mixed convection in a vertical channel and a cylindrical tube filled with a fluid-saturated porous medium, with particular emphasis on the developing region. The uniform wall temperature boundary condition has been assumed. The full momentum equations derived by Hsu and Cheng have been used, which accounts for variable porosity and permeability as well as viscous and inertia effects. A modification has been proposed to the dispersion conductivity model given by Hsu and Cheng, to take into account the ratio of the particle diameter to the characteristic length of the problem.

An expression that accounts for the variation of porosity in the streamwise and cross-stream directions has been introduced to take into account the variation of porosity near the walls, entrance and the exit sections. The empirical constants N, C_1 and φ_a, in the porosity function, and the Ergun constants A and B, in the permeability expression, have been determined by a comparison of the numerical and observed data for the pressure drop in a packed tube.

The predicted hydrodynamic entrance length has been found to be 10 to 20 particle diameters long for $0.024 \leq \gamma \leq 0.097$ and $1 \leq Re_d \leq 10^3$ (where γ is the ratio of the particle to the tube diameter and Re_d is the Reynolds number based on the particle diameter, d_p), with the shorter length corresponding to the smaller particle size. For all

practical purpose the entrance length can be considered to be about the size of the diameter of the tube (or the plate separation distance).

The empirical constants C_d and ω in the proposed dispersion model have been determined by comparing the predicted and observed heat flux data. The proposed porosity function with the present dispersion model have been found to predict the observed heat flux data of the air/glass sphere system to within 10% for $0.06 \leq \gamma \leq 0.12$ and $10^3 \leq Re_D \leq 2 \times 10^4$ (where Re_D is the Reynolds number based on the tube diameter, D) for the packed tube. For the air/chrome steel sphere system ($\gamma = 0.12$ and 0.14, $10^3 \leq Re_D \leq 2 \times 10^4$) the agreement was within 19%. The higher error in this case has been attributed to the large difference between the thermal conductivities of air and chrome steel, in which case the thermal equilibrium assumption invoked in the derivation of the energy equation may not be applicable. For the packed channel geometry ($\gamma = 0.06$ and 0.12 for the Freon/glass sphere system and $\gamma = 0.125$ for the Freon/chrome steel sphere system, $2 \times 10^3 \leq Re_D \leq 2 \times 10^4$) the agreement between the observed and calculated heat flux was within 20%, the discrepancy being due to improper experimentation and variable property effects of the fluid next to the heated surface which was not taken into account in the numerical simulation. The volume averaged method that is used to derive the governing equations has been found to be applicable to problems in which $\gamma \leq 0.15$.

The effect of using a fluid with a higher Prandlt number or a solid with a larger thermal conductivity has been observed to enhance heat transfer at high and low flow rates respectively. The exact values of the Reynolds number at which the above

mentioned enhancement takes place was found to be dependent on the Prandlt number of the saturating fluid.

Finally, it has been predicted in this study that the buoyancy force would play an important role in the heat transfer process for the air/glass sphere system with $\gamma = 0.06$, if $Gr_D/Re_D > 9 \times 10^5$ for the packed tube and $Gr_H/Re_H > 9 \times 10^4$ for the packed channel configuration.

TABLE OF CONTENTS

LIST OF TABLES

LIST OF FIGURES

LIST OF SYMBOLS

A, B	Ergun constants, Eq. (2.3)
C_a, C_b	Constants in Eq. (2.17)
C_d	Empirical constants in Eq. (1.8)
C_d'	Empirical constant in Eq. (1.7)
C_{form}	Influence coefficient of deformation factor for the conduction fraction, Eq. (1.6)
C_1, C_2	Empirical constants in Eq. (1.5)
d_p	Particle diameter
D	Tube diameter
f	Inertia coefficient, Eq. (2.3b)
F	Dimensionless inertia coefficient
g	Gravitational acceleration
Gr	Grashofs number based on tube radius
H	Plate separation distance
k	Permeability, Eq. (2.3a)
K	Dimensionless permeability
k_d	Dispersion thermal conductivity
k_e	Effective thermal conductivity
k_{ea}	Effective axial thermal conductivity
k_{et}	Effective transverse thermal conductivity
k_f	Thermal conductivity of the fluid phase

k_p	Thermal conductivity of the solid phase
k_s	Stagnant thermal conductivity
l	Dispersive length in Eq. (1.9)
L	length of the packed test section
L_{hy}	Dimensionless hydrodynamic entrance length (= L / d_p)
L_{th}	Dimensionless thermal entrance length (= L / d_p)
N	Empirical constant in Eq. (1.5)
Nu_{DX}, Nu_D	Local and average Nusselt number respectively based on tube diameter
Nu_{HX}, Nu_H	Local and average Nusselt number respectively based on plate separation distance
p_f	Volume averaged fluid pressure
P	Dimensionless pressure
Pe	Peclet number
Pr	Prandlt number
q_{wx}	Local wall heat flux
r	Radial coordinate
r_0	Tube radius
Re_d	Reynolds number based on particle diameter
Re_D	Reynolds number based on tube diameter
Re_H	Reynolds number based on plate separation distance
S	Deformation factor in Eq. (1.6)
t	Temperature

T	Dimensionless temperature
$\bar{u}$	Velocity vector
u	Streamwise velocity component
U	Dimensionless streamwise velocity component
v	Cross-stream velocity component
V	Dimensionless cross-stream velocity component
x, X	Streamwise dimensional and dimensionless coordinates
y, Y	Cross-stream dimensional and dimensionless coordinates

Greek symbols

β	Coefficient of volumetric expansion
γ	Ratio of particle to characteristic length
ρ	Fluid density
μ	Viscosity
ν	Kinematic viscosity
φ	Porosity
Φ	Normalized porosity ($= \varphi / \varphi_a$)
η	Transformed streamwise coordinate in Eq. (3.14)
χ	Transformed cross-stream coordinate in Eq. (3.13)
λ	Ratio of fluid to solid thermal conductivity ($= k_f/k_p$)
ω	Van Driest's damping coefficient

Subscripts

a	Asymptotic values
c	Conditions at the cold surface
D	Values calculated based on tube diameter
h	Conditions at the heated surface
H	Values calculated based on plate separation distance
i	Conditions at inlet

CHAPTER 1

INTRODUCTION

1.1 Importance of the Study :

The number of investigations on convective heat transfer through a fluid-saturated porous media has been on the rise during the past decade. The need for fundamental studies in porous media heat transfer stems from the fact that a better understanding of the physical phenomena is required for a host of thermal engineering applications in which porous materials are present. The accumulated impact of these studies is twofold : first to improve the performance of existing porous-media-related thermal systems, and second to generate new ideas and explore new avenues with respect to the use of porous media in heat transfer applications. Some examples of thermal engineering disciplines which stand to benefit from a better understanding of heat and fluid flow processes through porous materials are - geothermal systems, thermal insulations, grain storage and oil extraction. Many industrial operations in chemical and metallurgical engineering involve the passage of a fluid stream through a bed of solid particles to obtain extended solid fluid interfacial areas and good fluid mixing, thereby enhancing heat transfer. Typical examples of applications involving such systems include catalytic and chromatographic reactors [31,38,82,83], packed absorption and distillation towers, ion exchange columns, packed filters, pebble-type heat exchangers, etc. Packed bed systems have also found its way into the electronic industry [33-37]. For example, Chu and Hwang [37] proposed the use of a bed of

particles consisting of spherical plastic beads surrounding electronic components with a dielectric coolant flowing through the bed as a means of cooling components. This technique is called the direct liquid immersion cooling because it brings the coolant into direct physical contact with the chips or packages to be cooled. The beads would in this case act as turbulators for enhanced heat transfer.

The design of porous media systems that are used in chemical and metallurgical industries and in electronic cooling, is decided by the pressure drop, fluid flow and heat and mass transfer characteristics in the packed bed. Considerable attention has been paid to the aforementioned aspects because of their direct influence on the optimization and stability of the design of these systems. Thus, a need for a thorough analysis of all the aspects of flow, heat and mass transfer in packed bed exists in light of its usefulness in the design and operation of systems employing packed bed units.

1.2 Natural and Forced Convection in Porous Media :

In some of the applications mentioned above, e.g. geothermal reservoirs, the flow is unbounded and in the absence of an external pressure gradient, heat transfer takes place primarily due to natural convection [46,47]. Whereas when the flow is confined, e.g. in heat exchangers and in electronic cooling, where an external pressure gradient exists, forced convection predominates. Needless to say that in most of the above mentioned applications mixed mode of heat transfer exists. In geothermal reservoirs, for example, the effects of forced convection may become important near a well because of pressure gradients that are generated as a result of withdrawal or reinjection of geothermal fluids. Other examples of a porous media systems in which

mixed convection exists are in a saltless solar pond [49] and in building insulation structure [48].

1.3 Early Mathematical Models for Heat Transfer in Porous Media :

Early studies on the transport phenomena in porous media are based on Darcy's law as the momentum equation with the same energy equation as in the classical laminar heat transfer problem. The Darcy law is an empirical equation which states that the volumetric average velocity u in a packed column is proportional to the pressure drop along the packed column, i.e.,

$$u = -\frac{k}{\mu}\frac{dp_f}{dx} \tag{1.1}$$

where k is the permeability, μ is the viscosity of the fluid, p_f represents the pressure and x the direction of flow.

In 1901 Forchheimer [128] found experimentally that the Darcy law is invalid at high flow velocities. Forchheimer added a velocity square term in the Darcy law to account for the inertial effect which gives

$$\frac{\mu u}{k} + \frac{\rho f u^2}{\sqrt{k}} = -\frac{dp_f}{dx} \tag{1.2}$$

where f is the inertia coefficient and ρ is the density of the fluid.

To account for the shearing stress, Brinkman [12] added a shearing stress term in the Darcy law to give

$$\frac{\mu u}{k} + \frac{\rho f u^2}{\sqrt{k}} = -\frac{dp_f}{dx} + \frac{\mu}{\varphi}\frac{d^2u}{dy^2} \tag{1.3}$$

where φ is the porosity of the medium and y is the cross-stream coordinate direction. Applications of these early mathematical models to natural convection in geothermal reservoirs have been given by Cheng [41].

1.4 Recent Mathematical Models for Convective Heat Transfer in Porous Media :

As mentioned in the previous section, early mathematical models on heat transfer in porous media were based either on Darcy law, the Forchheimer model or the Brinkman model as the momentum equation. In addition, the permeability and porosity were assumed to be constant and the thermal dispersion effect was assumed to be negligible. Recently, a comparison of experimental data with theoretical results based on early models found that discrepancies between theory and experiments exist under certain conditions : when the dimensionless particle diameter (i.e. the ratio of the particle diameter to the characteristic length) is not vanishingly small, and when the velocity is high. The former has been attributed to the variable porosity effect while the latter to the thermal dispersion effect. These effects which have been neglected in early models will be discussed in this section.

1.4.1 Variable porosity effects :

A porous media is characterized by its porosity φ which is defined as the fraction of the void space in an elementary volume. For an unbounded medium randomly packed with uniform size spheres, the porosity varies from 0.36 to 0.4. If an impermeable surface is present, the porosity of the medium changes drastically from nearly one near the surface to $0.36 \sim 0.4$ in the core. The asymptotic value is reached by a damped oscillating function. For ideal metal spheres, Benenati and Brosilow [7]

and Roblee and Baird [115] measured the porosity as a function of distance from the wall of a packed tube. Their measurements show a high porosity region close to the external boundary. The damped oscillatory porosity data of Benenati and Brosilow [7] was correlated by Martin [3] and is expressed as the following :

$$\varphi = \begin{cases} \varphi_{min} + (1 - \varphi_{min})\, z^2 & y \le d_p / 2 \\ \varphi_a + (\varphi_{min} - \varphi_a) \exp[- z / 4] \cos(\pi z / l) & y > d_p / 2 \end{cases} \tag{1.4}$$

where $z = (2\, y / d_p - 1)$ with y representing the distance from the wall ; $\varphi_{min} = 0.23$ and $\varphi_a = 0.39$, $l = \sqrt{2}\,/\,3$ for $D/d_p \rightarrow \infty$, and $l = 0.876$ for $D/d_p = 20.3$, with D and d_p denoting the diameter of the tube and the solid particles respectively. It should be pointed out that the values of l in Eq. (1.4) are available only for $D/d_p = 20.3$ and $D/d_p \rightarrow \infty$. A functional relationship of l and D/d_p is not available in the literature at the present time.

In view of the fact that the governing equations for porous media flow, are volumetric average equations, the oscillation of porosity were neglected in most of the theoretical studies [9-11,13-16,19-22,43,45,96,97,99,106,108,113], and the variations of porosity were approximated by an exponential function of the form :

$$\varphi = \varphi_a [\, 1 + C_1 \exp(- N\, y / d_p)] \tag{1.5a}$$

where φ_a is the asymptotic value of porosity and y is the transverse distance from the wall. It should be noted that Eq. (1.5a) should be considered as a line averaged porosity of Eq. (1.4) in the direction normal to the wall. Since Eq. (1.4) is a correlation equation for the experimental data of Benenati and Brosilow [7] which gives the line

average porosity parallel to the wall, Eq. (1.5a) is a good estimate of the volumetric average porosity at any location in the packed bed.

In Eq. (1.5a) the porosity variation is considered only in the cross-stream direction. However, in the real situation porosity would also vary in the streamwise direction due to the presence of the surfaces (usually screens) which confine the porous medium or when the system is partially filled with porous media. In the present study (wherever applicable) therefore, the following form of the porosity variation was assumed :

$$\varphi = \varphi_a [\, 1 + C_1 \exp(-N\, y / d_p)][\, 1 + C_2 \exp\{-(L - x)/d_p\}] \qquad L/2 \le x \le L \qquad (1.5b)$$

$$\varphi = \varphi_a [\, 1 + C_1 \exp(-N\, y / d_p)][\, 1 + C_2 \exp(-x / d_p)] \qquad 0 \le x \le L/2 \qquad (1.5c)$$

A comparison of the fluid flow and heat transfer results with the assumption of porosity distribution given by Eqs. (1.4) and (1.5) will be presented in Chapter 5. In Eq. (1.5) the values of the empirical constants φ_a, N, and C_1 were determined in this study by a comparison of the numerical solutions of the pressure drop and heat flux with available experimental data while the value of C_2 was calculated (see Chapter 5).

Due to the large-scale variation in porosity (and hence permeability) close to an impermeable surface, a number of important effects such as flow maldistribution and channeling takes place. Channeling, which refers to the occurrence of a maximum velocity (or velocity overshoot) in a region close to an external boundary, has been reported by a number of investigators such as Schwartz and Smith [5], and Schertz and Bischoff [6]. Their velocity measurements in packed beds show a maximum close to the boundary which results from larger porosity value near the boundary. Chandrasekhara and Vortmeyer [20] used the measured porosity

variations of Benenati and Brosilow [7] and calculated numerically the velocity distribution in an isothermal packed bed. Chandrasekhara and Vortmeyer's results also show a peak velocity near the wall. Due to the variation of porosity in the packed bed, the effective thermal conductivity of the medium, which depends on the fluid and solid conductivities and upon the porosity [118], will also vary. As a result of the flow channeling, therefore, heat and mass transfer will also be affected. Thus, there is a need to include the variable porosity effects on flow, heat and mass transfer in the vicinity of an impermeable boundary.

1.4.2 Variable stagnant thermal conductivity effects :

The stagnant thermal conductivity of a porous media depends on the thermal conductivity of the fluid phase k_f, the thermal conductivity of the solid phase k_p, and the porosity of the medium φ. Thus, the stagnant thermal conductivity is nonuniform in a variable porosity medium.

The value of the stagnant thermal conductivity, k_s, can be evaluated by various methods [28,63,118,126,127]. By considering the influence of the particle shape and the variable porosity effect, Zehner and Schlunder [28] have obtained a semi-analytical expression for the stagnant thermal conductivity which is given by :

$$\frac{k_s}{k_f} = \left[1 - \sqrt{1-\varphi}\right] + \frac{2\sqrt{1-\varphi}}{(1-\lambda S)}\left[\frac{(1-\lambda)S}{(1-\lambda S)^2}\ln\left(\frac{1}{\lambda S}\right) - \frac{(S+1)}{2} - \frac{(S-1)}{(1-\lambda S)}\right] \qquad (1.6)$$

with $S = C_{form}\left[\frac{1-\varphi}{\varphi}\right]^{10/9}$ and $\lambda = k_f / k_p$ where S is called the deformation factor and

C_{form} (with a value of 1.25 for spherical particles) is the influence coefficient of deformation factor for the conduction fraction determined from experimental data.

1.4.3 Thermal dispersion effects :

The presence of solid particles in the fluid introduces an additional transport mechanism called dispersion which results from mixing of the fluid in the pores. At high flow rates, dispersion overwhelms diffusion, thus dominating the transport process. It should be emphasized that dispersion occurs even at low Reynolds numbers where the flow is laminar. Dispersion in packed beds is similar to turbulent eddy motion. However, their mechanisms are different in nature. Turbulent eddies arise from the instability of the flow, whereas dispersion in packed-beds is due to the existence of the solid matrix which forces the flow to go around it thus causing mixing of the fluid in the pores. The dispersion conductivity, therefore, represents the transport induced as the fluid is forced to follow a tortuous path around the solid particles. Thus, the dispersion conductivity depends upon the fluid velocity and the size of the particles around which the fluid travels. Experiments on forced convection in packed columns [1,56,61,65,79] have shown that the average radial or transverse thermal dispersion conductivity at high Reynolds numbers can be correlated as a linear function of Reynolds number as follows :

$$(k_d)_{av} / k_f = C_d^{'} \, Pe \qquad (1.7)$$

where $(k_d)_{av}$ is the cross-sectional average of the transverse thermal dispersion conductivity ; k_f the thermal conductivity of the fluid ; $C_d^{'} = 0.09 \sim 0.1$ [65,79] ; Pe the Peclet number defined as $Pe = Re_d \, Pr = u_i \, d_p/\alpha$ (with $Pr = \nu/\alpha$ being the Prandtl

number of the fluid and Re_d being the Reynolds number based on the particle diameter d_p and the mean velocity u_i, and α being the thermal diffusivity of the fluid). Based on the correlation given by Eq. (1.7), Cheng et al. [8-11,15,119,120] assumed that the local transverse thermal dispersion conductivity k_d is

$$k_d / k_f = C_d \, Pe \, \mathit{I} (u / u_i) \tag{1.8}$$

where the factor u / u_i was introduced to account for the local velocity variation. In Eq. (1.8), I is a dimensionless dispersive length (normalized with respect to the particle diameter d_p). The dispersive length was represented by a two-layer model in the earlier papers of Cheng et al. [8,9]. In a series of later papers Cheng et al. [10,11,15,119, 120] identify I as the Van Driest type of wall function [124] given by

$$\mathit{I} = 1 - \exp[- (r_o - r) / \omega \, d_p] \tag{1.9}$$

where ω is an empirical constant. Cheng et al. [8,15,29] found that without the wall function in Eq. (1.8) the observed steep transverse temperature gradients from experiments cannot be reproduced in theory. This implies that the channeling effect alone is not responsible for the observed temperature gradient behavior. The empirical constants C_d (also called the dispersion coefficient) in Eq. (1.8) and ω in Eq. (1.9) were obtained by comparing the heat transfer characteristics with the available experimental data.

Hsu and Cheng's dispersion model :

Carbonell & Whitaker [110] and Hsu & Cheng [45,98] show that dispersion enters the volume-averaged energy equations by decomposing the

convective term into the bulk convective flux and the interpore transport due to local spatial variations in velocity and temperature. This additional transport resembles a diffusive flux and thus is equated to the global temperature gradient and a dispersion conductivity, k_d [110]. Hsu & Cheng [45,98] obtained a closure scheme for the dispersion conductivity term and showed that it depends on the flow velocity and particle size of the porous medium. This agrees with the empirical models from various heat and mass transfer studies outlined in Wakao et al. [39] and Wen et al. [114]. Hsu & Cheng [45,98] obtained an expression for the dispersion conductivity tensor by giving special consideration to creeping flow at low Reynolds numbers and boundary layer flow and wakes at high Reynolds numbers. Accordingly at high Reynolds numbers $Re_{dl} >> 10$

$$\frac{k_d}{k_f} = C_d \left(\frac{1 - \varphi}{\varphi} \right) Pe_l \tag{1.10a}$$

and for low Reynolds numbers ($Re_{dl} << 10$)

$$\frac{k_d}{k_f} = C_d \left(\frac{1 - \varphi}{\varphi^2} \right) Pe_l^2 \tag{1.10b}$$

where the Peclet number $Pe_l = Re_{dl}\, Pr$ with Pr and $Re_{dl} = u\, d_p / \nu$ denoting the Prandtl number and the local Reynolds number respectively.

Present dispersion model :

It has been reported by Kunii et al. [69] that the value of the coefficient C_d in Eq. (1.8) depends on the ratio of the particle size to the characteristic length (also refered to as the dimensionless particle diameter) of the packed bed. Preliminary

numerical simulations, conducted in this research, using Eq. (1.10) as the dispersion conductivity model verified this dependance of C_d on the dimensionless particle diameter. In order to obtain a unique value of C_d (which is assumed to be a constant), the inclusion of a Van Driest type of damping function [124] into Hsu & Cheng's dispersion conductivity model is proposed in this study. This amounts to modifying Eq. (1.10) and writing it as the following :

$$\frac{k_d}{k_f} = C_d \left(\frac{1-\varphi}{\varphi}\right)\left[1 - \exp\{-(r_o - r)/\omega d_p\}\right] Pe_l \qquad Re_{dl} >> 10 \qquad (1.11a)$$

$$\frac{k_d}{k_f} = C_d \left(\frac{1-\varphi}{\varphi^2}\right)\left[1 - \exp\{-(r_o - r)/\omega\, d_p\}\right] Pe_l^2 \qquad Re_{dl} << 10 \qquad (1.11b)$$

with the values of C_d and ω to be determined by comparing the numerical solution of the heat flux with the available experimental data. The Van Driest type of wall function not only damps the value of the dispersion conductivity at the wall but also takes into account the diameters of the packed bed and the particle. The Van Driest wall function [124] has been very successfully used in classical turbulent convective heat transfer problems and is therefore reasonable to expect to be valid in porous media heat transfer problems especially in the wall region where porosity is nearly unity. It should be mentioned that because of the dependance of the dispersion thermal conductivity (e.g. Eq. (1.10 or 1.11)) on porosity the values of C_d and ω depend on the porosity function chosen.

Two other dispersion models that are available in the open literature have also been considered in this study to evaluate their accuracy in predicting the heat flux for forced convection in a packed bed. These dispersion models will be discussed next.

Kuo and Tien's dispersion model :

Kuo & Tien [121] proposed a theoretical model for the transverse dispersion in packed-sphere beds that includes the core and the near wall region. In the core region, the transverse dispersion process was depicted through the use of the mixing-length concept and statistical averaging. Their results indicate that the dispersion coefficient is independent of the porosity variation in this region. Near the bounding wall, the perturbation concept was utilized to establish a theoretical expression for the dispersion coefficient distribution. To a leading-order approximation the dispersion coefficient was found to be proportional to the square of the dimensionless distance from the wall (nondimensionalized with the sphere diameter). To match the wall and the core regions, a damping function, like that of Van Driest [124], was introduced to account for the reduction in the dispersion coefficient near the wall. The transverse dispersion conductivity model of Kuo and Tien [121] can be written as follows :

$$\frac{k_d}{k_f} = 0.075 \left[1 - \exp\left\{ - 5 \left(y / d_p\right)^2 \right\}\right] Pe_l \qquad (1.12)$$

where the value 0.075 in Eq. (1.12) is the dispersion coefficient.

Koch and Brady's dispersion model :

Another dispersion model which has been considered in this study was proposed by Koch & Brady [122]. Koch and Brady obtained an ensemble averaged energy equation by using the concept of the representative elementary volume. For periodic structures, they were able to obtain closed form solution for the dispersion coefficient. The following assumptions or simplifications were made in their analysis :

a) dilute concentration of particles - referring to large porosity and thereby permeability,
b) single-particle velocity disturbance found as the solution of the Brinkman momentum equation - i.e. inertial drag force term was neglected, and
c) slowly varying temperature field - equivalent to the thermal equilibrium assumption.

The transverse component of the dispersion conductivity, with the effect of particle interaction taken into account, for high Peclet number flows (Pe >> 1) is given in [122] as the following :

$$\frac{k_d}{k_f} = 0.14\ \varphi\ \sqrt{(1-\varphi)}\ Pe_l \qquad (1.13)$$

where the value 0.14 in Eq. (1.13) was obtained analytically. Since Koch and Brady's dispersion model was derived based on the assumption of constant porosity, it can only be applied when the ratio of the particle diameter to the characteristic length of the problem is small.

1.5 Studies on Forced Convection :

1.5.1 Experimental studies :

More than thirty experiments have been performed on forced convection through cylindrical [1,6,17,32,52-78] annular [79-81] and rectangular [2,21,51,116] packed columns. The purposes of the experiments were primarily to obtain correlation equations of the effective radial thermal conductivity and the wall heat transfer rate for the design of wall-cooled catalytic reactors. A rational design of this type of reactor is essential in order to avoid disastrous runaway temperature, low conversion rate and catalyst damages.

1.5.2 Studies on hydrodynamically and thermally fully developed flows :

Cheng and Vortmeyer [8], Cheng and Zhu [11] and Cheng and Hsu [9] investigated analytically the fully-developed forced convection problem in a packed channel, packed circular tube and an annular packed bed respectively. A Van Driest type of wall function was introduced to account for the thermal dispersion effects near the walls in the cross stream direction. The method of matched asymptotic expansion was employed to obtain an analytical solution for the velocity distribution in the packed bed. The fully developed temperature profile was obtained numerically by integrating the energy equation. Comparisons were made with the experimental results of the temperature distribution and heat flux of Schroeder et al. [2] for the packed channel (asymmetric heating), with Verschoor et al. [17] (constant wall temperature) and Quinton et al. [61] (constant heat flux) for the circular tube configuration, and with Yagi et al. [105] for the annular packed tube case.

1.5.3 Studies on hydrodynamically fully developed and thermally developing flows :

For the case of thermally developing flow in packed beds, Vafai and Tien [13] and Vafai [14,99] investigated numerically the forced convective problem in the vicinity of a heated flat plate embedded in a porous medium. Vafai [99] derived an approximate solution for the thermally developing flow problem by integrating the energy equation with the approximation of a second-order polynomial for the temperature distribution. The resulting equation was solved numerically to obtain the temperature profile. Cheng et al. [15] investigated numerically the forced convective flow problem in the entrance region of a packed channel. Chowdhury et al. [16] and

Poulikakos et al. [50] reported their numerical results for forced convection in a packed channel and a packed tube. But there exists a basic difference between these works. Poulikakos et al. [50] did not consider the thermal dispersion effect whereas Cheng et al. [15] and Chowdhury et al. [16] included it in their work. Cheng et al. [15] and Chowdhury et al. [16] obtained numerical solutions for the hydrodynamically fully developed and thermally developing forced convective flow problem by solving the set of finite difference equations with the Tri-Diagonal Matrix Algorithm (TDMA). Poulikakos et al. [50] used the Keller Box method [100,101] for the discretization of the energy equation and the block elimination method to obtain the solution. Hunt and Tien [22] numerically analyzed the thermally developing flow problem in a packed tube with the thermal dispersion conductivity taken into consideration in an approximate manner. Hunt and Tien [22] found their numerical solution of the temperature profile to be in good agreement with Plautz and Johnstone's [1] experimental data. The effects of thermal dispersion on forced convection in high-porosity fibrous media was investigated both numerically and experimentally by Hunt and Tien [108]. Their results show that the porous medium enhances heat transfer from the surface as compared to those for slug or laminar flow in an empty tube.

1.5.4 Studies on hydrodynamically and thermally developing flows :

Only a few papers discuss hydrodynamically and thermally developing flow problems in packed beds. Kaviany [90] reported numerical results for laminar flow through a porous channel bounded by isothermal parallel plates ; the inertia term, and variation in matrix porosity were not accounted for in this study. Low Reynolds number heat transfer in a packed bed was studied numerically by Khader and Goodling

[107]. Kaviany [102] obtained numerical solution for the hydrodynamically and thermally developing forced convection problem in the vicinity of a semi-infinite flat plate embedded in a porous media, through the application of (a) the Keller Box finite difference method [100,101] which was solved by the Newton's iteration method, (b) a third order expansion method and solved by the fourth-order Runge-Kutta-Gill method, and (c) the integral method which was solved numerically.

1.6 Studies on Mixed Convection :

1.6.1 Experimental work :

Reda [93] conducted an experimental and numerical investigation of mixed convection about a cylindrical heat source in a vertical annular region filled with a fluid-saturated porous medium. To the authors' knowledge no other experimental study has been reported on mixed convection in a packed sphere bed in a vertical column at constant wall temperature boundary conditions.

1.6.2 Numerical work :

In the case of mixed convection in porous media, early numerical results were reported by Cheng [84,85] and Cheng et al. [4], Ranganathan and Viskanta [86], and Minkowycz et al. [87] for problems involving external flow. Islam and Nandakumar [88] solved the problem of buoyancy-induced secondary flow in a horizontal porous rectangular channel. Numerical studies of mixed convection in horizontal porous layers have been presented by Haajizadeh and Tien [89], Prasad et al. [91] and Lai et al. [104]. Lai et al. [94] reported numerical results for mixed convection in a vertical porous layer for the case when a finite isothermal heat

source is located on one vertical wall while the other wall is isothermally cooled. However, their study is restricted to Darcy flow. Recently Hadim et al. [95] conducted a numerical investigation for mixed convection in a packed channel. In solving the mixed convection problem, Lai et al. [104] and Hadim et al. [95] used the control volume based scheme [27] to discretize the governing equations. The resulting discretized algebraic equations were solved using the Gauss-Seidel point iterative method. To the authors' knowledge, no other studies exist for the problem of mixed convection in a vertical packed column. In none of the studies discussed in this section were the effects of thermal dispersion taken into account.

1.7 Scope of the Present Study :

In this study, a detailed numerical investigation for forced and mixed convection in a vertical channel and a tube, filled with a fluid-saturated porous medium, was performed with particular emphasis on the developing region. For the packed tube configuration a uniform wall temperature, t_h, is maintained at the wall which is higher than the uniform inlet temperature, t_i, of the fluid such that, for the mixed convection case, buoyancy effects are assisting the upward flow. For the packed channel case temperatures of the two opposite walls are maintained at t_h and t_c ($t_h > t_c$). The fluid at the inlet of the channel is isothermal at temperature t_i. The present investigation uses the full momentum equations derived by Hsu & Cheng [45,98], which accounts for variable porosity and permeability as well as viscous and inertia effects. A model that accounts for the variation of porosity in the streamwise and cross-stream direction has been introduced. In the energy equation the thermal dispersion effect has been taken into account by using the closure scheme model given by Hsu & Cheng [45,98] and a

Van Driest type of damping function [124] as in classical turbulent heat transfer problems. The Van Driest function damps the dispersion near the wall and also takes into account the effect of the ratio of the particle diameter to the characteristic length of the problem on dispersion.

CHAPTER 2

MATHEMATICAL FORMULATION

In the present study, forced and mixed convection in a vertical channel and a tube filled with a fluid-saturated porous medium were investigated numerically. The systems under investigation are shown schematically in Fig. 1. Figure 1a depicts a vertical channel filled with a fluid saturated porous medium and bounded by two solid walls, which are maintained at different temperatures t_h and t_c ($t_h > t_c$). The fluid at the inlet of the channel is isothermal at temperature t_i. Figure 1b shows the conditions for a packed tube heated at a constant wall temperature. In this case the tube inlet temperature, t_i, is less than the wall temperature, t_h. In both cases, an external pressure gradient is imposed and the inlet velocity is u_i. At the entrance region where the relatively cold fluid enters, it is expected that the fluid buoyancy force would play an important role in the heat transfer process. The buoyancy force becomes important because the fluid next to the hot wall rises due to decrease in density and then flows downstream. An intent of this study was to investigate both mixed and forced convective flow and heat transfer characteristics in a vertical packed column.

2.1 Governing Equations :

The analysis of flow and heat transfer is usually based on the transport equations resulting from the differential balance laws. To predict global effects such as flow resistance or heat flux from a given object, requires detailed information of the

surrounding velocity and temperature fields. This information is extracted from the solution of the associated transport equations, subject to the pertinent boundary conditions. When flow through a complex structure such as a porous medium is involved, these equations are still valid inside the pores, but the geometric complexity prevents general solutions of the detailed velocity and temperature fields. Instead, some form of the 'macroscopic' balance equations based on the average over a small volumetric element must be employed. A common practice is to replace the 'microscopic' momentum and energy equations by the corresponding 'macroscopic' equations with the help of some closure schemes.

Flow parameters in porous media, such as velocity and temperature, are often determined by averaging the local quantities over some representative volume [109,110]. For higher flow rates, the velocity profile is often quite irregular and local velocity measurements fluctuate from the average value, as indicated by the velocity measurements by Lerou & Froment [111], Vortmeyer & Schuster [19]. To account for these variations, the velocity is averaged over a small local volume. Slattery [109] and Carbonell & Whitaker [110] showed that this local averaging incorporates both global flow variations and local interpore transport. To insure that the average quantity is meaningful, the overall geometry, such as the tube diameter (or channel height), must be significantly large than the length corresponding to the particle or pore size. Furthermore the averaging volume must be small enough to minimize any gradients within the volume. Such a volume is often refered to as a Representative Elementary Volume (REV) [103].

In the present study it has been assumed that the flow in the packed bed is steady, incompressible and two-dimensional. The porous medium is considered to be

saturated with a single phase fluid which is in thermal equilibrium with the solid matrix. The thermophysical properties of the solid matrix and the fluid are assumed to be constant except in the body force term (i.e. in the mixed convection problem) of the momentum equations. The macroscopic continuity and momentum equations for a variable porosity medium, from the work of Hsu & Cheng [45,98] are :

$$\nabla \cdot \bar{u} = 0 \tag{2.1}$$

$$\rho \left(\bar{u} \cdot \nabla\right) \frac{\bar{u}}{\varphi} = - \nabla p + \rho \beta (t - t_i) \varphi \bar{g} + \mu \nabla^2 \bar{u} - \left[\frac{\mu \varphi \bar{u}}{k} + \frac{\rho f \varphi \bar{u} |\bar{u}|}{\sqrt{k}}\right] \tag{2.2}$$

where $\bar{u}$ is the Darcy velocity vector which can be expressed in terms of the volume average (macroscopic) velocity vector $\langle \bar{u} \rangle$ as follows

$$\bar{u} = \varphi \langle \bar{u} \rangle$$

In the momentum equation $\varphi = \vartheta_f / \vartheta$ is the porosity, with ϑ_f denoting the volume occupied by the fluid phase in the representative elementary volume ϑ; ρ, μ and β are the density, viscosity and thermal expansion coefficient of the fluid, $p = \varphi (p_f - p_i)$, where p_f is the volume averaged fluid pressure; g is the gravitational acceleration; t is the temperature field and t_i and p_i are the reference inlet temperature and pressure respectively ; and k and f are the permeability and inertia coefficients, which are dependent on the porosity and particle diameter.

Equation (2.2) contains terms similar to those found in the Navier-Stokes equation, along with the flow resistance terms inherent to porous media studies. The first two terms on the right hand side represent respectively the pressure gradient and the body force, while the third term is due to the viscous force caused by shear

forces along the solid boundaries and is significant in the near wall region where velocity gradient is steep [13]. The fourth term on the right hand side represents the viscous drag caused by the solid particles [109,110] whereas the last term accounts for high-flow-rate inertial pressure losses [23]. The last two terms on the right hand side are referred to as the total drag force per unit volume by Hsu & Cheng. [45,98]. The terms on the left hand side are the convective terms and are usually neglected except in the entrance region of the flow. The permeability, k, and the inertia coefficient, f, are given by the relations developed by Ergun [23] for flow in a packed-sphere bed as follows :

$$k = \frac{d_p^2 \varphi^3}{A(1 - \varphi)^2} \qquad \text{and} \qquad f = \frac{B}{\sqrt{A}\, \varphi^{3/2}} \tag{2.3 a,b}$$

with A and B being the Ergun constants. In the present study these constants were determined by a comparison of the numerical solution with the experimental results for pressure drop.

The steady macroscopic energy equation for flow through porous media in local thermal equilibrium, from the work of Carbonell & Whitaker [110], Hsu & Cheng [45,98] is :

$$\rho\, C_p\, \bar{u} \cdot \nabla t = \nabla \cdot (k_e \nabla t) \tag{2.4}$$

where C_p is the fluid heat capacity and $k_e = k_s + k_d$ is the effective thermal conductivity with k_s being the stagnant thermal conductivity given by Eq. (1.6) and k_d being the thermal dispersion conductivity given by Eq. (1.11).

2.1.1 Hydrodynamically and thermally developing mixed convection :

For steady, mixed convection in a packed bed, the continuity (Eq. (2.1)), momentum (Eq. (2.2)) and energy (Eq. (2.4)) equations for the two-dimensional flow in the axisymetric coordinate system can be written as the following :

Continuity equation

$$\frac{\partial}{\partial x}(r\,u)+\frac{\partial}{\partial r}(r\,v)=0 \tag{2.5}$$

Momentum equation : x - component

$$\rho\left[u\frac{\partial}{\partial x}\left(\frac{u}{\varphi}\right)+v\frac{\partial}{\partial r}\left(\frac{u}{\varphi}\right)\right]=-\frac{\partial\,\varphi\,(p_f-p_i)}{\partial x}-\rho\,g\,\beta\,(t-t_i)\,\varphi+\frac{\mu}{r}\left[\frac{\partial}{\partial x}\left(r\frac{\partial u}{\partial x}\right)+\frac{\partial}{\partial r}\left(r\frac{\partial u}{\partial r}\right)\right]$$

$$-\left[\frac{\mu\,\varphi}{k}+\frac{\rho\,f\,\varphi}{\sqrt{k}}\sqrt{u^2+v^2}\right]u \tag{2.6}$$

Momentum equation : r - component

$$\rho\left[u\frac{\partial}{\partial x}\left(\frac{v}{\varphi}\right)+v\frac{\partial}{\partial r}\left(\frac{v}{\varphi}\right)\right]=-\frac{\partial\,(\varphi\,p_f)}{\partial r}+\frac{\mu}{r}\left[\frac{\partial}{\partial x}\left(r\frac{\partial v}{\partial x}\right)+\frac{\partial}{\partial r}\left(r\frac{\partial v}{\partial r}\right)\right]$$

$$-\left[\frac{\mu\,\varphi}{k}+\frac{\rho\,f\,\varphi}{\sqrt{k}}\sqrt{u^2+v^2}\right]v-\frac{\mu\,v}{r^2} \tag{2.7}$$

Energy equation :

$$\rho\,C_p\left[u\frac{\partial t}{\partial x}+v\frac{\partial t}{\partial r}\right]=\frac{1}{r}\left[\frac{\partial}{\partial x}\left(k_{ea}\,r\frac{\partial t}{\partial x}\right)+\frac{\partial}{\partial r}\left(k_{et}\,r\frac{\partial t}{\partial r}\right)\right] \tag{2.8}$$

In these equations, x and r are the axial and radial Cylindrical coordinates; u and v are the axial and radial velocities respectively ; k_{ea} and k_{et} are the effective thermal

conductivities in the streamwise and cross-stream directions respectively ; t is the temperature field and the subscript i denotes conditions at the inlet. The axial and transverse effective thermal conductivities were assumed to be equal in the numerical solutions. Typical boundary conditions for the mixed convection problem are as follows :

Dimensional boundary condition :

$$u = u_i \quad v = 0 \quad t = t_i \quad \text{at} \quad x = 0 \quad 0 < r < r_0 \tag{2.9}$$

$$u = 0 \quad v = 0 \quad t = t_h \quad \text{at} \quad x \geq 0 \quad r = r_0$$

$$\frac{\partial u}{\partial r} = 0 \quad v = 0 \quad \frac{\partial t}{\partial r} = 0 \quad \text{at} \quad x \geq 0 \quad r = 0$$

$$\frac{\partial u}{\partial x} = 0 \quad v = 0 \quad \frac{\partial \theta}{\partial x} = 0 \quad \text{at} \quad x \rightarrow \infty \quad 0 < r < r_0$$

where $\theta = (t_h - t)/(t_h - t_b)$ with t_b, the bulk temperature defined as

$$t_b = \frac{\int_0^{r_0} u\, t\, r\, dr}{\int_0^{r_0} u\, r\, dr}$$

Dimensionless variables can be formed according to the following :

$$U = \frac{u}{u_i} \qquad V = \frac{v}{u_i} \qquad X = \frac{x}{r_0} \qquad R = \frac{r}{r_0} \qquad \Phi = \frac{\varphi}{\varphi_a} \qquad \gamma = \frac{d_p}{D} \qquad K_e = \frac{k_e}{k_f}$$

$$k_a = \frac{d_p^2\, \varphi_a^3}{A(1 - \varphi_a)^2} \qquad f_a = \frac{B}{\sqrt{A}\, \varphi_a^{3/2}} \qquad K = \frac{k}{k_a} = \frac{\Phi^3}{\left[1 + \frac{\varphi_a}{(1 - \varphi_a)}(1 - \Phi)\right]^2}$$

$$F = \frac{f}{f_a} = \Phi^{-3/2} \qquad \sigma = \sqrt{\frac{k_a}{\varphi_a d_p^2}} \qquad T = \frac{t - t_i}{t_h - t_i} \qquad P = \frac{\varphi (p_f - p_i)}{\rho u_i^2}$$

$$Re_i = \frac{\rho u_i r_o}{\mu} \qquad Pr = \frac{\mu C_p}{k_f} \qquad Gr = \frac{g \beta (t_h - t_i) r_o^3}{\nu^2}$$

where φ_a is the asymptotic value of porosity and u_i represents the velocity at the inlet section. The corresponding dimensionless governing equations for the mixed convection problem can then be written as the following :

Continuity equation :

$$\frac{\partial}{\partial X}(R\,U) + \frac{\partial}{\partial R}(R\,V) = 0 \tag{2.10}$$

Momentum equation : x - component

$$U \frac{\partial}{\partial X}\left(\frac{U}{\Phi}\right) + V \frac{\partial}{\partial R}\left(\frac{U}{\Phi}\right) = - \varphi_a \frac{\partial P}{\partial X} + \frac{Gr\,T}{Re_i^2} \Phi \varphi_a^2 + \frac{\varphi_a}{Re_i R}\left[\frac{\partial}{\partial X}\left(R \frac{\partial U}{\partial X}\right) + \frac{\partial}{\partial R}\left(R \frac{\partial U}{\partial R}\right)\right]$$

$$- \frac{\varphi}{4 K \sigma^2 \gamma^2}\left[\frac{\varphi_a}{Re_i} + \frac{2 F B \sqrt{K}\ \sigma \gamma}{\sqrt{A}} \sqrt{U^2 + V^2}\right] U \tag{2.11}$$

Momentum equation : r - component

$$U \frac{\partial}{\partial X}\left(\frac{V}{\Phi}\right) + V \frac{\partial}{\partial R}\left(\frac{V}{\Phi}\right) = - \varphi_a \frac{\partial P}{\partial R} + \frac{\varphi_a}{Re_i R}\left[\frac{\partial}{\partial X}\left(R \frac{\partial V}{\partial X}\right) + \frac{\partial}{\partial R}\left(R \frac{\partial V}{\partial R}\right)\right]$$

$$- \frac{\varphi}{4 K \sigma^2 \gamma^2}\left[\frac{\varphi_a}{Re_i} + \frac{2 F B \sqrt{K}\ \sigma \gamma}{\sqrt{A}} \sqrt{U^2 + V^2}\right] V - \frac{\varphi_a}{Re_i} \frac{V}{R^2} \tag{2.12}$$

Energy equation :

$$U \frac{\partial T}{\partial X} + V \frac{\partial T}{\partial R} = \frac{1}{Re_i Pr R}\left[\frac{\partial}{\partial X}\left(K_{ea} R \frac{\partial T}{\partial X}\right) + \frac{\partial}{\partial R}\left(K_{et} R \frac{\partial T}{\partial R}\right)\right] \tag{2.13}$$

In dimensionless form the boundary conditions, Eq. (2.9) can be written as

$$U = 1 \quad V = 0 \quad T = 0 \quad \text{at} \quad X = 0 \quad 0 < R < 1 \tag{2.14}$$

$$U = 0 \quad V = 0 \quad T = 1 \quad \text{at} \quad X \geq 0 \quad R = 1$$

$$\frac{\partial U}{\partial R} = 0 \quad V = 0 \quad \frac{\partial T}{\partial R} = 0 \quad \text{at} \quad X \geq 0 \quad R = 0$$

$$\frac{\partial U}{\partial X} = 0 \quad V = 0 \quad \frac{\partial \theta}{\partial X} = 0 \quad \text{at} \quad X \to \infty \quad 0 < R < 1$$

Momentum equations (2.11) and (2.12) and the energy equation (2.13) with the boundary conditions Eq. (2.14) constitute the mixed convection problem in a cylindrical packed tube. The relevant parameters for the mixed convection problem are Gr, Pr, Re_i, γ, and k_f / k_s. The governing equations and boundary conditions for the hydrodynamically and thermally developing forced convection problem are the same as in Eqs. (2.10-2.14) except that the body force term in Eq. (2.11) is neglected.

The governing equations were discretized using the control-volume scheme and solved by the application of the SIMPLER algorithm [27] (Chapter 3) on a non-uniform computational grid plane. Grids were clustered near the walls and also at the inflow and outflow boundaries where changes in the dependent variables are expected to be large. A complete description of the grid generation formulae are presented in Chapter 3.

For the cylindrical packed tube at constant wall temperature the average Nusselt number can be defined as

$$Nu_{DL} = \frac{1}{L} \int_0^L Nu_{Dx} \, dx \tag{2.15a}$$

$$\text{where } Nu_{Dx} = \frac{q_{wx}\, D}{k_f (t - t_b)} \tag{2.15b}$$

with $q_{wx} = -\left(k_e\, \partial T / \partial r\right)_{x,\, r = r_0}$ which is the local heat flux at the wall and t_b is the bulk-mean temperature defined in Eq. (2.9).

For the Cartesian coordinate system the governing equations can be developed in the same way and is not shown here for brevity. For a packed channel heated asymmetrically at temperatures t_h and t_c, the average Nusselt number can be defined as the following :

$$Nu_{HL} = \frac{1}{L}\int_0^L Nu_{Hx}\, dx \tag{2.16a}$$

$$\text{where } Nu_{Hx} = \frac{q_{wx}\, H}{k_f (t_h - t_c)} \tag{2.16b}$$

with $q_{wx} = -\left(k_e\, \partial T / \partial y\right)_{x,\, y = 0}$ being the local heat flux at the wall.

2.1.2 Hydrodynamically fully developed and thermally developing forced convection :

It has been shown theoretically that the velocity boundary layer growth in porous media takes place over a short distance from the entrance [13]. Therefore, in this section a hydrodynamically fully developed flow was assumed at the entrance of the packed bed. With this approximation the governing equations and boundary conditions in the axisymetric coordinate system in dimensionless form yields :

The momentum equation in the r direction

$$U\left[\frac{1}{K} + \frac{C_a\, F\, U}{\sqrt{K}}\right] = -\frac{dP}{dx} + \frac{C_b}{\Phi}\frac{1}{R}\frac{d}{dR}\left[R\,\frac{dU}{dR}\right] \tag{2.17}$$

which is to be solved subject to boundary conditions :

$$U = 0 \text{ at } R = 1/2\gamma \tag{2.18}$$

$$\frac{\partial U}{\partial R} = 0 \text{ at } R = 0$$

The energy equation with the boundary layer approximation is

$$U \frac{\partial T}{\partial X} = \frac{1}{R} \frac{\partial}{\partial R}\left[R K_{et} \frac{\partial T}{\partial R}\right] \tag{2.19}$$

which is to be solved subject to boundary conditions :

$$T = 0 \text{ at } X = 0 \text{ and } 0 < R < R_0 \tag{2.20}$$

$$T = 1 \text{ at } X \geq 0 \text{ and } R = R_0$$

$$\frac{dT_c}{dX} = 0 \text{ where } T_c = \frac{t - t_i}{t_h - t_b} \text{ as } X \rightarrow \infty$$

where t_b is the bulk temperature defined as

$$t_b = \frac{\int_0^{r_0} u\, t\, r\, dr}{\int_0^{r_0} u\, r\, dr} = \frac{2}{R_0^2\, U_m} \int_0^{R_0} U\, t\, R\, dR$$

$$\text{with } U_m = \frac{u_m\, d_p}{\nu} \text{ and } u_m = \frac{2}{r_0^2} \int_0^{r_0} u\, r\, dr$$

The dimensionless variables for the governing equations can be defined as follows :

$$U = \frac{u\, d_p}{\nu} \quad R = \frac{r}{d_p} \quad \gamma = \frac{d_p}{D} \quad R_0 = \frac{r_0}{d_p} = \frac{1}{2\gamma} \quad \Phi = \frac{\varphi}{\varphi_a} \quad k_a = \frac{d_p^2\, \varphi_a^3}{A(1 - \varphi_a)^2}$$

$$f_a = \frac{B}{\sqrt{A}\, \varphi_a^{3/2}} \quad K = \frac{k}{k_a} \quad F = \frac{f}{f_a} \quad P = \frac{k_a\, d_p}{\rho\, \nu^2}\, p_f \quad C_a = \frac{B}{A(1 - \varphi_a)}$$

$$C_b = \frac{\varphi_a^2}{A(1 - \varphi_a)^2} \quad X = \frac{x}{Pr\, d_p} \quad T = \frac{t - t_i}{t_h - t_i} \quad K_{et} = \frac{k_{et}}{k_f}$$

In equation (2.17) the porosity function was assumed as the following :

$$\Phi = [1 + C_1 \exp\{- N (R_0 - R)\}] \tag{2.21}$$

Equations (2.17) and (2.19) with the boundary conditions Eqs. (2.18) and (2.20) constitute the governing equations for the hydrodynamically fully developed and thermally developing forced convection problem. It is evident that these equations are not coupled unlike the mixed convection problem and can therefore be solved independent of each other. Since the velocity field is required to solve the energy equation, it is logical to solve the momentum equation first. This was achieved by first discretizing the momentum equation with the use of a control-volume type of differencing scheme. A coordinate transformation (see Chapter 3) was employed in the cross-stream direction to clustered grids near the wall where velocity gradients are expected to be steep. The resulting equations in the transformed coordinates were solved on the uniformly spaced computational grid plane by the application of the TDMA. Since the momentum equation has a non-linear term, it was first linearized by expressing the product of the velocities as one between a known quantity from the

previous iteration, and the unknown variable. The iterative process was terminated when the difference in velocities of subsequent iterations did not change by a preset small value (10^{-4}).

The energy equation (2.19) was discretized using the control-volume type of differencing scheme for the transverse derivatives and the upwind difference for the srteamwise derivative (i.e. for the convective term). Grid transformations were used in the streamwise and the cross-stream directions to investigate the temperature gradients at the wall and the inlet/outlet sections respectively. The marching procedure was used for the solution of the energy equation for the developing flow problem. The discretized equations at each axial station were solved by the TDMA. The downstream temperature profile was checked to ensure thermally fully developed condition as in Eq. (2.20). The average Nusselt number was calculated according to Eq. (2.15).

CHAPTER 3

THE NUMERICAL METHOD & GRID GENERATION

Most of the numerical studies on mixed or forced convection in packed beds [95,102] are based on the "stream-function/vorticity method", i.e. using stream function and vorticity as dependent variables in the computations. The stream-function/vorticity method has some attractive features. The pressure makes no appearance, and, instead of dealing with the continuity equation and two momentum equations, only two equations need to be solved to obtain the stream function and the vorticity. Some of the boundary conditions can be easily satisfied, e.g. when an external irrotational flow lies adjacent to the calculation domain, the boundary vorticity can conveniently be set to zero. There are, however, some major disadvantages to the stream-function/vorticity method. The value of the vorticity at the wall is difficult to specify and is often the cause of trouble in getting a converged solution. The pressure, which has been so cleverly eliminated, frequently happens to be an important desired result or even an intermediate outcome required for the calculation of density and other fluid properties. Then, the effort of extracting pressure from vorticity offsets the computational savings obtained otherwise. But, above all, the major shortcoming of the method is that it cannot easily be extended to three-dimensional situations, for which a stream function does not exist. Since most practical problems are three-dimensional, a method that is intrinsically restricted to two dimensions suffers from a serious limitation. For three dimensional problems, an approach based on vorticity uses six

dependent variables, namely, the three components of the vorticity vector and the three components of the velocity-potential vector [125]. Thus, the complexity is actually greater than that of treating the three velocity components and pressure directly. Also, the vorticity vector and the velocity-potential vector involve concepts that are harder to visualize and interpret than the meanings of the velocity components and pressure. On the other hand a physically meaningful approach can be adopted by using the so-called primitive variables i.e. the velocity components and pressure. In this study therefore, the primitive variable approach has been adopted with the hope that in the future it can be extended to three-dimensional problems.

Patankar [27] developed an algorithm which is abbreviated SIMPLER (Semi-Implicit Method for Pressure Linked Equations Revised) to solve the conservation equations of momentum, energy, chemical species, etc. using the primitive variables. In this study, a numerical code was written based on the SIMPLER algorithm to solve the simultaneously developing mixed and forced convection problems. The next section will include a brief description of the SIMPLER method.

3.1 Description of the Numerical Algorithm :

In the numerical algorithm, primitive or physical variables U, V, P, and T are used in a staggered grid system. The computational domain is divided into rectangular control volumes with one grid point located at the center of the control volume which forms the basic cell over which the governing equations are applied and discretized. Figure 2 shows a portion of a two-dimensional grid. In the staggered grid, the dependent variables are not all calculated at the same grid points. The velocity components, U and V, are given displaced or staggered locations. In Fig. 2, the

locations of the two velocity components are indicated by short arrows in the direction of the velocity component. All other variables, e.g. temperature, and pressure, are calculated at the grid points shown by the dots. A consequence of this arrangement is that the normal velocity components are directly available at the control-volume faces, where they are needed for the calculation of the mass flow rates. In addition, the pressure difference between two adjacent grid points can be used to "drive" the velocity component located between them.

3.2 Discretized Continuity Equation :

The discretized continuity equation can be obtained by integrating Eq. (2.10) over the control volume in Fig. 2 to give

$$(\rho U A)_w - (\rho U A)_e + (\rho V A)_s - (\rho V A)_n = 0 \qquad (3.1)$$

where U and V denote the velocity components in the streamwise and cross-stream directions respectively, and A is the product of the width of the control volume normal to the flow and the radial distance. The mass flux through the control volume faces (denoted by the subscripts) is represented by the quantity inside the parentheses in Eq. (3.1).

3.3 Discretized Momentum Equations :

The staggered locations for the velocity components determine the corresponding control volumes to be used for conservation of momentum. The faces of these control volumes that are normal to the direction of the velocity component pass

through the grid points. The appropriate control volumes for the velocity components U and V (in the streamwise and cross-stream directions, respectively) are shown in Fig. 3. The two faces of the control volume around the velocity component U_e pass through the grid points P and E. The corresponding discretized momentum equation for U_e can be written as :

$$a_e U_e = \sum a_{nb} U_{nb} + b + (P_P - P_E) A_e \tag{3.2}$$

where the term b includes the source terms other than the pressure gradient, e.g. the drag force terms and the buoyancy term in the mixed convection problem. In Eq. (3.2) the subscript "nb" denotes a neighbor, and the summation is to be taken over all four neighbors. The pressure P_P and P_E denote those at points P ant E respectively, while A_e is the area or the width over which the pressure force act. The coefficient a's are functions of conductive and convective fluxes and can easily be obtained from the momentum equations like Eq. (2.11) and (2.12). The numerical values of the coefficients depend on the kind of differencing schemes chosen (e.g. power-law, hybrid or exponential schemes). A complete and detailed explanation of the differencing scheme with examples of how to obtain the coefficients in Eq. (3.2) is given in [27]. The results presented in the later chapters all uses the power-law scheme.

Equations similar to (3.2) can be written for the other components of velocity. For a given pressure field then, it is possible to solve the momentum equations. If U^* denotes the starred velocity field based on an estimated pressure field P^* then a starred momentum equation similar to Eq. (3.2) can be written as the following :

$$a_e U_e^* = \sum a_{nb} U_{nb}^* + b + \left(P_P^* - P_E^*\right) A_e \tag{3.3}$$

The guessed pressure field P^* will yield an estimated velocity field U^* and V^*. In general, this velocity field will not satisfy the continuity equation. The algorithm, therefore, calls for the derivation of a pressure correction equation which will result a correction to the velocity field that will ensure satisfaction of the continuity equation.

3.3.1 Pressure-correction equation :

If P' denotes the pressure correction and U' the corresponding correction to the velocity component U^* it follows that

$$P = P^* + P' \tag{3.4a}$$

$$U = U^* + U' \tag{3.4b}$$

Subtracting Eq. (3.3) from (3.2) and using the relationship given by Eq. (3.4) gives

$$a_e U'_e = \sum a_{nb} U'_{nb} + \left(P'_P - P'_E\right) A_e \tag{3.5}$$

Equation (3.5) is further simplified by assuming that the term $\sum a_{nb} U'_{nb}$ is negligible, thus yielding

$$U'_e = d_e \left(P'_P - P'_E\right) \tag{3.6}$$

where $d_e = A_e / a_e$. Formulas for the velocity-correction can be obtained by substituting Eq. (3.6) into Eq. (3.4b) to yield

$$U_e = U^*_e + d_e \left(P'_P - P'_E\right) \tag{3.7}$$

Similar formulas can be written for the other velocity components.

The pressure correction equation is obtained by substituting the velocity-correction formulas for U_e, U_w, V_n, and V_s (like Eq. (3.7)) into the discretized form of the continuity equation (3.1). The resulting equation is the pressure correction equation, which can be written as

$$a_P P'_P = \Sigma a_{nb} P'_{nb} + b \tag{3.8a}$$

where $a_I = (\rho A d)_i$ with I = E, W, N or S corresponding i = e, w, n or s (3.8b)

$$a_P = \Sigma a_I \tag{3.8c}$$

$$b = (\rho U^* A)_w - (\rho U^* A)_e + (\rho V^* A)_s - (\rho V^* A)_n \tag{3.8d}$$

It may be noted that the term b as given by Eq. (3.8d) represents the residual in the continuity equation when the starred velocity field is employed. The task of the pressure correction is to remove this residual. This is the essence of the algorithm called SIMPLE (Semi-Implicit Method for Pressure-Linked Equations).

Though the approximation introduced in the derivation of the P' equation (3.8) (the omission of the term $\sum a_{nb} U'_{nb}$) does not influence the correctness of the final solution, it may lead to rather exaggerated pressure corrections, and pressure underrelaxation becomes essential. Since the influence of the neighbor-point velocity corrections is removed from the velocity-correction formula (Eq. 3.7), the pressure correction has the entire burden of correcting the velocities, and this results into a rather poor convergence rate of the SIMPLE procedure. A revised version, SIMPLER (SIMPLE-Revised) was therefore formulated by Patankar [27]. Since the pressure-correction equation does a fairly good job of correcting the velocities, but a rather poor job of correcting pressure, in SIMPLER, a separate equation is derived for evaluating pressure.

3.3.2 Pressure equation :

From Eq. (3.2) a pseudovelocity $\hat{U}_e$ can be defined as

$$\hat{U}_e = \frac{\sum a_{nb} U_{nb} + b}{a_e} \tag{3.9}$$

The pseudovelocity $\hat{U}_e$ can be interpreted as the velocity that would prevail at point e of the control volume in the absence of the pressure force. To calculate $\hat{U}_e$, one does not require the pressure field but does require the values of the neighbor velocities U_{nb}. Equation (3.2) can now be written in terms of the pseudovelocity as

$$U_e = \hat{U}_e + d_e (P_P - P_E) \tag{3.10}$$

where d_e is as defined earlier in Eq. (3.6). Just as the pressure-correction equation (3.8) was derived from the continuity (Eq. (3.1)) by the substitution of equations like (3.7), the pressure equation can be similarly obtained by the use of Eq. (3.10) into the continuity equation. The result is a pressure equation very similar in form and content to the P' equation (3.8). The pressure equation is written as :

$$a_P P_P = \Sigma a_{nb} P_{nb} + b \tag{3.11a}$$

where the coefficients a_I's and a_P are given by Eq. (3.8b,c), and b is defined by

$$b = (\rho \hat{U} A)_w - (\rho \hat{U} A)_e + (\rho \hat{V} A)_s - (\rho \hat{V} A)_n \tag{3.11b}$$

Again, the term b in Eq. (3.11b) can be regarded as a "mass source" implied by the pseudovelocity field $\hat{U}$ and $\hat{V}$.

3.4 Discretized Energy Equation :

A discretized form of the energy equation can be obtained by integrating Eq. (2.13) over the control volume as shown in Fig. 2 to yield

$$a_P T_P = \Sigma a_{nb} T_{nb} \qquad (3.12)$$

where T is the temperature field and the coefficient a's depend on the differencing scheme which has been discussed in [27] in detail.

3.5 Calculation Procedure :

In the calculation procedure it is assumed that two of the neighboring values are known from their latest values. A tridiagonal matrix can then be formed from the discretization equations for the grid points along a chosen line. The tridiagonal matrix is solved by the Thomas Method. This solution procedure of updating values by traversing each line in sequence is continued by alternating directions. The idea is to bring information from the boundaries (like the heated wall) to the interior, faster.

The SIMPLER procedure can be outlined in terms of the calculation sequence as follows

1. Guess a velocity field U, V.
2. Calculate the coefficients (a's) in the momentum equations and hence obtain $\hat{U}$ and $\hat{V}$ from equations like (3.9).
3. Solve the pressure equation (3.11) for P.
4. Regarding this pressure field as P^*, solve the momentum equations such as Eq. (3.3) to obtain U^* and V^*.
5. Solve the pressure correction equation (3.8) for P'.

6. Correct the velocities via equations such as Eq. (3.7).
7. Calculate the coefficients in the energy equation and solve for the temperature field, Eq. 3.12.
8. Return to step 2 with the corrected velocity and temperature field and repeat the procedure until a convergence criteria is satisfied.

The convergence criteria include checks on relative changes of the dependent variables between consecutive iterations :

$$|(T_{new} - T_{old}) / T_{new}|_{max} \leq \varepsilon_1$$

$$|(U_{new} - U_{old}) / U_{new}|_{max} \leq \varepsilon_2$$

where the subscript "max" denotes the maximum value over all the grid points, "new" and "old" denote values in two consecutive iterations. The typical values for all the ε's are 10^{-4} . If the correct U and V field is achieved i.e. the continuity equation is satisfied, the residual in the pressure equation goes to zero. In the calculation this criteria for the residual was set to 10^{-5} .

Underrelaxation parameters were used in different subroutines to control the convergence of the solution field. Typical values for U and V are 0.7 and 0.8 for T, while P was not underrelaxed. Computations were performed using a 162 x 66 variable grid system in the streamwise and cross-stream directions respectively with the boundary conditions set according to the experiments which were being simulated. For example if the experiment had a packed inlet section the inflow velocity boundary condition was taken as fully developed. The length of the tube (or channel) was set equal to the length used in the experiments and an exit section (packed or empty) was

added if the experimental setup had one. The University of Hawaii's VAX 8550 computer has been utilized for the computations.

3.6 Grid Generation :

In the case of flow through a porous medium, velocity and temperature gradients are expected to be very large near a bounding surface because of the changes in porosity there. Refinement of the computational mesh near a wall is therefore mandatory, if the details of the flow and temperature fields are to be properly resolved. Lauriat and Prasad [26] have used a one dimensional exponential stretching type of coordinate transformation to distribute reasonably large number of grids near the wall. In this study the clustered (unequally spaced) R-grid points for the packed cylindrical tube case have been determined as a function of the equally divided transformed co-ordinate (χ) as follows :

$$R = H_R\left[1 - \frac{\{\exp[\zeta_r(H_R - \chi)] - 1\}}{[\exp(\zeta_r H_R) - 1]}\right] \qquad 0 \le \chi \le H_R \qquad (3.13)$$

where $\zeta_r > 1$ is the grid concentration factor. Larger values of ζ_r results in more grids near the walls. In Eq. (3.13) H_R is the upper limit of R the value of which depends on the definition of R. For example if $R = r/d_p$ then $H_R = 1/\gamma$ whereas if $R = r/D$ then $H_R = 1$. Note that for the Cartesian co-ordinate system the above equation can be easily modified.

To solve the governing equations numerically, it is also convenient to convert the semi-infinite streamwise domain ($0 \le X \le \infty$) into a finite one by a coordinate transformation. For this purpose the following coordinate transformation [30] was used :

$$X = \frac{1}{\zeta_x}\frac{\eta}{1-\eta} \qquad 0 \le \eta \le 1 \qquad (3.14)$$

where $\zeta_x > 0$ is a dimensionless constant which allows grid concentration near the entrance region where changes in the relevant dependant variables are greater than those in the downstream region. Larger values of ζ_x results in more grids in the inflow region. In equation (3.14), η is the equally spaced transformed axial coordinate whereas X is the clustered plane.

When the radial and axial porosity variations are assumed, grid refinement is required at the inlet and the exit section. For such cases the following grid transformation formulation has been adopted [92] :

$$X = X_L \frac{(\zeta_x + 1)Z^{(2\eta - 1)} - \zeta_x + 1}{2\{1 + Z^{(2\eta - 1)}\}} \qquad (3.15)$$

where $Z = (\zeta_x + 1)/(\zeta_x - 1)$. The grid stretching parameter $\zeta_x > 1$ clusters more grids near the boundaries as ζ_x approaches 1. In Eq. (3.15) the value of X_L depends on the length (L) of the packed bed and on the definition of X. For example if $X = x/d_p$ then $X_L = L/d_p$.

CHAPTER 4

EFFECT OF THE EMPIRICAL CONSTANTS

As mentioned earlier, a prime objective of this research was to determine, by a comparison with available experimental data, values of the empirical constants N, C_1, φ_a, A, B, C_d and ω, in the mathematical model for the prediction of the transport phenomena in porous media. It is befitting, therefore, to devote some time to study the effect of each of these constants on the fluid flow and heat transfer characteristics. A complete understanding of how the empirical constants effect the heat transfer and fluid flow characteristics would help in determining their values when comparing the numerical solution of the pressure drop and the heat flux with the available experimental data. In what follows, flow through a packed tube will be considered. Similar effects of the empirical constants will prevail for flow in a packed channel and therefore not presented to avoid repetition. A hydrodynamically fully developed flow with a uniform temperature profile at the inlet was assumed. The axial heat conduction has been neglected because it is expected to have negligible effect on the temperature field.

4.1 Effects of N, C_1, & φ_a on Properties of the Porous Medium :

4.1.1 Porosity :

Different values of N, C_1, and φ_a in equation (1.5a) generate different porosity variations from the wall as depicted in Fig. 4. Increasing C_1 with N and φ_a fixed causes a higher porosity at the wall, (curves a & b) and increasing N for the same

values of C_1 and φ_a causes the porosity to reach its asymptotic value within a shorter distance from the wall, as shown in curves b and c. It is also observed that for N = 2, $C_1 = 0.56$ (curve a) for which $\varphi_w = 0.56$, φ_w being the porosity at the wall, the asymptotic value of the porosity is reached within 2 ~ 3 particle diameters from the wall. On the other hand with N = 6, $C_1 = 1.4$ (curve c), for which $\varphi_w = 0.86$, the asymptotic value is reached within one particle diameter from the wall. Increasing the value of φ_a for fixed values of N and C_1 (curves c & d) not only increases the porosity away from the wall but is also expected to increase the overall bed porosity .

4.1.2 Permeability :

Since permeability depends on porosity per Eq. (2.3a), its value also depends on N and C_1. In Fig. 5 the normalized permeability (k / k_a), where k_a is the asymptotic value of the permeability, is plotted as a function of the distance normal to the wall. As seen before, for fixed values of N and φ_a, increasing C_1 results in higher porosity near the boundary. The large values of porosity near the wall results in large value of permeability (curves a & b) near the wall. On the other hand with C_1 and φ_a held constant, increasing N which results in a sharp drop in porosity, causes the permeability to reach its asymptotic value within a short distance from the boundary as shown in curves b and c. For a fixed value of N and C_1 (curves c & d) increasing the asymptotic value φ_a, for a fixed pair of N and C_1 values, increases the permeability since the overall porosity in the bed increases. Fig. 5 does not demonstrate this increase to a great extent because of the way the dependent variable is normalized.

4.1.3 Inertia coefficient :

From Eq. (2.3b) it can be seen that the inertia coefficient, f, varies as the inverse of porosity. In Fig. 6 the normalized inertia coefficient (f / f_a), where f_a is the asymptotic value of the inertia coefficient, is plotted as a function of the radial coordinate. For fixed values of N and φ_a, a higher value of C_1, which results in a higher porosity at the wall yields a smaller value of the said coefficient (curves a & b). On the other hand for the same values of C_1 and φ_a, the value of the inertia coefficient increases faster for a large value of N (curves b & c) since the porosity for the latter decreases faster to its asymptotic value close to the boundary. The effect of a higher value of φ_a, for fixed values of N and C_1, which increases the overall porosity in the bed is expected to decrease the value of the inertia coefficient. When the normalized inertia coefficient is plotted, this increase is not apparent (curve d which coincides with curve c).

4.1.4 Stagnant thermal conductivity :

The variation of the normalized stagnant thermal conductivity, (k_s / k_f), from Eq. (1.6), normalized with respect to the thermal conductivity of the fluid, k_f, for different combinations of N, C_1, and φ_a is plotted in Fig. 7. The effect of the empirical constants on the normalized stagnant thermal conductivity, is observed to be similar in nature to that of the normalized inertia coefficient.

4.2 Effects of N, C_1 and φ_a on Fluid Flow and Heat Transfer :

4.2.1 Velocity distribution :

The effect of N, C_1 and φ_a in Eq. (1.5a) on the velocity distribution in a packed cylindrical tube as a function of distance normal to the wall is shown in Fig. 8. The velocity distributions presented in this figure are calculated for the same flow rate and particle size. Since a higher value of C_1 (with N and φ_a fixed) results in large porosities near the wall, the velocity peak is consequently higher (curve b) as compared to a smaller value of C_1 (curve a). For fixed values of C_1 and φ_a, increasing N increases the rate of decay of porosity to its asymptotic value (see Fig. 4). The velocity profile for larger N also depicts the same behavior (curves b & c) in which the core value of velocity is reached within a short distance from the wall. Increasing φ_a for a fixed pair of N and C_1 values, has little effect on the velocity profile (curves c & d) - only the peak is slightly reduced, due to larger porosity values near the wall, with $\varphi_w = 0.96$ instead of $\varphi_w = 0.86$, where φ_w is the porosity at the wall.

4.2.2 Dimensionless pressure drop :

Fig. 9 depicts the effect of N, C_1 and φ_a on the dimensionless pressure drop parameter, f_D, as a function of the Reynolds number. The dimensionless pressure drop parameter is defined as $f_D = (\Delta p_f / L) / (\rho u_i^2)$ where L is the length of the packed tube and u_i is the mean flow velocity, Δp_f and ρ are the pressure drop and density of the fluid respectively. A larger pressure gradient is expected for the same flow rate through the bed if the average bed porosity decreases. This behavior is observed in Fig. 9. The values of N and C_1 represented by curves a and c results in similar average bed porosities for the same value of φ_a and are therefore almost identical. A decrease in

the value of N for a fixed pair of the values of C_1 and φ_a, decreases the required pressure drop because of an increase in the average bed porosity (curves b & c) in this case. A similar effect is observed when the asymptotic value of porosity, φ_a, is increased for a fixed pair of N and C_1 values (curves c & d). From Fig. 9 it can be observed that for an increase in the value of C_1 (with N and φ_a fixed) from 0.56 to 1.4 (curves a & b), i.e. by a factor of 2.5, the value of the dimensionless pressure drop parameter is lowered by 40%. Another important observation is the effect of the asymptotic value of porosity, φ_a, on the dimensionless pressure drop. An increase in the value of φ_a by 10% (0.36 to 0.4) represented by curves c and d, also seems to yield the f_D values that are 40% lower. The choice of the asymptotic value of porosity, φ_a in Eq. (1.5a) is therefore one of the most important among all the other empirical constants that are considered in this study.

4.2.3 Temperature distribution :

The dimensionless temperature profiles (at $L/r_0 = 2$) for different values of N, C_1 and φ_a are plotted in Fig. 10 as a function of the distance from the wall for a fixed Reynolds number, $Re_D = 10$, and particle to tube diameter ratio, $\gamma = 0.035$, (γ is referred to as the dimensionless particle diameter). The dimensionless temperature is defined as follows : $T = (t - t_h) / (t_i - t_h)$ where t_i and t_h refer to the inlet and hot wall temperatures respectively. Smaller values of C_1, which results in lower velocities near the wall (see Fig. 8), results in slower changes in temperature (curve a) as compared to the temperature profile for higher C_1 value (curve b) for the same values of N and φ_a. The effect of increasing N for fixed values of C_1 and φ_a (represented by curve c), has a mean effect between the previous two profiles since the velocity also shows the same

mean nature. Increasing the value of φ_a, for the same values of N and C_1, changes the value of the thermal conductivity and consequently the temperature distribution of the medium, as is reflected by curve d.

4.2.4 Dimensionless heat flux :

The effect of the empirical constants N, C_1 and φ_a on the Nusselt number is presented in Fig. 11 as a function of the streamwise coordinate measured from the inlet plane. The Reynolds number and the dimensionless particle diameter, γ, are held constant in this calculation. The effects of these constants on the local Nusselt number are similar to those on the temperature profiles. Comparing the curves a and b represented by the dashed and the dotted lines respectively, it is seen that a smaller value of C_1 for a fixed pair of values of N and φ_a, which results in a smaller slope in the temperature profile also results in the smaller heat flux at the wall (curve a). Increasing N (for constant C_1 and φ_a) results in the Nusselt number values (given by curve c) near the wall that are within the curves represented by the dashed and the dotted lines which also correspond to their respective temperature gradients (see Fig. 10). This condition also yields lower average heat flux. For fixed values of N and C_1, increasing φ_a decreases the peak velocity (see Fig. 8) thereby decreasing the heat flux (curve d).

4.3 Effect of the Ergun Constants A and B on Fluid Flow and Heat Transfer :

Various investigators have reported different values of the Ergun constants A and B. The value of A ranges from 150 to 215 while the value of B ranges from 1.75 to 1.92. In this section, the effects of these constants on the fluid flow and

heat transfer characteristics are investigated. In all of these computations, the values of $N = 6$, $C_1 = 1.4$ and $\varphi_a = 0.36$ have been used. The results of these computations are presented in Figs. 12-15.

4.3.1 Velocity distribution :

The effect of the Ergun constants A and B, on the velocity distribution in a packed cylindrical tube is presented in Fig. 12. The values of A (ranging from 150 to 215) and B (ranging from 1.75 to 1.92) are observed to have small effects on the velocity profiles. The peak velocity for A = 150 and B = 1.75 (curve a) is smaller than the others because of increased inertial resistance and overall bed permeability. The other set of values of A and B, depicted by curve b, c and d results in almost identical velocity profiles. Therefore, it can be concluded that the Ergun constants A and B (for the range of values considered) have negligible effect on the fluid velocity distribution for forced convection in a packed tube.

4.3.2 Temperature distribution and heat flux :

The dimensionless temperature profiles (at $L/r_0 = 2$) for the different values of A and B considered, do not show any marked difference as seen in Fig. 13. Since the temperature profiles for the different values of A and B have almost the same gradient at the wall the heat flux profiles are also similar as depicted in Fig. 14. It can be concluded that the Ergun constants have negligible effect on the heat transfer characteristics for forced convection in a packed tube.

4.3.3 Dimensionless pressure drop :

As shown in Fig. 15 a smaller values of A (e.g. A = 150), for the same B value, which gives larger permeability values, results in a lower pressure drop for a given flow rate (curves a & d). From the momentum equation (2.2) it can be seen that the effect of changing A and B is expected in the lower and higher Reynolds numbers respectively. This behavior can be observed by comparing the curves represented by a and d for the effect of A and curves c and d for the effect of B. From Fig. 15 it can be concluded that for the same value of B, decreasing A from 215 to 150 decreases the values of the pressure drop parameter by 30-40% for $Re_D < 10^3$. For $Re_D > 10^3$ the effect of decreasing A for a fixed value of B is observed to be of a lesser magnitude. Also for a fixed value of A, if B is changed from 1.92 to 1.75 (a 10% decrease) the value of the pressure drop parameter is lowered by 10% for $Re_D > 10^4$. For $Re_D < 10^4$ no effect can be observed on the values of the dimensionless pressure drop parameter if the value of B is changed with the value of A kept constant. It can be concluded, therefore, that the values of the Ergun constants A and B have a considerable effect on the dimensionless pressure drop parameter, f_D.

4.4 Effects of γ and Re_D on Fluid Flow and Heat Transfer :

In convective flow through a packed bed, the velocity and temperature distributions depend on the size of the particle and Reynolds number (or flow rate). Consequently, the pressure drop and heat transfer also depend on these parameters. In the following section the effect of these parameters will be examined qualitatively. In the numerical computations the exponential porosity function given by Eq. (1.5a) with N = 6, C_1 = 1.4 and $\varphi_a = 0.36$ and the Ergun constants A = 215, B = 1.92 have been

used. The present dispersion conductivity model, Eq. (1.11) (with $C_d = 0.15$ and $\omega = 3$) was employed in the energy equation. The dimensionless temperatures is defined as mentioned earlier in section 4.2.3.

4.4.1 Velocity distribution :

Fig. 16 shows the axial velocity as a function of the radial coordinate for forced convective flow in a packed tube at different Reynolds number (Re_D) and the dimensionless particle diameter (γ). For the same particle diameter (curves a & b) increasing the Reynolds number from 200 to 1000, increases the peak velocity. On the other hand for a fixed Reynolds number $Re_D = 1000$ increasing the dimensionless particle diameter $\gamma = 0.05$ to 0.1 decreases the peak velocity (curves b & c). This is caused due to an increase in bed porosity for the larger particle, and thereby permeability. To observe the channeling effect (mentioned before) the velocity profiles are replotted on a different dimensionless scale in Fig. 17. It can be seen that channeling effect becomes more pronounced as the particle size increases for the same Reynolds number (curves b & c). On the other hand for the same dimensionless particle diameter $\gamma = 0.05$, channeling effect becomes less pronounced as the flow rate increases from $Re_D = 200$ to 1000 (curves a & b).

4.4.2 Temperature distribution :

Fig. 18 shows the effect of Re_D and γ on the dimensionless temperature distribution as a function of the distance from the wall at a given downstream location. For the same particle size ($\gamma = 0.05$) increasing the Reynolds number from 200 to 1000 yields a steeper temperature gradient at the wall (curves a & b) thereby increasing heat

transfer. On the other hand for Re_D = 1000 a smaller particle seems to result in a steeper temperature gradient at the wall (curves b & c). From this figure it can be observed that the thermal entrance length increases with the flow rate.

4.4.3 Dimensionless heat flux :

Fig. 19 shows the local Nusselt number as a function of the axial coordinate, for a given length of the packed bed ($L/r_0 = 2$), for different values of Re_D and γ. The local Nusselt number follows the same trend as that of the temperature gradient discussed above. In Fig. 19 it can be seen that the Nusselt number increases if the Reynolds number increases from 200 to 1000 (curves a & b) for the same particle size, $\gamma = 0.05$. The Nusselt number is observed to decrease when the particle size increases from $\gamma = 0.05$ to 0.1 (curves b & c) for the same Reynolds number.

4.5 Effects of C_d and ω on Heat Transfer:

4.5.1 Temperature distribution :

The effect of the empirical constants C_d and ω in the present dispersion model given by Eq. (1.11) on the dimensionless temperature distribution is presented in Fig. 20 for Re_D = 1000 and $\gamma = 0.06$. The dimensionless temperatures are plotted as a function of the radial coordinate for a fixed axial location ($L/r_0 = 2$). A comparison of the profiles represented by curves a and c show that the temperature in the core of the packed bed increases as the value of C_d decreases from 0.15 to 0.1 with ω remaining constant. Similar trend is observed if the value of ω is increased from 3 to 4 for the same value of C_d (curves a & b).

4.5.2 Dimensionless heat flux :

The average Nusselt number, defined by Eq. (2.15), was calculated for different values of C_d and ω and are plotted in Fig. 21 as a function of Re_D for $\gamma = 0.06$, L = 0.3 m. From Fig. 21 it can be seen that at higher Reynolds numbers, for a fixed value of $C_d = 0.15$, increasing the value of ω from 3 to 4 decreases the average Nusselt number (curves a & b). The Nusselt number also seems to decrease (curves a & c) if the value of C_d is decreased for a fixed value of ω.

CHAPTER 5

RESULTS AND DISCUSSION

5.1 Values of the Empirical Constants N, C_1, C_2, φ_a, A, B, C_d and ω :

In the previous chapter, an analysis of the effects of the empirical constants were presented. Values of the empirical constants have been determined by a comparison of the numerical results of porosity, velocity, pressure drop and heat flux with available experimental data. The comparison show that good agreement between the numerical results and experiments can be achieved if the following values of empirical constants are employed : $N = 6$, $C_1 = 1.4$, $\varphi_a = 0.36$, $A = 215$, $B = 1.92$, $C_d = 0.15$ and $\omega = 3$ when the present dispersion model given by Eq. (1.11) is assumed, and the porosity function is assumed by the exponential function given by Eq. (1.5a, or b & c). The first five empirical constants were determined by a comparison of the porosity, velocity and the pressure drop data in a packed tube while the later two empirical constants were determined by comparing the numerical and observed heat flux data for forced convection in a packed tube and a channel.

When porosity is assumed to vary in the streamwise and the cross-stream directions, the exponential porosity function given by Eq. (1.5b,c) was employed as mentioned in Chapter 1. In this case the value of another constant, C_2, had to determined. Fortunately, the value of C_2 is limited by the maximum possible value of porosity in the entire bed, which is unity. A simple calculation gives $C_2 = 0.157$. In the

numerical computation in this study this value of C_2 has been assumed when the porosity variation was expressed by Eq. (1.5b,c).

Some authors [21,22,50,123] have used Eq. (1.5a) to represent the porosity function with N = 2 ~ 6, C_1 = 0.56 ~ 1, φ_a = 0.4 and A = 150, B = 1.75 in the momentum equation and found acceptable agreement of their computed heat flux with experimental data. None of the authors mentioned above have compared their numerical results of the pressure drop with experimental data. In the present study it has been observed that the computed pressure drop and velocity based on the above set of values donot agree with the data of Fand et al. [24,25] and Price [112]. If A = 150, B = 1.75 and φ_a = 0.4 are used and the exponential porosity function, Eq. (1.5a) is assumed with N = 2 to 6 and C_1 = 0.56 to 0.86, then the numerical result was found to underpredict the pressure data. If the exponential porosity function, Eq. (1.5a), is to be used to represent the porosity variation in the packed bed with N = 2, which has been used in many papers, the following values of the empirical constants have been found in this study to yield the best match for the numerical results with the experimental data of pressure drop [24,25] and velocity [112] : C_1 = 0.56, φ_a = 0.36, A = 215, B = 1.92. With these empirical constants in Eq. (1.5a), if Eq. (1.11) is assumed as the dispersion conductivity model, C_d = 0.13 and ω = 4 have been found to give the best possible match with the heat flux data.

In the following sections, the fluid flow and heat transfer results are also presented when the decaying cosine function given by Eq. (1.4) is employed as the porosity function and the dispersion conductivity model is represented by Eq. (1.11). The empirical constants involved in this case are φ_a, A, B, C_d and ω. The values of the first three empirical constants were found to remain the same as mentioned above by a

comparison of the fluid flow results, but the values of $C_d = 0.22$ and $\omega = 3$ were found to yield the best match for the heat flux data.

In order to facilitate the discussion in the sections that follow, the three combinations of porosity function and the present dispersion model (Eq. (1.11)), that are studied in this research, are classified as follows :

Case 1 : The exponential porosity variation, Eq. (1.5a or b and c) is assumed with

$N = 6$, $C_1 = 1.4$.

Case 2 : The exponential porosity function, Eq. (1.5a, or b and c) is assumed with

$N = 2$, $C_1 = 0.56$.

Case 3 : The decaying cosine function, Eq. (1.4) is used as the porosity function.

In all the cases mentioned above values of the Ergun constants A = 215 and B = 1.92 and the asymptotic value of porosity $\varphi_a = 0.36$ were used. Also if the porosity function is assumed by Eq. (1.5b,c) then the value of $C_2 = 0.157$ is used.

5.2 Comparison of Geometric Properties of the Porous media :

5.2.1 Porosity distribution :

A comparison of the exponential and oscillating porosity functions for a packed tube and a channel are presented in Figs. 22 and 23 respectively. The experimental data in these figures were obtained by Benenati and Brosilow [7]. The measured porosities show that about five oscillations (or five particle diameters) are required in order to reach the asymptotic porosity value, φ_a. In Figs. 22 and 23 curve c represent the porosity distribution assumed by the decaying cosine function (Case 3), Eq. (1.4). The dashed line (curve b) represents the exponentially decaying porosity function, Eq. (1.5a), with $N = 2$, $C_1 = 0.56$ (i.e. Case 2). These plots show that the

assumed porosity distribution given by Eq.(1.5a) with N = 6, C_1 = 1.4 (i.e. Case 1) represented by curve a, predicts the higher porosity near the wall extremely well. The oscillatory nature of the experimental porosity variations in the far field is predicted by Eq.(1.5a) as an average of the high and low porosities. It can also be concluded from Figs. 22 and 23 that though Eq. (1.5a) with Case 2 values (represented by curve b) predicts the porosity variation far from the wall quite well, it fails to achieve the large values of porosity near the boundary because of the smaller value of C_1 (see Fig. 4 for the effect of C_1 on porosity). Variation of any geometric property of the porous medium, especially porosity, is crucial to the heat transfer process because of the channeling effect as discussed in Chapter 1. It is therefore important to select a model for the porosity variation in the packed bed, that closely represents the experimentally obtained values. Choice of either the exponential function, Eq. (1.5a), with N = 6, C_1 = 1.4 (Case 1) or the decaying cosine function (Case 3), Eq. (1.4), seems to be promising. It is important to mention at this point that the values of the Ergun constants, A and B, should also be taken into account when comparing the effects of the different porosity functions on the pressure drop and velocity distribution in a packed column in order to obtain the desired porosity function. It is for this reason that an entire chapter (Chapter 4) has been devoted to study the effect of all the interacting empirical constants on the heat transfer and fluid flow characteristics.

The decaying cosine function Eq. (1.4) for the packed tube ($D/d_p = 20.3$) and the packed channel $\left(D/d_p \rightarrow \infty\right)$ is reported in Fig. 24 where d_p and D are the particle and tube diameters respectively. The only difference between these two curves is the value of l in Eq. (1.4) which determines the phase of the oscillation. From

Fig. 24 it can be concluded that the effect of l on the porosity distribution is rather small. Therefore Eq. (1.4) with l = 0.876 can safely be used even when $D/d_p \neq 20.3$.

5.2.2 Average or overall bed porosity :

The overall porosity of the entire packed bed as a function of d_p / D is presented in Fig. 25 for the oscillatory and exponential porosity functions. The computed values of the overall bed porosity was obtained by integrating the porosity function over the cross-section of a packed bed as follows :

$$\overline{\varphi} = \frac{2}{r_0^2} \int_0^{r_0} \varphi \, r \, dr \qquad (5.1)$$

where r_0 is the radius of the tube and r is the radial coordinate. The experimental data of Fand [25], Yagi [67] and Reichelt [42] presented in Fig. 25 show some scatter but the computed values (for Case 1, 2 and 3) represent good estimates. The scatter in the experimental data for the overall porosity value, is attributed to the method adopted in their evaluation.

5.3 Fluid Flow Results :

The momentum equations (2.11) and (2.12) (with the body force term neglected) with appropriate boundary conditions (depending on the experimental condition), constitute the governing equations for the hydrodynamically developing forced convection problem. On the other hand the governing momentum equation for the hydrodynamically fully developed forced convection problem is given by Eq. (2.17) with the boundary condition given by Eq. (2.18). Numerical solution for the

hydrodynamically developing forced convection flow problem was obtained by the application of the SIMPLER algorithm [27] on a non-uniform grid system. Grids were clustered near the wall region and also at the inlet and exit sections where steep velocity gradients are expected due to variations of porosity. The grids were generated as explained in Chapter 3. The numerical solution for the hydrodynamically fully developed forced convection problem was obtained by discretizing the governing momentum equation using the control volume based finite difference scheme and solving the resulting algebraic equations by the application of the Tri-Diagonal Matrix Algorithm (TDMA) on a uniform grid system with coordinate transformation in the cross-stream direction.

5.3.1 Velocity distribution :

Price [112] measured velocities at the exit section of a packed tube (D = 12 in.) for different flow rates (i.e. Reynolds number) of air flowing through the bed with length L = 9 in. (i.e. $L/r_0 = 1.5$). A pitot-static tube was placed at approximately 1/16 in. downstream of the exit face of the packed section. Since the velocity outside the packed section is expected to change with axial location [19], in the present study the exact experimental condition of Price [112] was simulated by adding an empty section (i.e without the solid matrix) at the exit of the packed section. The measured normalized axial velocity (normalized with the mean velocity at inlet) of Price [112] are presented in Fig. 26-28. The predicted velocity profile presented in Figs. 26-27 represent those at the section where the measurements were taken by Price (i.e. at x = L + 1/16 in. from the inlet) and also those at other downstream locations from the bed exit (0.5 in. and 1 in.). Calculations were performed for Case 1 (N = 6,

$C_1 = 1.4$) with $C_2 = 0.157$ and $\varphi_a = 0.36$ in the exponential porosity function, Eq. (1.5), with the Ergun constants A = 215, B= 1.92. An interesting observation from Figs. 26-27 is that a significant decrease in the peak velocity value takes place over a short axial distance just as the fluid leaves the packed bed. In Fig. 28 the predicted velocity profiles at the plane of measurement is presented for Case 1 (curve a). In the same figure curve b represents conditions for Case 2 (i.e. the exponential porosity function, Eq. (1.5a), with N = 2 and $C_1 = 0.56$) and curve c for Case 3 (i.e. with the porosity function assumed by the decaying cosine porosity function, Eq. (1.4)). When the porosity function is assumed by the damped cosine function the velocity profile (curve c) also exhibits an oscillatory nature as observed in Fig. 28. The measured velocity profile of Price [112] is also presented in Fig. 28 for the purpose of comparison. In Figs. 26-28 the exponential porosity function (i.e. Case 1 and 2) seem to yield a better agreement between the calculated and measured velocity as compared to the decaying cosine function (i.e. Case 3). A definite conclusion regarding the porosity function that results in the best agreement in this case cannot be made because of the fact that the velocity measurements of Price [112] are available at locations outside the region (relative to the wall) in which most of the changes have already taken place. Therefore, velocity measurements within one particle diameter of the containing walls (where the velocity seems to change drastically) are needed before any conclusion can be made on the porosity function and the empirical constants that gives the best match between computed and measured axial velocity data.

5.3.2 Hydrodynamic entrance length :

In order to obtain the hydrodynamic entrance length numerically, a uniform velocity distribution was assumed at the inlet of the packed section. Hence the boundary conditions given by Eq. (2.14) apply to the momentum equation. In this case the exponential porosity function, Eq. (1.5b,c) was employed with N = 6, C_1 = 1.4 (i.e. Case 1) with C_2 = 0.157, φ_a = 0.36 and A = 215, B = 1.92. The hydrodynamic entrance length, L_{hy} (normalized with respect to the particle diameter) for the flow of air in a packed tube was computed for different ratios of particle to tube diameter and for different Reynolds numbers, Re_d (based on the particle diameter). A sufficiently long packed section (L = 0.5 m) was assumed in the numerical solution to ensure a hydrodynamically fully developed condition at the exit. In the numerical solution a hydrodynamically fully developed condition was assumed if the velocities at consecutive axial locations at any given cross-section did not change by 0.01 percent. The results of the predicted hydrodynamic entrance lengths for γ = 0.024, 0.035, 0.045, 0.071 and 0.097 are presented in Table 1, which shows that for $0.024 \leq \gamma \leq 0.097$ and $1 \leq Re_d \leq 250$ the hydrodynamic entrance length decreases with increasing Reynolds number and then attains a constant value. This type of behavior of the entrance length is typical in classical turbulent flow in a tube. In the case of flow through a packed bed, mixing of fluids in the pores take place even at very slow flow rates resulting in the flow to become fully developed over a short distance from the inlet section. This mixing phenomena in the pores increases as the flow rate increases thereby decreasing the hydrodynamic entrance length up to a certain value beyond which it remains constant. From Table 1 it can also be concluded that for larger particles (i.e. large values of γ) the entrance length is longer for a given Reynolds

number (or flow rate). From the numerical results the hydrodynamic entrance length for flow in a packed-sphere bed inside a tube, is observed to be about 20 particle diameters long for $\gamma = 0.024$ and is about half as long for $\gamma = 0.071$, which is contrary to assumptions of L_{hy} being of the order of one in most papers.

From Table 1 an interesting observation is the Reynolds number independence regions of the hydrodynamic entrance length for $Re_d < 4$ ($\gamma = 0.071$ and 0.097). When the Reynolds number varies from 1 to 4 the inertial resistance increases but the Darcian resistance decreases. Since these two resistances have opposite effects on the flow, the velocity profiles in this Reynolds number range remain practically unchanged resulting in little or no change in the hydrodynamic entrance length. At smaller and higher flow rates the hydrodynamic entrance length can therefore be assumed to be constant (but different). Caution is advised when using the predicted hydrodynamic entrance length because it depends on the criteria that has been used to determine it (in this study the criteria was 0.01% as mentioned in this section). A different value for the criteria would result in a different value of L_{hy}. Therefore a careful experimental investigation is required to substantiate the findings of the present numerical computations for the hydrodynamic entrance length.

5.3.3 Pressure drop :

A considerable amount of experimental work has been performed on pressure drop in packed tubes [24,25,106]. In particular Fand et al. [24,25] have measured pressure drop of water flowing through a packed tube having particle/tube diameter ratio ranging from 0.024 to 0.71. Fig. 29 is a comparison of the predicted and experimentally determined dimensionless pressure drop parameter f_D as a function of

Re_D (both based on the tube diameter, D) in a packed tube for $\gamma = 0.024, 0.035, 0.045, 0.071$ and 0.097 which correspond to Fand et al.'s experimental conditions [24,25]. The dimensionless pressure drop parameter f_D is defined as $f_D = (\Delta p_f / L) D / \rho u_i^2$ where L is the length of the packed tube and u_i is the mean velocity at the inlet, Δp_f and ρ are the pressure drop and density of the fluid respectively. The lines in Fig. 29 represent the predicted pressure drop with porosity approximated by the exponential function, Eq.(1.5b,c), with N = 6, $C_1 = 1.4$ (i.e. Case 1) and $C_2 = 0.157$, $\varphi_a = 0.36$ and A = 215, B = 1.92. From this plot it is observed that the predicted pressure drop agrees very well with the experimental data if these empirical constants are used. It should be mentioned at this point that the predicted pressure drop for the hydrodynamically fully developed and the developing forced flow cases are almost identical and are therefore not presented separately. Therefore, it can be concluded that the hydrodynamic entrance length has little effect on the pressure drop. In Fig. 30 the effect of using different porosity function relationship on the dimensionless pressure drop, f_D, as a function of the Reynolds number, Re_D, is presented for $\gamma = 0.035$ and $\gamma = 0.097$. The solid lines (curve a) in Fig. 30 represent the f_D values for Case 1 ; the dashed lines (curve b) are for Case 2 (i.e. exponential porosity variation, Eq. (1.5b,c), with N = 2, $C_1 = 0.56$) ; and the chain-dashed lines (curve c) represents f_D values for Case 3 (i.e. porosity assumed by the decaying cosine function, Eq. (1.4)). It can be concluded from Fig. 30 that the porosity variations given by Eq. (1.4) and Eq. (1.5b,c) are equally valid for predicting the pressure drop in a packed-sphere bed in a tube for $10 \leq Re_D \leq 10^4$.

In the absence of any reliable experimental pressure drop data for flow in a packed channel, only numerical result of the dimensional pressure drop parameter,

f_H, as a function of the Reynolds number, Re_H, (both based on the the height of the channel or plate separation distance, H) are presented in Fig. 31 for $\gamma = 0.06$ and 0.12. The dimensionless pressure drop parameter, f_H, in the case of flow through a packed channel is defined as $f_H = (\Delta p_f / L) H / \rho u_i^2$ where L is the length of the channel, H is the plate separation distance, u_i is the mean fluid velocity at inlet, ρ and Δp_f are the densities and average pressure drop of the fluid respectively. From Fig. 31 it can be observed that Cases 1 and 2 result in almost the same profiles of f_H for $10 \leq Re_H \leq 10^4$. The decaying cosine function, (Case 3), on the other hand predicts a higher f_H value for $Re_H < 10^3$ and lower values for $Re_H \geq 10^3$. The sudden drop in the value of f_H around $Re_H = 500$ is attributed to the sinusoidal nature of the porosity function.

A comparison of the predicted dimensionless pressure drop in a packed tube and a channel for $\gamma = 0.035$ and 0.097 as a function of Reynolds number is presented in Fig. 32 for the condition in Case 1. From this plot it can be observed that for small γ ($\gamma = 0.035$) at the same Reynolds number a greater pressure drop (about 6%) is required for flow through a packed channel than through a packed tube. Whereas for $\gamma = 0.097$ an even greater pressure drop (about 20%) is required for flow through a packed channel. This implies that the pressure drop does not dependent on the geometry of the packed bed for small values of γ whereas for large γ the geometry is important.

5.4 Heat Transfer Results :

Having obtained the hydrodynamic field, the next step is to obtain the temperature field by solving the energy equation. From the temperature distribution, the heat flux and thereby the Nusselt number can be calculated. The Nusselt number and

the heat flux for the packed tube and the packed channel are defined in Eqs. (2.15) and (2.16) respectively. The governing energy equation for the simultaneously developing forced convection problem is given by Eq. (2.13) with appropriate boundary condition (depending on the experimental conditions). The numerical solution for the energy equation for this problem was obtained by the application of the SIMPLER algorithm on a non-uniform grid system as in the case of the momentum equation. For the hydrodynamically fully developed and thermally developing forced convection problem the governing energy equation (with the boundary layer approximation) is given by Eq. (2.19) with the boundary conditions as in Eq. (2.20). The governing equation in this case was discretized using the finite difference scheme with the convective term expressed as an upwind difference. The resulting sets of algebraic equations were solved with the TDMA. The marching technique was used to obtain the temperature profiles at each axial location by traversing the solution procedure from inlet to the exit section.

As mentioned earlier, the empirical constants C_d and ω in Eq. (1.11) have been determined by a comparison of the experimental and numerical values of the Nusselt number (Nusselt number will also be referred to as the dimensionless heat flux). Hence these results will be presented first followed by the temperature distribution. Some comments need to be made at this point on the choice of the tube diameter, D, or the plate separation distance, H, in the definition of the Nusselt number and the Reynolds number in the case of the circular and flat (channel) geometries. When comparison between two identities are made a common basis should be used. For example, if the effect of the particle diameter on the velocity profile or the heat flux is to be studied, the Reynolds number or the Nusselt number should not be calculated

with the particle diameter as the characteristic length. To make a fair comparison it is quite logical to use an independent parameter, e.g. the tube diameter or the plate separation distance as the characteristic length. Another choice of the characteristic length for the case in question is the length of the tube (or channel) which has been suggested by Chrysler and Simons [33]. But the choice of permeability as the characteristic length, also suggested by Chrysler and Simons [33], is not recommended because of the dependence of the permeability on the particle diameter per Eq. (2.3a).

In this research it has been found that a dispersion coefficient $C_d = 0.15$ and the Van Driest damping factor $\omega = 3$ results in the best match between numerical and experimental results of the heat transfer characteristics if the dispersion conductivity given by Eq. (1.11) and the exponential porosity function, Eq. (1.5b,c) are considered with N = 6, $C_1 = 1.4$ (i.e. Case 1) with $C_2 = 0.157$, $\varphi_a = 0.36$ and A = 215, B = 1.92. On the other hand for Case 2 (i.e. if the values of N = 2, $C_1 = 0.556$ are used in Eq. (1.5) with the values of the other empirical constants as mentioned above), the best match between the predicted and experimental heat flux data can be obtained if $C_d = 0.13$ and $\omega = 4$ are used in the dispersion conductivity model given by Eq. (1.11). If the decaying cosine porosity function, Case 3, was assumed (i.e. Eq. (1.4) then $C_d = 0.22$ and $\omega = 3$ have been found to be the appropriate values of the empirical constants to be used in Eq. (1.11). Values of C_d and ω that were used in the numerical computations for the different cases studied can be summarized as follows :

a) for Case 1 : $C_d = 0.15$ and $\omega = 3$,

b) for Case 2 : $C_d = 0.13$ and $\omega = 4$ and

c) for Case 3 : $C_d = 0.22$ and $\omega = 3$.

In evaluating the values of the empirical constants C_d and ω, comparison was made with the observed Nusselt number and not the measured temperature distribution. The reason for this is that temperature measurements in a porous medium is extremely difficult without affecting the flow (even by using small diameter probes). Also it is not assured whether the fluid or the solid temperature is being measured, keeping in mind that under non-thermal equilibrium conditions these two temperatures will be different. Therefore, temperature measurements are not so reliable for comparison purposes. On the other hand the observed heat flux is calculated from measured power input to the heat source. If heat losses are minimized (or taken into account) the heat flux measurements are usually of much greater accuracy than the temperatures.

In the following sections results of the computed heat flux are also presented when the dispersion conductivity models by Kuo and Tien [121] and Koch and Brady [122] are used for Case 1 conditions. Since the latter model [122] was not derived with the effect of variable porosity taken into account (as are most of the dispersion models), it is expected to be valid for small γ.

Before going into the presentation and discussion of the heat transfer results, the reasons for choosing the experimental data of Verschoor and Schuit [17] for comparison purposes is stated as follows. It is true that in the literature one can find numerous data for the heat flux in the case of forced convection in a packed tube. The question is which of these data are reliable and how complete are the information. For example, many authors do not report the measured heat flux data, inlet and outlet bulk mean temperatures. The inlet and outlet temperatures were not usually reported because it was assumed that the flow is thermally fully developed. If the reported experimental

data includes the inlet and outlet temperatures and the heat flux or the heat transfer coefficient, it is possible to assess the reliability of the experimental data in question by simple heat balance calculations. In the present study the experimental data of Verschoor and Schuit [17] was found to be very reliable and complete, and therefore was used for comparison with the numerical solution. It should be mentioned that a good estimation of the empirical constants, in this case C_d and ω in Eq. (1.11) can only be made if the source of the experimental data is reliable. Conversely, if the reliability of data cannot be assessed then a comparison with it would lead to inaccurate values of the empirical constants.

An error analysis of the computed and experimental data for the Nusselt number is reported in this section to quantify the difference between the observed and calculated heat flux data for forced convection in a packed bed. The Root Mean Square Error (RMSE) which is used as the criterion for the comparison in this analysis is expressed as follows :

$$RMSE = \sqrt{\frac{1}{n} \Sigma E_i^2}$$

where, n refers to the number of data points and the error E_i is defined as

$$E_i = \frac{X_{th} - X_{exp}}{X_{exp}}$$

where X_{th} and X_{exp} are the theoretical and experimental values of the Nusselt number.

5.4.1 Thermally developing forced convection in a packed tube :

(A) Comparison with Verschoor and Schuit's as well as Leva's experimental data :

Experiments on forced convection in a packed tube at uniform wall temperature were carried out by Verschoor and Schuit [17] and by Leva [52]. Although

temperature distributions were not measured in these experiments, the dimensionless heat flux data was reported and are presented in Figs. 33-37 for Verschoor and Schuit's experiments [17] and Fig. 38 for Leva's experiments [52]. Since no packed calming section was used at the inlet in Verschoor and Schuit's [17] or Leva's [52] experiments, the numerical solution in the present study is based on a simultaneously developing flow with a uniform velocity assumed at the inlet of the heated packed column.

The experimental data of the Nusselt number as a function of Reynolds number (both based on the tube diameter), for $\gamma = 0.06, 0.1, 0.101, 0.12$ and 0.14 which correspond to the experimental conditions of Verschoor and Schuit [17] for air/glass sphere and air/chrome steel sphere, are presented in Fig. 33. The lines in this figure represent the computed Nusselt number corresponding to Verschoor and Schuit's experimental conditions. For the purpose of comparison the numerical solution of the energy equation without the dispersion term is also included in Fig. 33 for $\gamma = 0.1$. From this plot it can be seen that dispersion plays an important role in the heat transfer process for forced convection in a packed bed and therefore must be included in the energy equation. From Table 2 it can be seen that for the air/glass sphere system the Root Mean Square Error (RMSE) between the experiments of Verschoor and Schuit [17] and the present numerical solution is less than 10%. The RMSE for the air/chrome steel sphere system is within 16% for $\gamma = 0.12$ and 19% for $\gamma = 0.14$. Good agreement between the experimental and computed values of the heat flux can be concluded from Fig. 33. It should be mentioned here that the computed results are based on the assumption of local thermal equilibrium. The thermal equilibrium assumption is valid if the thermal conductivities of the solid and the fluid media are of

the same order of magnitude. Therefore, if the thermal conductivity ratio of the fluid and the solid, $\lambda = k_f/k_p$ is close to unity, the computed results are expected to closely predict the temperature in the packed bed. For the air/glass system the thermal conductivity ratio $\lambda = 0.03$, whereas for the air/chrome steel system $\lambda = 0.0006$. Therefore, the numerical solution is expected to predict the Nusselt number better for the air/glass sphere system than the air/chrome steel sphere system. This explains the reason for the larger error between the numerical and experimental values of Nusselt number for the air/chrome steel system as compared to the air/glass sphere system.

From Fig. 33 the effect of the ratio of the particle to the tube diameter, γ $(0.06 \le \gamma \le 0.12)$ and the length of the heated tube, L, $(0.21 \text{ m} \le L \le 0.3 \text{ m})$ is observed to be small on the dimensionless heat flux results (both predicted and observed), for $10^3 \le Re_D \le 10^4$ when the solid particles are comprised of the glass spheres. On the other hand for the air/chrome steel sphere system, $\gamma = 0.12$, $L = 0.21$ m and $\gamma = 0.14$, $L = 0.3$ m, the predicted and observed results of the Nusselt number is smaller for the larger particle for $10^3 \le Re_D \le 10^4$. Another observation from the same figure is the tendency of the Nusselt number to collapse to one line (i.e. independent of material of the solid particle) for $Re_D > 10^4$ (in the case of the observed and numerical data). From Fig. 33 the effect of L on the Nusselt number can be studied by comparing the predicted values for $\gamma = 0.101$, $L = 0.26$ m (curve c) and $\gamma = 0.1$, $L = 0.21$ m (curve b). It can be observed that for similar particle size the effect of using a heated tube that is 25% shorter increases the heat flux by about 10%. The observed values for this case on the other hand show a 4% increase in the heat flux.

To examine the effect of γ on the Nusselt number, Fig. 33 is replotted in Figs. 34 for $\gamma = 0.06$ and 0.12 for $L = 0.3$ m. From Fig. 34 it can be observed (both

experimental data and numerical results) that for a given Reynolds number, Re_D, the particle size has little effect on the Nusselt number (not heat flux). From this figure the predicted results of the Nusselt number for $\gamma = 0.06$ and 0.12, an increase of only 1-2 % can be observed for the range of $10^3 \leq Re_D \leq 10^4$. The effect of λ (the ratio of the fluid to solid thermal conductivity) on the Nusselt number can be studied from Fig. 35 in which the dashed line (curve b) represents the predicted Nusselt number for $\gamma =$ 0.12, L = 0.21 m for air/chrome steel sphere system and the solid line (curve a) the Nusselt number for $\gamma = 0.12$, L = 0.3 m for the air/glass sphere system. Since the effect of the length of the packed heated tube on the observed Nusselt number is seen to be small, a comparison of the effect of λ on the Nusselt number can be made from this figure. The experimental data of Verschoor and Schuit [17] which correspond to the above mentioned predicted results are also included in the same graph as a comparison. The effect of using metal spheres as compared to glass spheres is seen to increase the Nusselt number at lower Reynolds number. On the other hand the effect of using metal spheres seems to be small at higher flow rates. No definite conclusion can be made to quantify the amount of increase in heat flux from this plot because the experiments (and predictions) were not performed at identical boundary conditions of temperature for the two sets of data. The effect of λ on the Nusselt number will be discussed later in which the numerical simulations was performed for the same boundary values of temperature.

The effect of using the different porosity functions (Case 1, 2 and 3) on the Nusselt number is presented here. In Figs. 36 and 37 the predicted and observed data of the Nusselt number for $\gamma = 0.06$ and 0.101 (air/glass sphere system) which correspond to Verschoor and Schuit's experimental conditions is presented. From Figs. 36 and 37 it can be observed that though Case 1, 2 and 3 predict the Nusselt

number for $\gamma = 0.06$ quite well, for $\gamma = 0.12$ Cases 2 and 3 underpredict the dimensionless heat flux values, especially with increasing Reynolds numbers. Therefore, Case 1 i.e. the exponential porosity variation, Eq. (1.5b,c) with N = 6, $C_1 = 1.4$ along with the present dispersion model given by Eq. (1.11) with $C_d = 0.15$ and $\omega = 3$ offers the best solution in predicting the dimensionless heat flux in a packed tube.

A comparison of the results based on the present dispersion model and those of Kuo and Tien [121] and Koch and Brady [122] is presented in Fig. 38 where the numerical solutions (for Case 1) were carried out corresponding to Verschoor and Schuit's experimental condition [17]. The dispersion models proposed by Kuo and Tien [121] and by Koch and Brady [122] is seen to underpredict the dimensionless heat flux results and the deviation seem to increase with increasing Reynolds number. From Fig. 38 it can be concluded that the present dispersion model given by Eq. (1.11) with $C_d = 0.15$ and $\omega = 3$, along with the exponential porosity function with N = 6, $C_1 = 1.4$ (i.e. Case 1) with $C_2 = 0.157$, $\varphi_a = 0.36$ and A = 215, B = 1.92, results in the best match between the computed and observed Nusselt number for forced convection in a packed tube.

In Fig. 39 the experimental results of Leva [52] for $\gamma = 0.086$ and 0.11 are presented for the Nusselt number as a function of the Reynolds number. The numerical solutions are also included in this plot for the purpose of comparison. In the numerical simulation the exponential porosity function was assumed as in Case 1 with $C_d = 0.15$ and $\omega = 3$ in the present dispersion conductivity model, Eq. (1.11). The discrepancy between the numerical results of Nusselt number and the experimental data is attributed to large heat losses and difficulty in measuring the packed bed exit bulk

mean temperature in Leva's experiments. This comment was also made by Verschoor and Schuit [17], Hennecke and Schlunder [75], Quinton and Storrow [61] and others. As observed in Fig. 39 the deviation between the experimental data and the numerical solutions increases with decreasing Reynolds number. This happens particularly in tubes that are very long as for example the one used by Leva [52]. As the outlet temperature approaches equality with the wall temperature, small errors of exit temperature measurement become magnified in the subsequent calculations, leading to increasingly low values of the heat transfer coefficient with decreasing flow rates [61]. An error analysis for the experimental and predicted Nusselt number is presented in Table 3 which shows that the Root mean square error is 15% for $\gamma = 0.086$ and 11% for $\gamma = 0.11$.

In the present study agreement between computed and the experimentally determined Nusselt number for forced convection in a packed tube is found to be good for $\gamma < 0.15$. For $\gamma \geq 0.15$ especially at high Reynolds numbers, the predicted Nusselt number (Case 1) appears to be lower than the experimental data as shown in Fig. 40 for $\gamma = 0.151$ for air/glass sphere system corresponding to Verschoor and Schuit's experiments [17]. The Root mean square error for this case is 25%. This discrepancy may be attributed to the fact that the assumption of a continuum is inaccurate for $\gamma \geq 0.15$.

(B) Comparison with Plautz and Johnstone's experimental data :

Plautz and Johnstone [1] have carried out an experiment on forced convection of air in a cylindrical tube at uniform wall temperature packed with glass spheres. Since a packed calming inlet section was used in the experiment, numerical

solutions to simulate this flow condition have been performed using a fully developed velocity profile as the inlet velocity distribution. Plautz and Johnstone's experimental data [1] for dimensionless temperature distribution $T = (t - t_h)/(t_i - t_h)$ (with t_h and t_i denoting the wall and inlet temperatures respectively) at different downstream location for $\gamma = 0.088$ and $Re_D = 1.1 \times 10^3$ (Reynolds number based on the tube diameter) is presented in Figs. 41-45. Results of the numerical solution for the dimensionless temperature distribution are also plotted in the same graph for comparison purposes for Case 1, 2 and 3 and for two other dispersion models by Kuo and Tien [121] and by Koch and Brady [122]. In Fig. 41 the computed results are based on Case 1 and the present dispersion conductivity model given by Eq. (1.11) with $C_d = 0.15$ and $\omega = 3$. As shown in the figure the calculated temperature profiles are in fair agreement with Plautz and Johnstone's experimental data [1]. It should be noted that the calculated temperatures are volumetric averaged quantities while the experimental data are microscopic fluid temperature measurements and thus a perfect agreement is not expected.

Numerical results of the temperature distribution were also obtained for Case 2 (i.e. the exponential porosity function, Eq. (1.5b,c) with $N = 2$, $C_1 = 0.56$) and the present dispersion model with $C_d = 0.13$ and $\omega = 4$. As mentioned earlier the values of C_d and ω were obtained by comparing the numerical results and the observed data for the dimensionless heat flux. The predicted and observed temperature distribution is presented in Fig. 42. From Fig. 42 it can be concluded that the predicted temperature distribution for Case 2 is of the same nature as obtained for Case 1 (i.e. the exponential porosity function with $N = 6$, $C_1 = 1.4$). In Fig. 43 a comparison of the predicted and observed temperature profiles corresponding to Plautz and Johnstone's [1]

experiments, is presented for the decaying cosine porosity function i.e. Case 3, and the present dispersion model, Eq. (1.11) with $C_d = 0.22$ and $\omega = 3$. The agreement between the observed and numerical results of temperature for this case seems to be worse.

As mentioned earlier two other dispersion models by Kuo and Tien [121] and by Koch and Brady [122] are analyzed in this study to ascertain their accuracies. Using the dispersion model of Kuo and Tien [121] Eq. (1.12) with the exponential porosity function, i.e. Case 1, the experimental conditions of Plautz & Johnstone [1] was numerically simulated. A comparison of the numerical solution and experimental data of the temperature distribution is presented in Fig. 44. The temperature profile with Kuo and Tien's dispersion model [121] seems to overpredict the bed temperatures. Fig. 45 is a comparison of temperature data obtained by Plautz and Johnstone [1] with computed temperature profiles based on Koch and Brady's [122] dispersion model, Eq. (1.13) (also under Case 1 conditions). Similar over-prediction of the bed temperature is observed when Koch and Brady's dispersion model [122] was employed in the numerical solution of the energy equation. From the predicted temperature profiles presented in Figs. 41-45, it can be seen that none of the porosity functions or dispersion models that has been assumed in this study, is able to predict the temperature distribution of the experiments of Plautz and Johnstone [1] well. The closest prediction is seen to be for Case 1 (Fig. 41) with the present dispersion conductivity model given by Eq. (1.11) with $C_d = 0.15$ and $\omega = 3$.

5.4.2 Thermally developing forced convection in a packed channel :

Cai [116] conducted an experimental investigation on forced convection of Freon (referred to as R-113 in this study) in a packed channel of 0.46 m in length, maintained at temperatures $t_h \sim 38$ °C and $t_c \sim 23$ °C, referring to the hot and cold wall temperatures, and separated by a distance H (which will be referred to as the plate separation distance from hereon). Temperature distribution in the packed channel at five downstream locations i.e. at x = 6.35, 92.1, 181.0, 270.0, and 451.0 mm from the inlet section were measured using J-type thermocouple probes (0.81 mm in diameter). Two types of spherical balls - glass (3, 5 and 6 mm in diameter) and chrome steel (6.35 mm in diameter) were used as the porous matrix and the measured temperature and heat flux were reported [116].

A numerical simulation of Cai's experiments was carried out in this study with the inlet velocity distribution taken as fully-developed (because of the presence of a packed calming inlet section). Figure 46 depicts the variation of the Nusselt number, Nu_H (defined in Eq. (2.16), in a packed channel as a function of the Reynolds number, Re_H, for $\gamma = 0.06$ and 0.12 for the R-113/glass sphere system and the R-113/chrome steel sphere system. The lines in Fig. 46 represent the numerical solutions corresponding to Cai's experiments [116]. It appears that as the Reynolds number increases the agreement between the numerical and experimental results [116] of the Nusselt number become worse for the R-113/glass sphere system. On the other hand good agreement is observed for the R-113/chrome steel sphere system (curve c). This is contrary to what is expected and also observed in the case of forced convection in a packed tube presented earlier. The value of the thermal conductivity ratio, λ, for the R-113/glass sphere system is 0.071 whereas for the R-113/chrome steel system

$\lambda = 0.0017$. Therefore under the assumption of thermal equilibrium as discussed earlier (in section 5.4.1) the R-113/glass sphere system is expected to yield better agreement with the computed Nusselt number. One of the important reasons for the discrepancy in the computed and observed Nusselt number data of Cai [116] could have resulted from loose packing of the glass spheres in the test section in his experiments. A large void space was observed in the inlet section at higher flow rates. This may have caused the velocity profile to become distorted in the test section resulting in a problem that was not numerically simulated. Also poor measurement techniques and instrumentation used in the measurement of the hot and cold wall temperatures may have been a contributing factor. An error analysis of the computed and experimental data for the Nusselt number for forced convection of R-113 in a packed channel for the glass and chrome steel sphere systems is presented in Table 4.

The effect of using the different porosity functions (Case 1, 2 and 3) on the computed Nusselt number for forced convection in a packed channel are presented in Figs. 47 and 48 for $\gamma = 0.06$ and 0.12 (air/glass sphere system) respectively, which correspond to Cai's experimental conditions. From Figs. 47 and 48 it can be observed that Case 1 and 2 predict the Nusselt number data quite well for $\gamma = 0.06$ and 0.12. Computed results of the Nusselt number for Cases 3 assumption is seen to underpredict the dimensionless heat flux values, especially with increasing Reynolds numbers. Therefore, Case 1 and 2, i.e. the exponential porosity variation, along with the present dispersion model given by Eq. (1.11) offers the best solution in predicting the dimensionless heat flux in a packed channel.

A comparison of the computed (for Case 1) Nusselt number based on the present dispersion model and those of Kuo and Tien [121] and Koch and Brady

[122] with the experimental data is presented in Fig. 49. The dispersion model proposed by Kuo and Tien [121] is seen to underpredict the dimensionless heat flux. At higher Reynolds numbers the discrepancy is greater. The dispersion model of Koch and Brady [122] is seen to overpredict the dimensionless heat flux results for any given Reynolds number. From Fig. 49 it can be concluded that the present dispersion model given by Eq. (1.11) with $C_d = 0.15$ and $\omega = 3$, along with the exponential porosity function with $N = 6$, $C_1 = 1.4$ (i.e. Case 1) with $C_2 = 0.157$, $\varphi_a = 0.36$ and $A = 215$, $B = 1.92$, results in the best match between the computed and observed Nusselt number.

A comparison of Cai's temperature data for R-113/glass sphere system ($\gamma = 0.06$) with predicted temperature distribution for Case 1 and $C_d = 0.15$ and $\omega = 3$ in Eq. (1.11) at $Re_H = 4161$ and 16685 are presented in Figs. 50 and 51 respectively. In Figs. 52-54 similar comparisons of the observed and computed temperature distribution (based on Case 1) for $\gamma = 0.12$ at $Re_H = 2407$, 8228 and 16613 for the R-113/glass sphere system are plotted. In Figs. 55-57 the observed and predicted temperature profiles for R-113/chrome steel system at $Re_H = 2148$, 8301 and 16571 are presented. From Figs. 50-57 the predicted temperatures are seen to be less than the measured values near the heated wall, especially at distances far from the entrance section. The discrepancy seem to become worse as Reynolds number increases (compare Figs. 50 and 51 for example). It can also be observed that the differences in the predicted and observed temperatures are smaller on the cold side but larger on the hot side of the channel. This is because the observed temperatures are not anti-symmetric about the centerline of the channel which should have been obtained in an asymmetric heating condition at steady state. Some of the reasons for the poor

agreement between the observed and the predicted temperatures are as follows :

a) the flow has not attained steady state,

b) variable property effect may be more important near the hot wall,

c) in porous media problems, temperature measurements using probes is not the best method to be used because the size of the probes may influence the flow thereby changing the temperature field. Moreover, no guarantee can be given as to the location of the measurements.

In order to compare the effect of the remaining two porosity functions (i.e. Cases 2 and 3) on the temperature distribution, a numerical computation was conducted. A comparison of Cai's temperature data for the R-113/glass sphere system ($\gamma = 0.06$) with the computed temperatures at $Re_H = 4161$ is presented in Fig. 58 for Case 2 (i.e. exponential porosity function, Eq. (1.5b,c) with $N = 2$, $C_1 = 0.556$). The agreement between the numerical and observed temperature is still not so good. Similar trends are observed for $\gamma = 0.12$ and $Re_H = 8228$ (R-113/glass sphere system) as shown in Fig. 59. In Fig. 60-61 the temperature distribution for Case 3 (decaying cosine function, Eq. (1.4)) are presented for $\gamma = 0.06$, $Re_H = 4161$ and $\gamma = 0.12$, $Re_H = 8228$ respectively for the R-113/glass sphere system. Similar underprediction of the temperatures on the hot side of the channel is observed from this plot.

Using the dispersion model of Kuo and Tien [121] as given by Eq. (1.12) with the exponential porosity function given by Case 1, the experimental conditions of Cai [116] was numerically simulated at $Re_H = 2407$ and $\gamma = 0.12$ for the air/glass sphere system. Comparison of the numerical solution and experimental data of the temperature distribution is presented in Fig. 62. The temperature profile with Kuo and Tien's dispersion model [121] seems to predict the bed temperatures quite well. In

Fig. 63 Cai's experimental data [116] are compared with computed temperature profiles based on Koch and Brady's [122] dispersion model, Eq. (1.13) (also under Case 1 conditions) for the air/glass sphere system at Re_H = 2407 and $\gamma = 0.12$. The temperature profiles for this model for the channel and the tube geometries are of similar nature, i.e. the observed temperatures are below the corresponding predicted values. From the predicted temperature profiles presented in Figs. 50-63, it is seen that none of the porosity functions or dispersion models that have been assumed in this study, is able to predict the temperature distribution of the experiments of Cai [116] well. The closest prediction is obtained with the dispersion model of Kuo and Tien [121] under Case 1 assumptions and for the present dispersion model with $C_d = 0.13$, $\omega = 4$ for the Case 2 conditions.

5.4.3 Thermal entrance length :

The thermal entrance length, L_{th}, (normalized with respect to the particle diameter) for the flow of R-113 in a packed tube and a packed channel was computed for different dimensionless particle diameters, and for different Reynolds numbers, Re_d (based on the particle diameter). In the numerical solution a thermally fully developed condition was assumed if the local Nusselt number at a consecutive axial location did not change by 0.01 percent. The results of the predicted thermal entrance length for $\gamma = 0.06$ and 0.12 are presented in Table 5 for R-113/glass sphere system for forced convection in a packed channel. From Tables 5 it can be observed that the thermal entrance length increases with the Reynolds number. This can also be concluded from Cai's experimental data for the temperature distribution presented in Fig. 52 ($Re_H = 2407$) and Fig. 56 ($Re_H = 16613$). It can be seen that when the Reynolds

number is increased the thermal boundary layer becomes thinner which would mean longer thermal entrance length. On the other hand from the same Table it can be observed that for the larger particles the thermal entrance length seems to be shorter. If the comparison is made for a particular Reynolds number which means that for the larger particle the velocity is less, then, on the basis of what has been conclude (decrease of L_{th} with Re_d) the trend of the thermal entrance length with an increase in γ can be explained. For $Re_d > 100$ the thermal entrance length seems to be almost independent of the Reynolds number.

For a packed tube the thermal entrance length was also calculated for R-113/glass sphere system and for $\gamma = 0.06$ and 0.12 . The predicted results of the thermal entrance length are presented in Table 5 and are similar in nature as for the channel configuration.

5.4.4 Effect of Pr and λ on heat flux in a packed tube and a packed channel :

A numerical investigation was conducted for forced convection in a packed tube to study the effect of Prandlt number, Pr, and the ratio of the fluid to solid thermal conductivity, λ. The computed results are presented in Fig. 64 for $\gamma = 0.06$, in which case the present dispersion model was used with Case 1 assumption. In Fig. 64 the predicted results of the Nusselt number are represented by the solid line (curve a) for the R-113/glass sphere system ; the dashed line (curve b) for the air/glass sphere system ; the chain-dashed line (curve c) for the air/chrome steel sphere system ; and the chain-dot line (curve d) for the R-113/chrome steel sphere system. It should be mentioned that the effect of the Prandlt number alone cannot be examined because it

also changes the value of the thermal conductivity ratio λ. The curves plotted in Fig. 64 show three distinct regions :

a) the conduction dominated region in which the heat flux is independent of the Reynolds number,

b) the transition region in which conduction and forced convection heat transfer are of comparable magnitude, and

c) the forced convection region in which the heat flux has an exponential relationship with the Reynolds number.

The Reynolds number that correspond to these regions seems to depend on the continuous phase in the porous media. The following conclusions can be made on the three regions mentioned above for air and R-113 :

	Air/chrome steel	R-113/chrome steel
Conduction region :	$Re_D < 100$	$Re_D < 10$
Transition region :	$100 < Re_D < 10^3$	$10 < Re_D < 2 \times 10^3$
Forced convection region :	$Re_D > 10^3$	$Re_D > 2 \times 10^3$

It is evident from Fig. 64 that the Prandlt number has a pronounced effect on the heat flux in a packed-sphere bed beyond a critical Reynolds number which is in the transition region. The value of the critical Reynolds number seems to depend on the type of solid and fluid in the system. When the porous matrix is composed of glass-spheres and the fluid medium is either air or R-113 the critical Reynolds number is about 20. On the other hand for the air/chrome steel and R-113/chrome steel sphere system this is around 30. The increase in the heat flux for the air/glass and R-113/glass system is about five times for $Re_D > 10^3$, i.e. in the forced convection region. This is

also true for the air/chrome steel and R-113/chrome steel sphere system for $Re_D > 2 \times 10^3$. The effect of Prandlt number on the heat flux becomes small as the conduction dominated region is approached for a given type of the solid medium.

From Fig. 64 the effect of the thermal conductivity ratio of the fluid and solid medium on the dimensionless heat flux in a packed tube can also be studied. The effect of the thermal property of the solid medium is seen to be small at large values of Reynolds number. But in the conduction region the thermal conductivity ratio has a pronounced effect on the heat transfer. For the air/glass system, $\lambda = 0.03$ (curve b), and the air/chrome steel sphere system, $\lambda = 0.0006$ (curve c), the heat flux increases in the latter by a factor of two in the conduction region. Similar conclusions can be made for the R-113/glass sphere system, $\lambda = 0.071$ (curve a), and the R-113/chrome steel sphere system, $\lambda = 0.0017$ (curve d). From Fig. 64 it can also be concluded that a fluid with a greater Prandlt number enhances heat transfer if the flow is in the convection dominated region. On the other hand if the heat transfer is conduction dominated (i.e. at slower flows) more heat can be removed by using a solid material with a higher thermal conductivity.

A similar numerical study on the effect of Prandlt number and the thermal conductivity ratio of the fluid and the solid for forced convection in a packed channel was also carried out. The value of $\gamma = 0.06$ was used in the computation. The same combinations of the fluid and solid were used as in the case of the packed tube. The numerical results for the Nusselt number as a function of the Reynolds number is presented in Fig. 65. It is found that the same conclusions as in the case of a packed tube are also valid for a packed channel.

5.5 Mixed Convection in a Packed Tube and a Packed Channel :

Since no experimental data could be obtained in the open literature for mixed convection in a packed tube or a channel for the constant wall temperature boundary condition, a qualitative analysis is presented below for these flow conditions. The effect of buoyancy force on forced flow was obtained by decreasing the Reynolds number for a fixed value of the Grashofs number, Gr_D. The Nusselt numbers for this were compared with the forced convection situation to determine if the buoyancy term had any effect.

5.5.1 Mixed convection in a packed tube :

The numerical results of the local heat flux Nu_{DX} as a function of the axial distance is presented in Fig. 66 for $\gamma = 0.06$ (air/glass sphere system) at $Gr_D / Re_D = 5 \times 10^5, 9 \times 10^5, 2 \times 10^6$. From Fig. 66 it can be observed that the effect of the buoyancy force is to decrease the thermal entrance length. Similar results can also be observed in classical heat transfer problems [117]. In Fig. 67 the average Nusselt number is plotted as a function of Gr_D / Re_D for $\gamma = 0.06$ and 0.12 for the air/glass sphere system. The horizontal dashed lines in this figure represents the predicted asymptotes for forced convection. From Fig. 67 it can be seen that the effect of buoyancy force on forced convection become important when $Gr_D / Re_D > 9 \times 10^5$ for $\gamma = 0.06$ and for values of $Gr_D / Re_D > 4 \times 10^4$ for $\gamma = 0.12$.

5.5.2 Mixed convection in a packed channel :

A similar numerical analysis was performed for mixed convection in a packed channel for the air/glass sphere system for $\gamma = 0.06$ and 0.12. The numerical

results of the local Nusselt number, Nu_H, as a function of distance from the inlet of the channel for $\gamma = 0.06$ is presented in Fig. 68 for $Gr_H / Re_H = 9 \times 10^4, 2 \times 10^5, 5 \times 10^5$. The thermal entrance length is also seen to decrease due to the effect of buoyancy force on the induced flow in a channel. In Fig. 69 the average Nusselt number is plotted as a function of Gr_H / Re_H for $\gamma = 0.06$ and 0.12 for the air/glass sphere system. The horizontal dashed lines in this figure represents the predicted asymptotes for forced convection. From Fig. 69 it can be observed that for $\gamma = 0.06$ and $Gr_H / Re_H > 9 \times 10^4$ the effect of the buoyancy forces become important. From the same figure for $\gamma = 0.12$ it can be seen that buoyancy forces are important to consider for values of $Gr_H / Re_H > 4 \times 10^3$.

CHAPTER 6

CONCLUSIONS AND REMARKS

The present study has been motivated by the need for a better understanding of the fluid flow and heat transfer characteristics for an induced flow in a fluid-saturated packed bed that is contained in a cylindrical tube and in a channel. The outstanding features of this study are :

a) the use of the full momentum and energy equation, i.e. without the boundary layer approximation in the two-dimensional flow problem

b) the inclusion of the effect of the dimensionless particle diameter in the dispersion conductivity model of Hsu and Cheng [45,98], and

c) the use of a porosity function that accounts for both streamwise and cross-stream porosity variations.

6.1 Conclusions :

The mathematical formulation of convective heat transfer in porous media with variable porosity and thermal dispersion taken into consideration contains seven empirical constants. Three of these constants N, C_1 and φ_a appear in the exponential porosity function, Eq. (1.5a), the two Ergun constants A and B in Eq. (2.3) and two constants C_d and ω in the proposed dispersion conductivity model, Eq. (1.11). The asymptotic value of porosity, φ_a, and the Ergun constants A and B have been found to have a significant effect on the pressure drop in a packed bed

system. With all other empirical constants held fixed a 10% increase in the value of φ_a (from 0.36 to 0.4) results in the pressure drop to be underpredicted by 40%. The effect of the Ergun constant A for $Re_D < 10^3$ on the pressure drop has been found to be almost proportional, i.e. a 1% decrease in the value of A, results in the pressure drop to be underpredicted by 1%. The effect of the Ergun constant B for $Re_D > 10^4$ follows the same trend. The values of the Ergun constants A ($150 \leq A \leq 226$) and B ($1.75 \leq B \leq 1.92$) have negligible effect on the heat transfer characteristics.

The values of the seven empirical constants which yield the best match for the numerical and observed fluid flow and heat transfer results have been found to be as follows : $N = 6$, $C_1 = 1.4$, $\varphi_a = 0.36$, $A = 215$, $B = 1.92$, $C_d = 0.15$ and $\omega = 3$. The first five empirical constants were determined by a comparison of the porosity, velocity and pressure drop data in a packed tube, while the latter two empirical constants were determined by a comparison of the available heat flux data for forced convection in a packed tube and a channel.

The predicted hydrodynamic entrance length has been found to be about 10 to 20 particle diameters long for $0.024 \leq \gamma \leq 0.097$ and $1 \leq Re_d \leq 10^3$. Based on the dimensional length, the hydrodynamic entrance length was found to be shorter for the smaller particles. For all practical purposes the entrance length can be considered to be equal to the size of the tube diameter, D (or the plate separation distance, H).

The predicted heat flux results for flow in a packed tube were found to be within 10% of the observed values for $0.06 \leq \gamma \leq 0.12$ (air/glass sphere system) and $10^3 \leq Re_D \leq 10^4$. For the air/chrome steel sphere system the agreement was within 19% for $\gamma = 0.12$ and 0.14 and $10^3 \leq Re_D \leq 10^4$. The large difference in the observed and predicted heat flux results for the air/chrome steel spheres has been attributed to the

small value of the fluid to solid thermal conductivity ratio, λ, in which case there is a temperature gradient between the fluid and the solid, thereby invalidating the thermal equilibrium assumption used in the derivation of the energy equation. For the packed channel geometry the numerical values of the heat flux has been found to be within 20% of the observed values ($0.06 \leq \gamma \leq 0.125$, $10^3 \leq Re_D \leq 10^4$), the discrepancy in this case being attributed to improper experimentation and variable property effects of the fluid next to the heated surface which is not taken into account in the numerical solution.

The effects of the Prandlt number, Pr, and the fluid to solid thermal conductivity ratio, λ, on the heat flux was observed to depend on the type of flow. Accordingly, the following regions have been identified in this study for air and Freon (referred to as R-113 in this study) based on the heat transfer mechanism :

	Air	R-113
Conduction region	$Re_D < 100$	$Re_D < 10$
Transition region	$100 \leq Re_D \leq 10^3$	$10 \leq Re_D \leq 2 \times 10^3$
Forced convection region	$Re_D > 10^3$	$Re_D > 2 \times 10^3$

The effect of the Prandlt number on the heat flux becomes significant only in the forced convection region. The effect of using a fluid with a Prandlt number that is 10 times larger (for a given type of solid particle) has been seen to increase the heat flux by a factor of five in the forced convection region. The effect of using chrome steel spheres instead of glass spheres (thermal conductivity of chrome steel being about 40 times greater) was found to increase the heat flux by a factor of two in the conduction region.

For the packed cylindrical tube the effect of increasing the length of the heated tube, for the same particle size was observed to decrease the predicted Nusselt number. On the other hand, in the case of the air/glass sphere system, for the same length of the heated tube the effect of using larger size particles was seen to have no effect on the Nusselt. The chrome steel spheres have been found to enhance the heat transfer more than the glass spheres for forced convection in a packed tube.

In the case of forced convection in a packed channel, increasing the size of the particles was observed to decrease the predicted Nusselt number for the same length of the channel. This characteristic is also observed in the experimental results. The numerical solution for the heat flux in the case of the chrome steel spheres showed a higher heat flux than the steel spheres (for the same channel length and almost the same particle diameter) whereas the experimental data show no such effect. A higher heat transfer is expected when the solid matrix is comprised of chrome steel spheres as compared to the glass spheres owing to the large thermal conductivity value of the former.

The numerical solution has been seen to underpredict the heat flux results for $\gamma > 0.15$ (air/glass system). The discrepancy has been attributed to the fact that the volume averaging method used in the derivation of the governing equations may not be valid for such large size particles.

Finally, for the mixed convection problem, the buoyancy force was found to play an important role in the heat transfer process (for $\gamma = 0.06$) if $Gr_D/Re_D > 9 \times 10^5$ for the packed tube and $Gr_H/Re_H > 9 \times 10^4$ for the packed channel configuration.

6.2 Recommendations for Future Research :

The following topics are suggested to further the research in mixed and forced convection in a packed bed :

a) experiments are needed to reconfirm heat flux data already obtained for forced convection in a packed channel

b) experiments are needed to obtain heat flux data for $Re_H < 10^3$ and $Re_H > 2 \times 10^4$ for convective flow in a packed channel

c) experiments are needed to obtain heat flux data for $Re_D < 10^3$ and $Re_D > 2 \times 10^4$ for convective flow in a packed tube

d) experiments are needed to obtain pressure drop data for forced convection in a packed channel

e) experiments are needed to obtain heat flux data for mixed convection in a packed channel and a packed tube for uniform wall temperature and uniform heat flux boundary conditions

f) experiments are needed to measure velocity distribution in a packed channel and in a packed cylindrical tube

g) numerical solutions are needed to determine the 3-D effects in mixed and forced convective flow in a packed tube and a channel.

Table 1

Computed hydrodynamic entrance length, L_{hy}, for a packed tube

$L_{hy} = L / d_p$

a) $\gamma = 0.024$

Re_d	Re_D	L_{hy}	L/D
1.0	41.7	21.81	0.52
4.0	166.7	20.76	0.49
10.0	416.7	19.74	0.47
15.0	625.0	18.72	0.44
20.0	833.3	17.73	0.43
35.0	1458.3	16.75	0.40
60.0	2500.0	15.78	0.38
125.0	5208.3	14.83	0.36
250.0	10416.7	13.89	0.33
450.0	18750.0	13.89	0.33
750.0	31250.0	13.89	0.33
1000.0	41666.7	13.89	0.33

b) $\gamma = 0.035$

Re_d	Re_D	L_{hy}	L/D
1.0	28.6	16.96	0.59
4.0	114.3	16.22	0.57
10.0	285.7	15.49	0.54
15.0	428.6	14.77	0.52
20.0	571.4	14.06	0.49
35.0	1000.0	13.02	0.46
60.0	1714.3	12.68	0.44
125.0	3571.4	11.67	0.41
250.0	7142.9	11.34	0.39
450.0	12857.1	10.69	0.37
750.0	21428.6	10.69	0.37
1000.0	28571.4	10.69	0.37

Table 1 (Continued)
Computed hydrodynamic entrance length, L_{hy}, for a packed tube

c) $\gamma = 0.045$

Re_d	Re_D	L_{hy}	L/D
1.0	22.2	14.09	0.63
4.0	88.9	13.51	0.61
10.0	222.2	12.93	0.58
15.0	333.3	12.37	0.56
20.0	444.4	11.53	0.52
35.0	777.8	11.26	0.51
60.0	1333.3	10.45	0.47
125.0	2777.8	9.92	0.45
250.0	5555.6	9.15	0.41
450.0	10000.0	9.15	0.41
750.0	16666.7	9.15	0.41
1000.0	22222.2	9.15	0.41

d) $\gamma = 0.071$

Re_d	Re_D	L_{hy}	L/D
1.0	14.1	11.92	0.85
4.0	56.3	11.92	0.85
10.0	140.8	10.75	0.76
15.0	211.3	10.17	0.72
45.0	633.8	9.59	0.68
150.0	2112.7	9.03	0.64
250.0	3521.1	8.46	0.60
450.0	6338.0	8.46	0.60
750.0	10563.4	8.46	0.60
1000.0	14084.5	8.46	0.60

Table 1 (Continued)
Computed hydrodynamic entrance length, L_{hy}, for a packed tube

e) $\gamma = 0.097$

Re_d	Re_D	L_{hy}	L/D
1.0	10.3	9.08	0.88
4.0	41.2	9.08	0.88
20.0	206.2	8.19	0.79
60.0	618.6	7.75	0.75
100.0	1030.9	7.31	0.71
250.0	2577.3	7.31	0.71
450.0	4639.2	7.31	0.71
750.0	7731.9	7.31	0.71
1000.0	10309.3	7.31	0.71

Table 2

Error statistic for Verschoor & Schuit's experimental data of the Nusselt number

Numerical simulation based on : Present dispersion model and Case 1 assumption.

γ	L (m)	System	Root Mean Square Error
0.06	0.3	Air/glass	0.0460
0.1	0.21	"	0.0662
0.101	0.26	"	0.0813
0.12	0.3	"	0.0773
0.12	0.21	Air/chrome steel	0.1588
0.14	0.3	"	0.1824
0.151	0.21	Air/glass	0.2453

Table 3

Error statistic for Leva's experimental data of the Nusselt number

Numerical simulation based on : Present dispersion model and Case 1 assumption.

L = 0.9 m

γ	System	Root Mean Square Error
0.086	Air/glass	0.152
0.11	"	0.109

Table 4

Error statistic for Cai's experimental data of the Nusselt number

Numerical simulation based on : Present dispersion model and Case 1 assumption.

L = 0.45 m

γ	System	Root Mean Square Error
0.06	R-113/glass	0.1764
0.12	R-113/glass	0.1938
0.125	R-113/chrome steel	0.0836

Table 5

Computed thermal entrance length, L_{th}, for a packed tube & a packed channel

$L_{th} = L / d_p$

A) Packed tube

a) $\gamma = 0.06$

Re_d	Re_D	L_{th}	L/D
1.6	25.8	27.34	1.64
3.2	53.2	41.52	2.49
6.3	104.3	85.70	5.14
8.7	145.0	99.57	5.97
11.0	183.3	105.40	6.32
18.1	301.7	115.10	6.91
23.9	398.3	120.80	7.25
29.7	495.0	126.50	7.59
46.8	780.0	133.10	7.99
58.2	970.0	136.10	8.17
80.9	1348.3	137.80	8.27
114.8	1913.3	140.40	8.42
171.4	2856.7	143.30	8.60
455.4	7590.0	144.70	8.68
683.4	11390.0	144.80	8.69
999.8	16663.3	144.80	8.69

Table 5 (Continued)
Computed thermal entrance length, L_{th}, for a packed tube & a packed channel

b) $\gamma = 0.12$

Re_d	Re_D	L_{th}	L/D
1.1	9.25	6.35	0.76
3.1	25.8	13.95	1.67
6.0	50.3	21.68	2.60
8.9	74.0	26.10	3.13
11.7	97.3	29.07	3.49
14.4	120.0	32.49	3.89
21.1	175.8	35.17	4.22
27.7	230.6	38.62	4.63
40.6	338.3	42.13	5.06
66.0	550.0	45.66	5.48
91.2	760.3	46.18	5.54
200.0	1666.7	46.20	5.54
400.0	3333.3	46.21	5.55
800.0	6666.6	46.22	5.55
1000.0	8333.3	46.23	5.55

Table 5 (Continued)
Computed thermal entrance length, L_{th}, for a packed tube & a packed channel

B) Packed channel -

a) $\gamma = 0.06$

Re_d	Re_D	L_{th}	L/D
1.2	19.2	25.2	1.51
3.4	56.8	51.6	3.09
6.4	106.7	73.5	4.41
10.0	167.3	90.4	5.42
16.6	276.7	103.0	6.18
21.9	365.0	109.5	6.57
27.4	456.7	117.5	7.05
54.1	901.7	121.7	7.30
100.0	1666.7	122.0	7.32
200.0	3333.3	122.2	7.33
400.0	6666.6	122.3	7.34
700.0	11666.6	122.5	7.35
1000.0	16666.6	122.8	7.37

b) $\gamma = 0.12$

Re_d	Re_D	L_{th}	L/D
1.3	10.6	8.83	1.06
3.2	26.6	18.78	2.25
6.3	52.3	30.01	3.60
12.3	102.3	38.20	4.58
18.2	151.5	41.50	4.98
29.7	247.7	48.56	5.83
46.9	390.7	50.50	6.06
80.9	674.4	55.58	6.67
103.6	863.3	58.30	6.99
200.0	1666.6	58.50	7.02
400.0	3333.3	58.70	7.04
800.0	6666.6	58.90	7.07
1000.0	8333.3	59.00	7.08

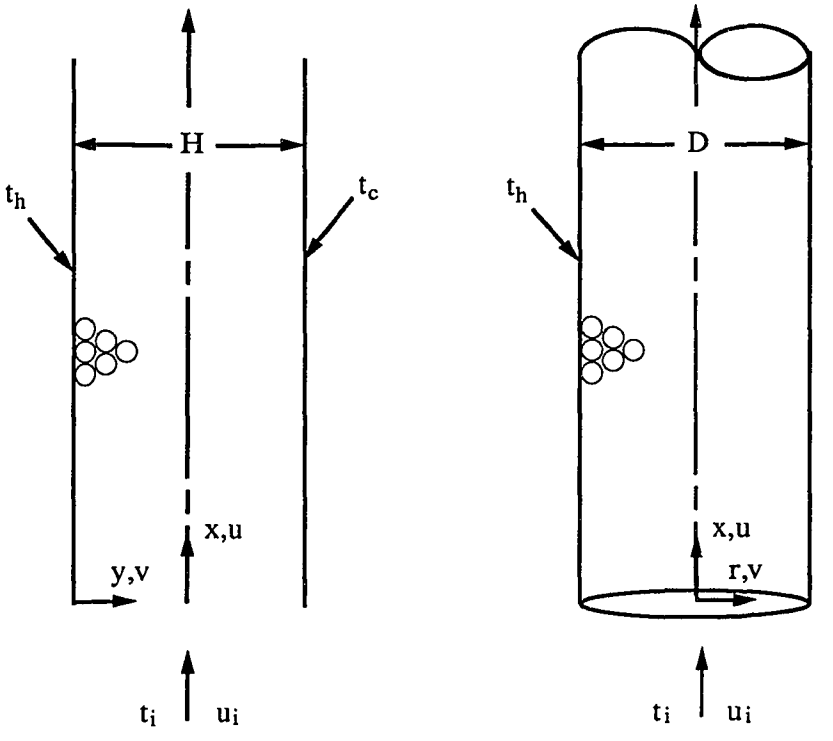

a) Packed channel

b) Packed tube

Figure 1. Coordinate system

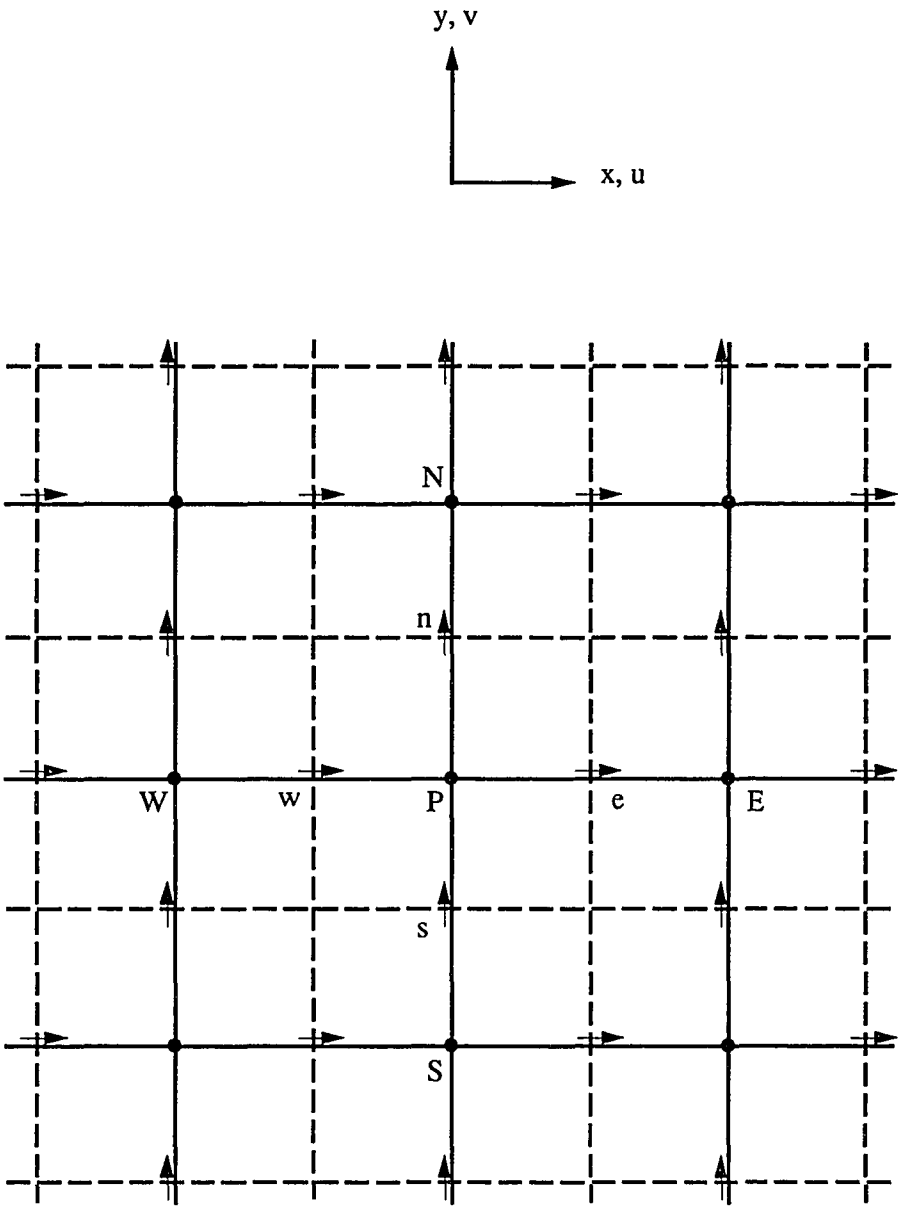

Figure 2. The staggered grid arrangement

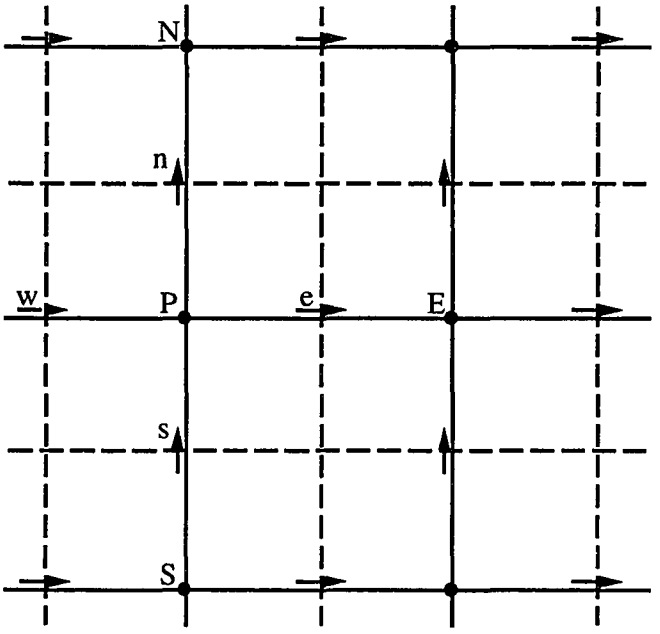

Control volume for U

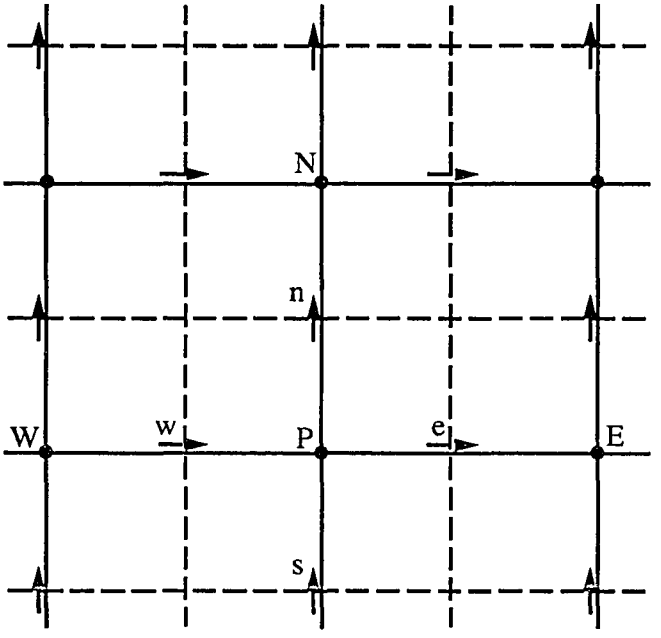

Control volume for V

Figure 3. U and V control volumes

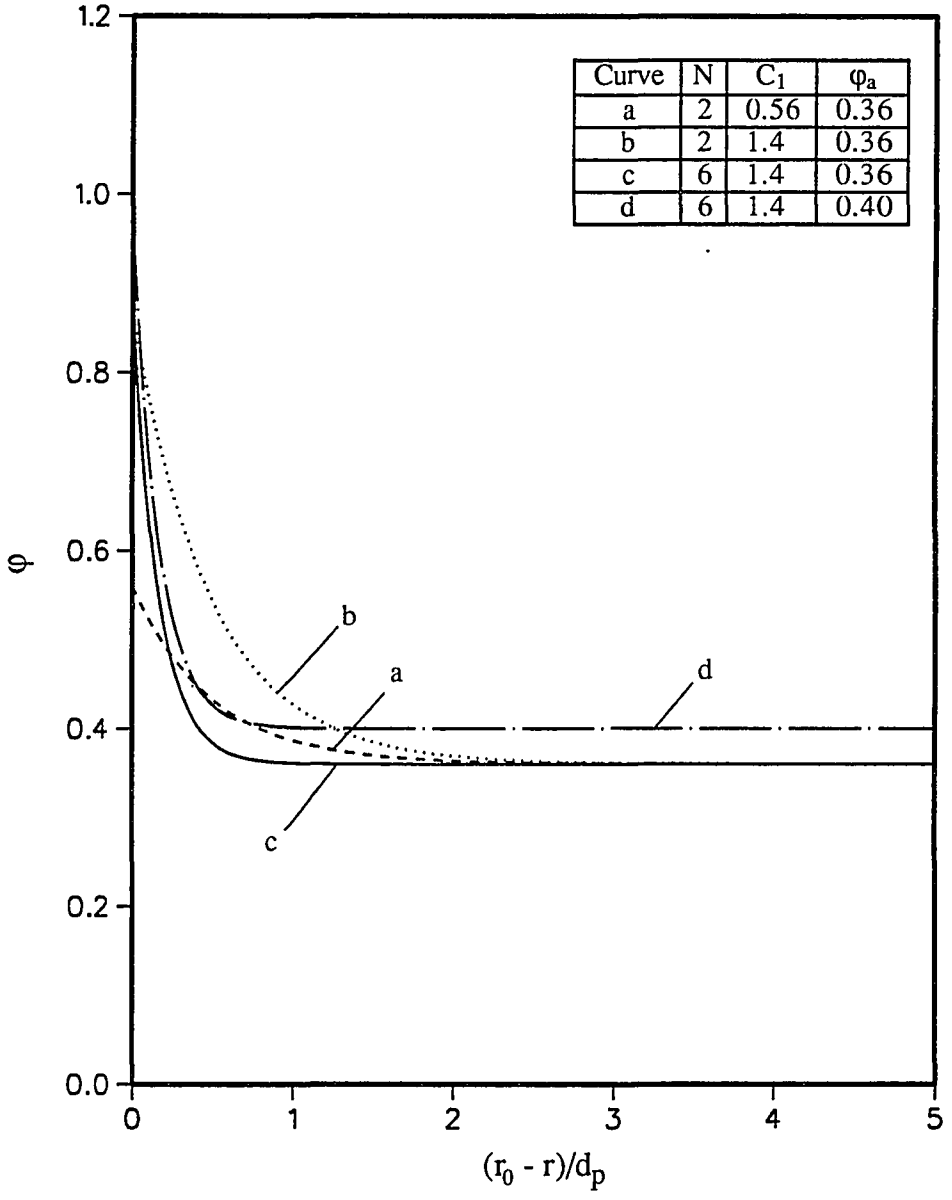

Figure 4. Effects of N, C_1 and φ_a on the exponential porosity distribution

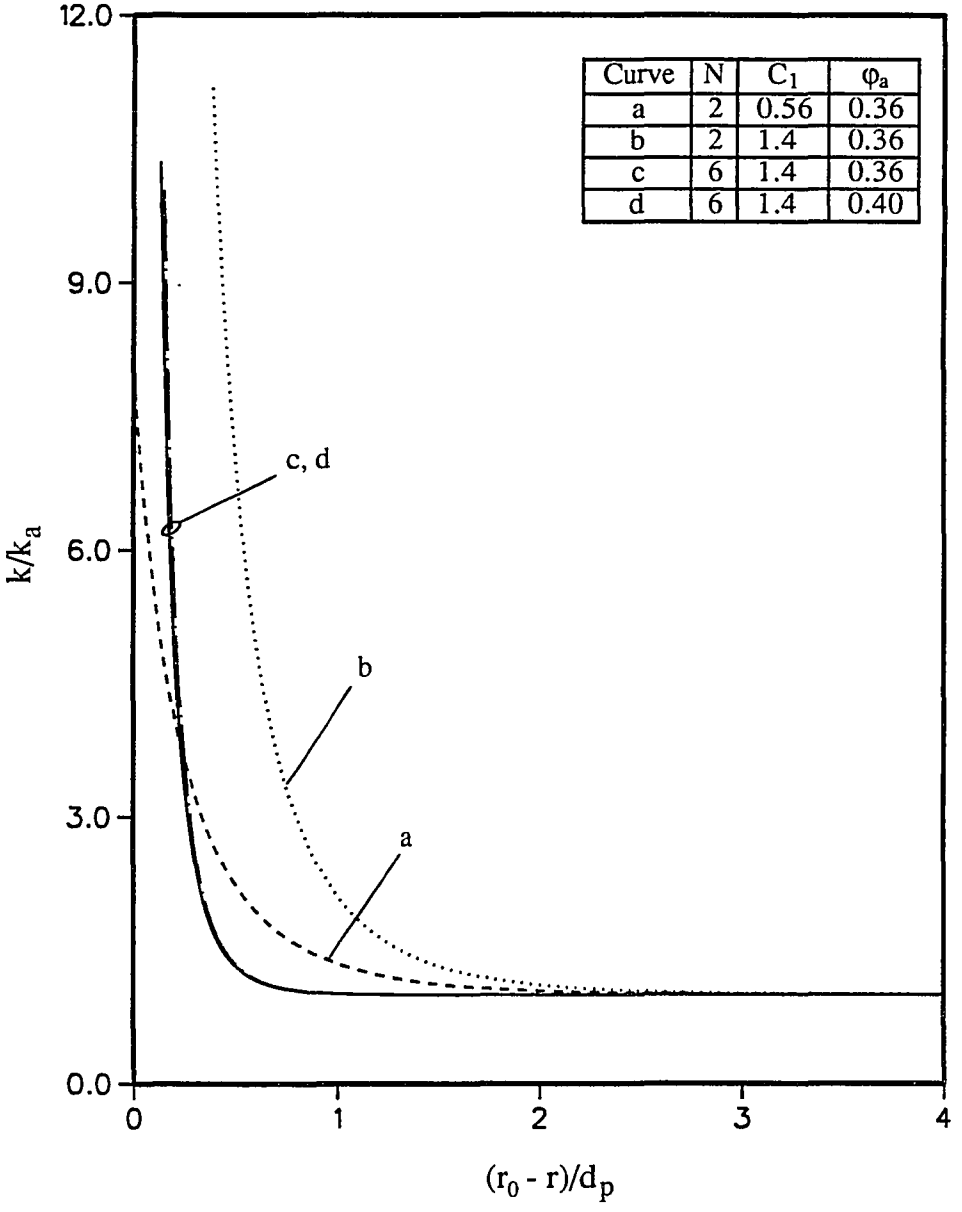

Figure 5. Effects of N, C_1 and φ_a on permeability

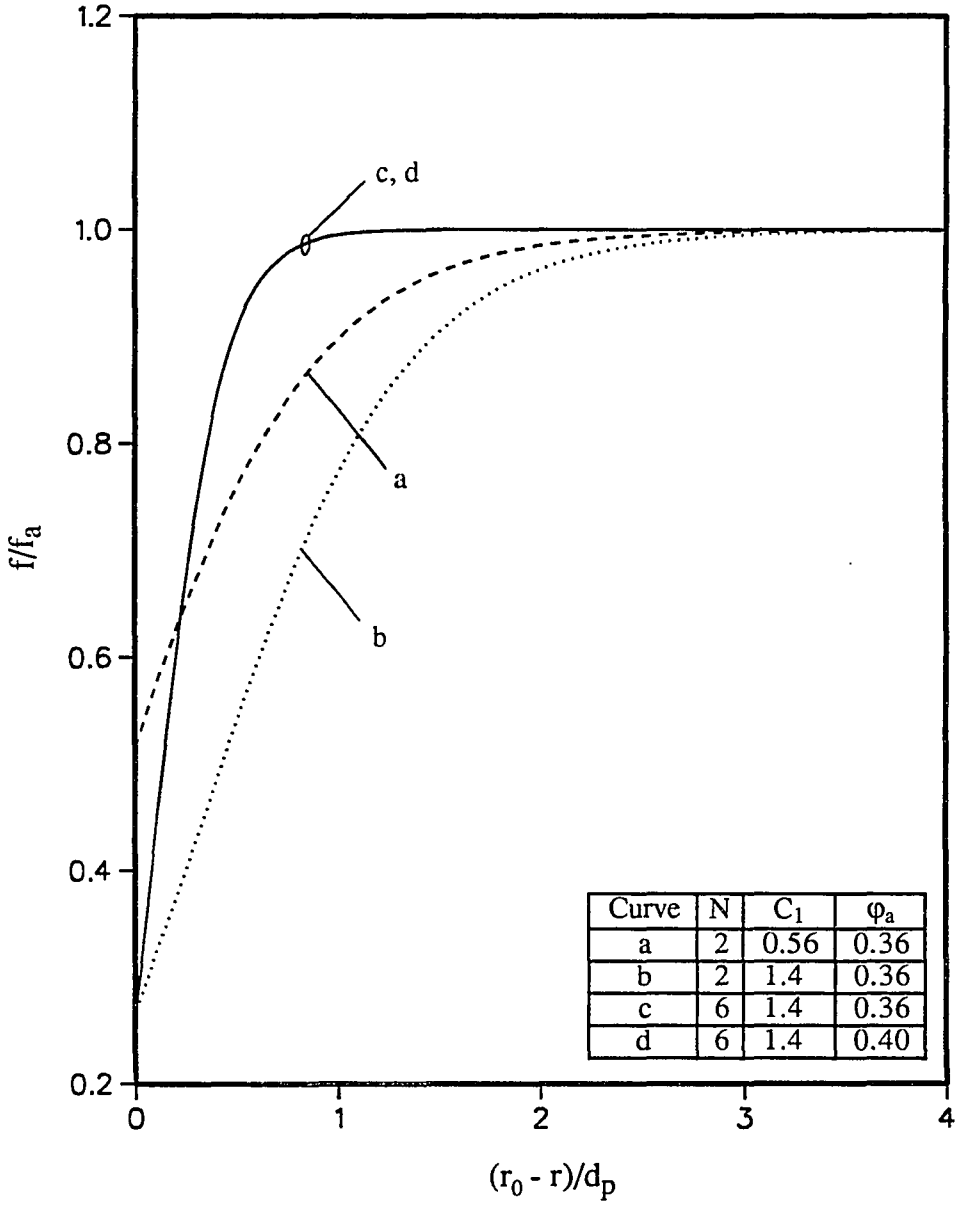

Figure 6. Effects of N, C_1 and φ_a on the inertia coefficient

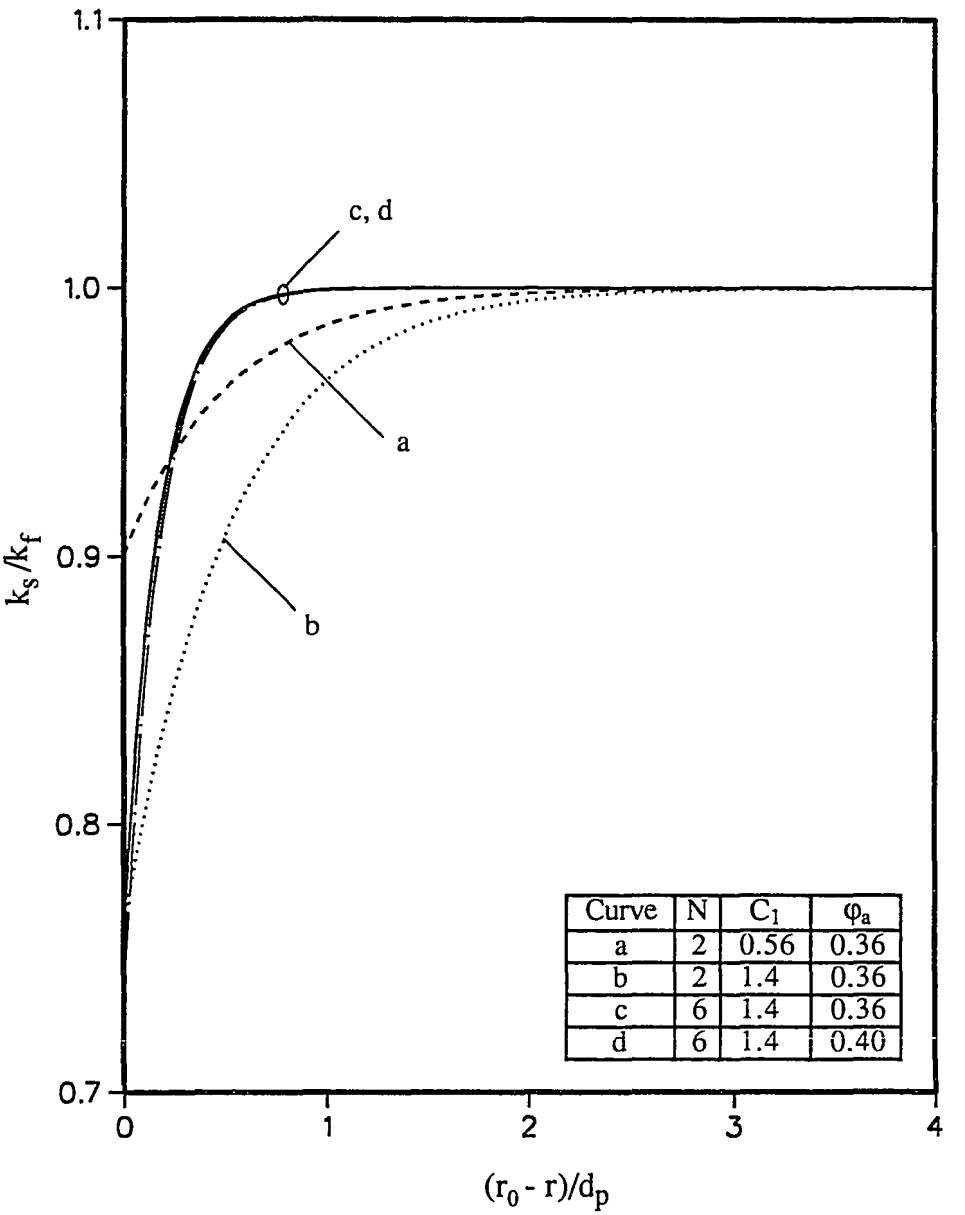

Curve	N	C_1	φ_a
a	2	0.56	0.36
b	2	1.4	0.36
c	6	1.4	0.36
d	6	1.4	0.40

Figure 7. Effects of N, C_1 and φ_a on the stagnant thermal conductivity

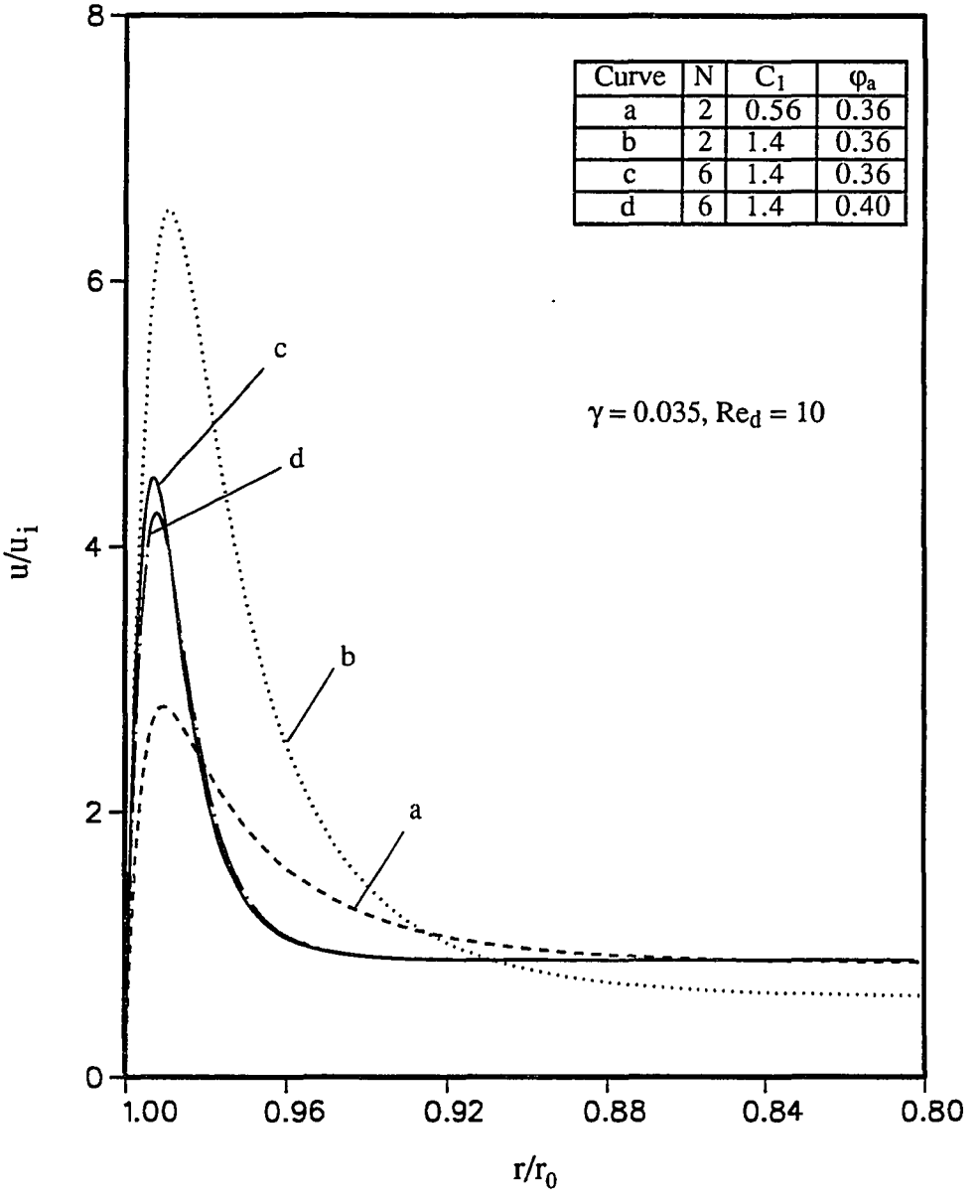

Figure 8. Effects of N, C_1 and φ_a on the axial velocity distribution for flow in a packed tube

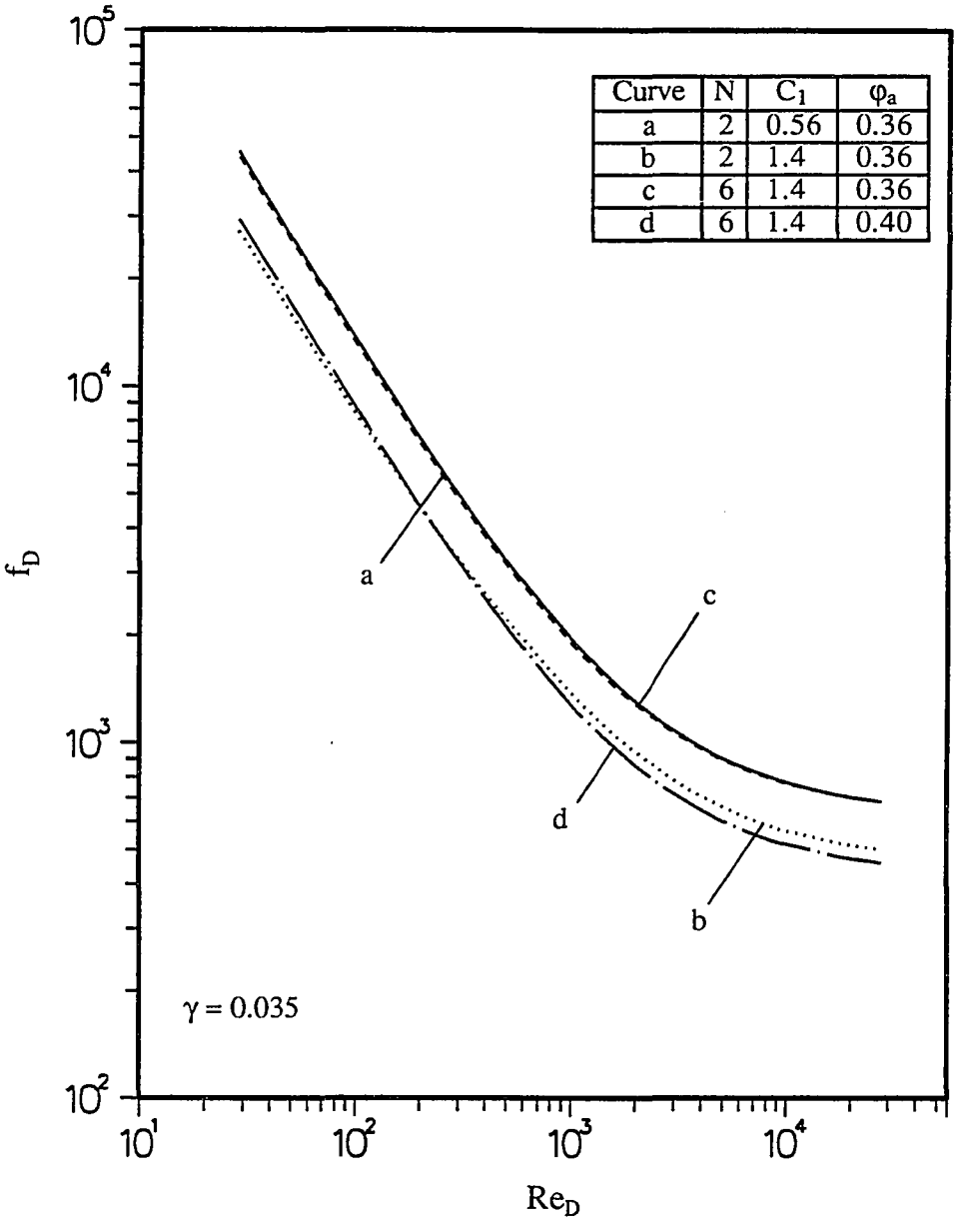

Figure 9. Effects of N, C_1 and φ_a on the dimensionless pressure drop for flow in a packed tube

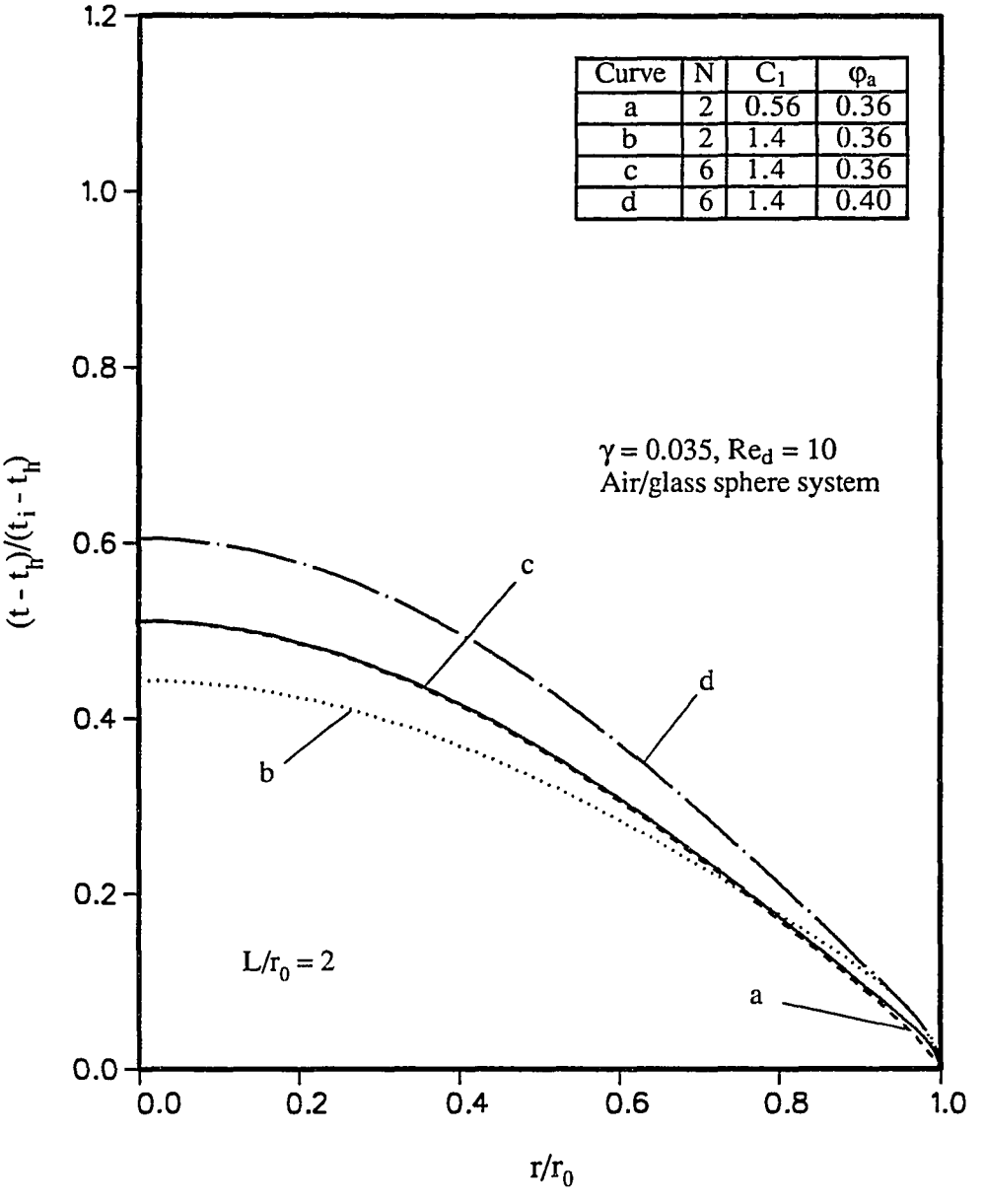

Figure 10. Effects of N, C_1 and φ_a on the dimensionless temperature distribution for forced convection in a packed tube

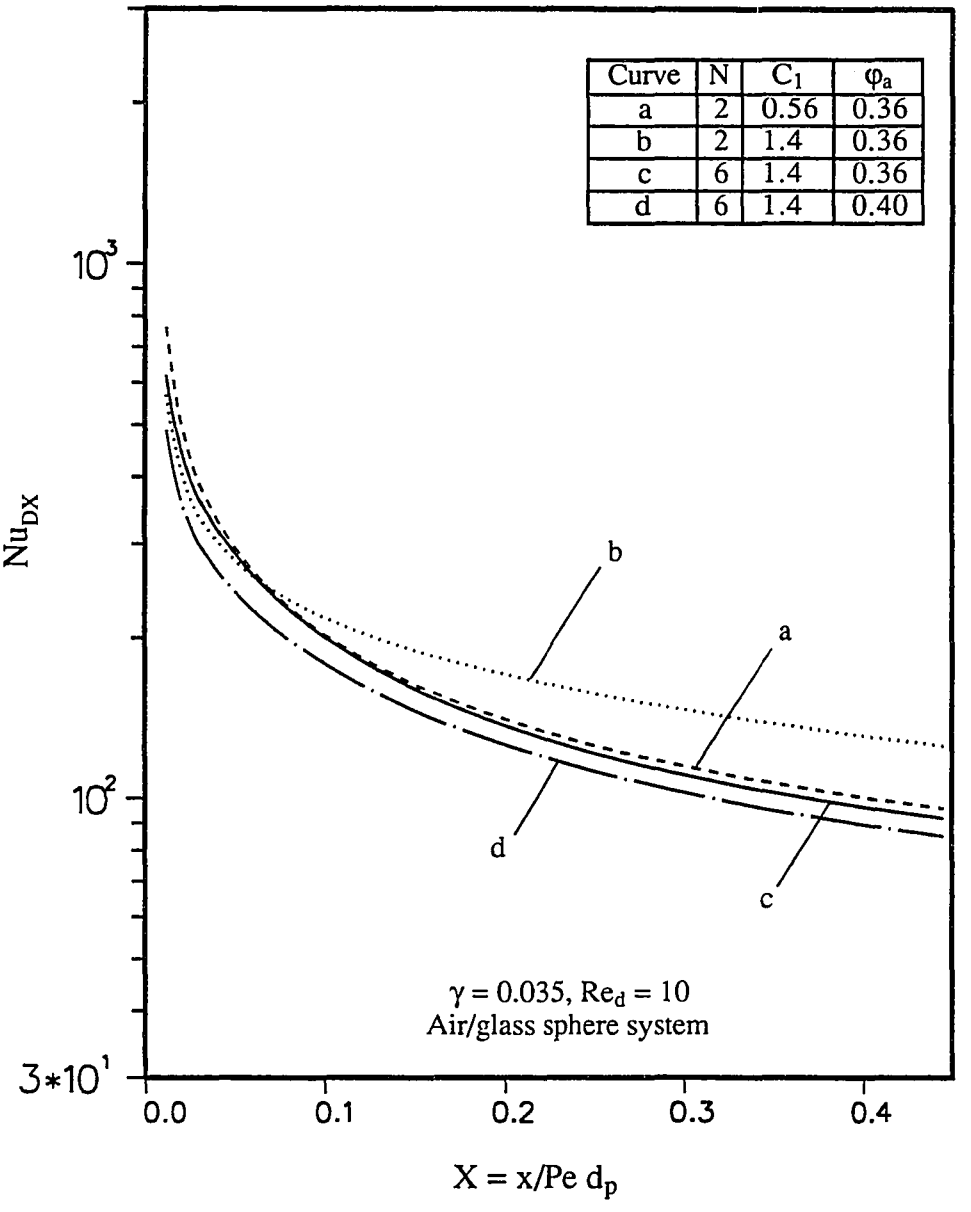

Figure 11. Effects of N, C_1 and φ_a on the local Nusselt number for forced convection in a packed tube

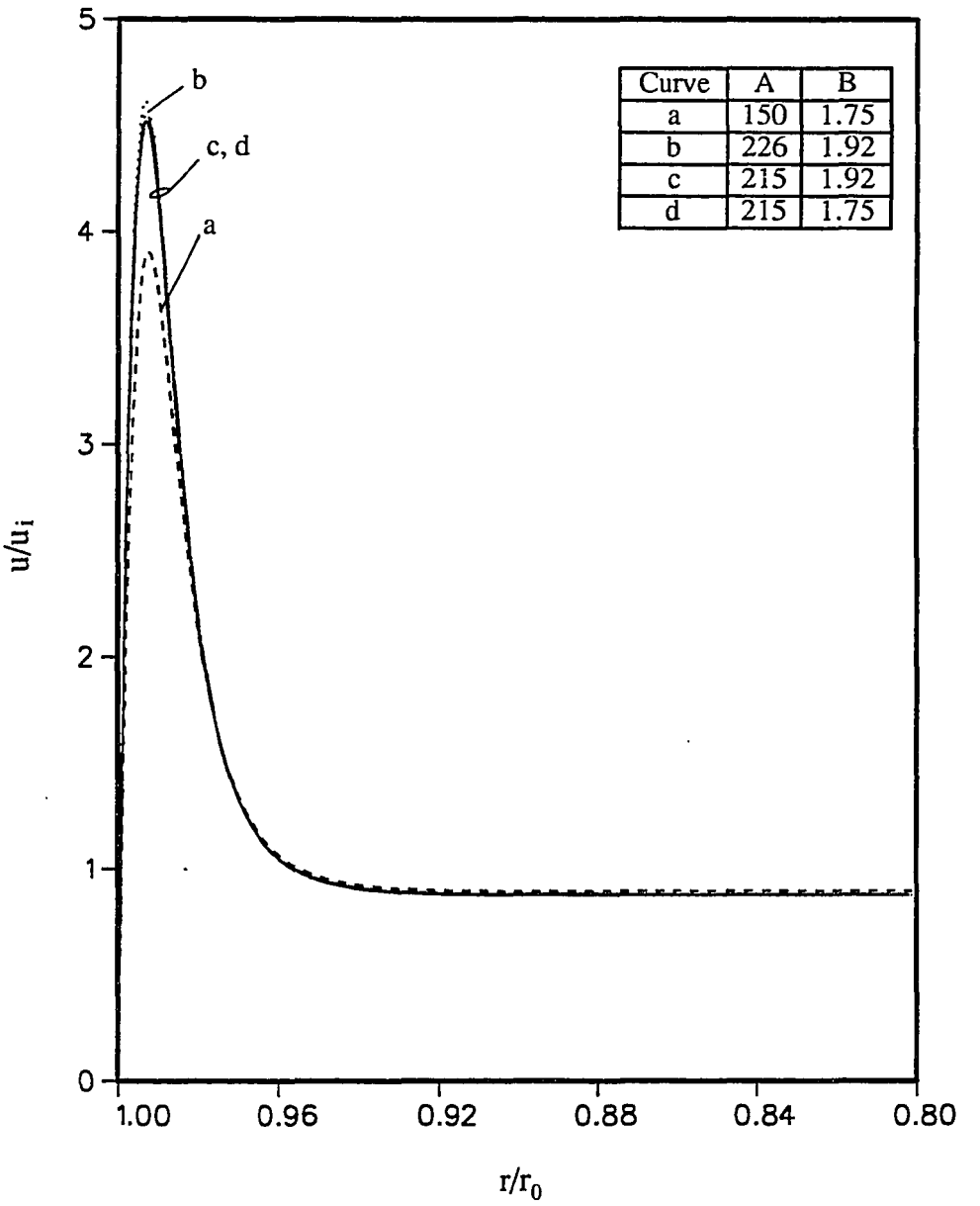

Figure 12. Effects of A and B on the axial velocity distribution for flow in a packed tube

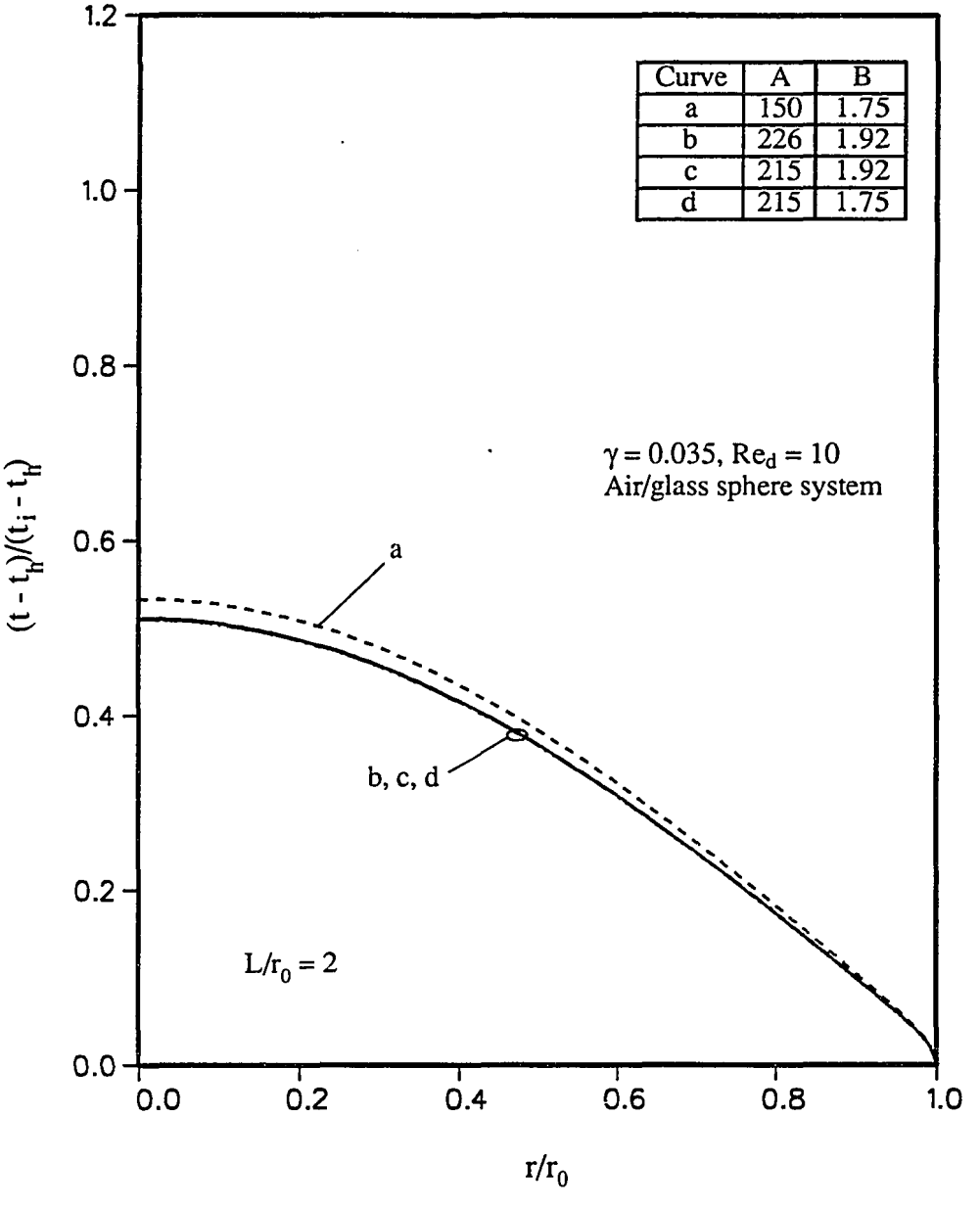

Figure 13. Effects of A and B on the dimensionless temperature distribution for forced convection in a packed tube

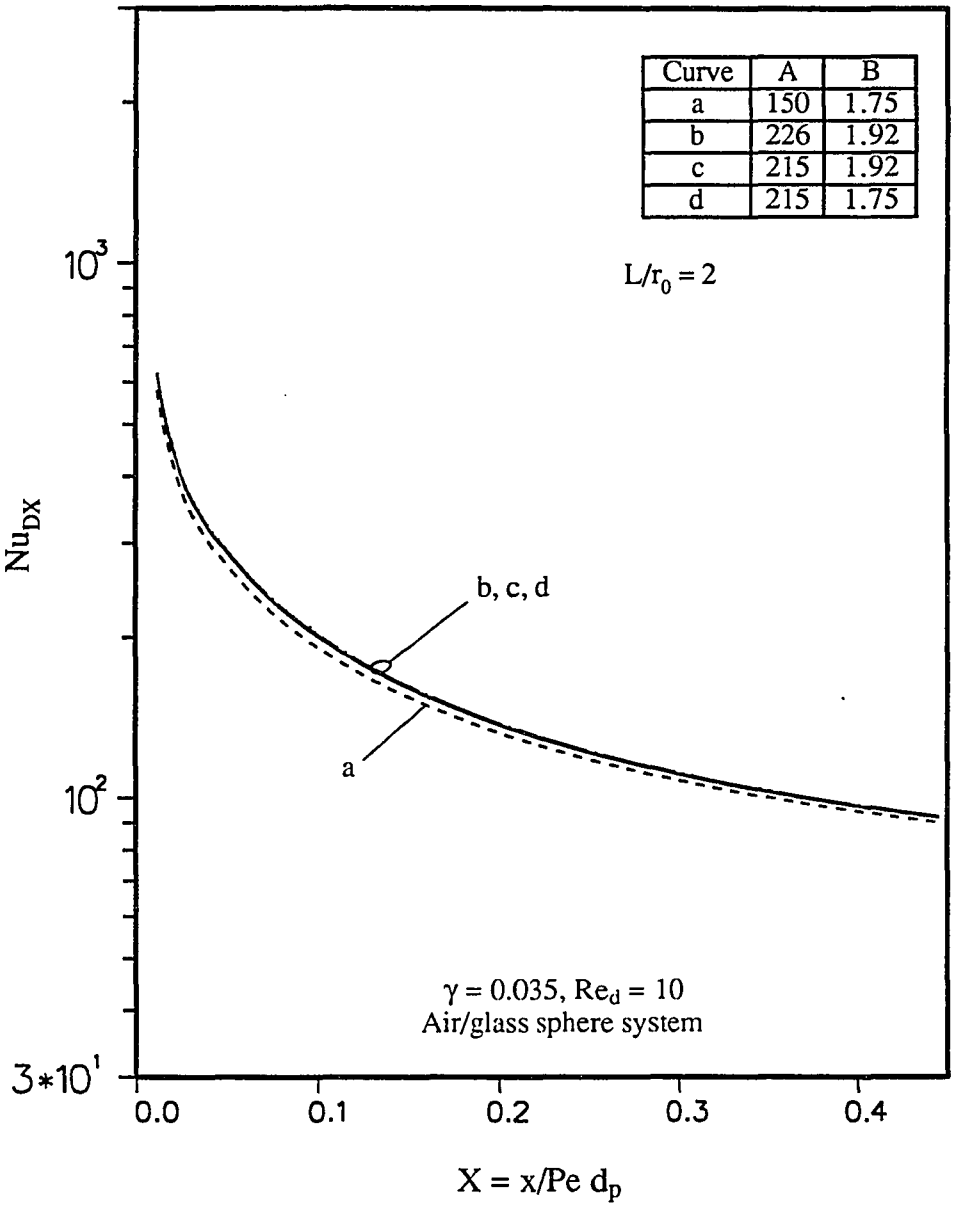

Figure 14. Effects of A and B on the local Nusselt number for forced convection in a packed tube

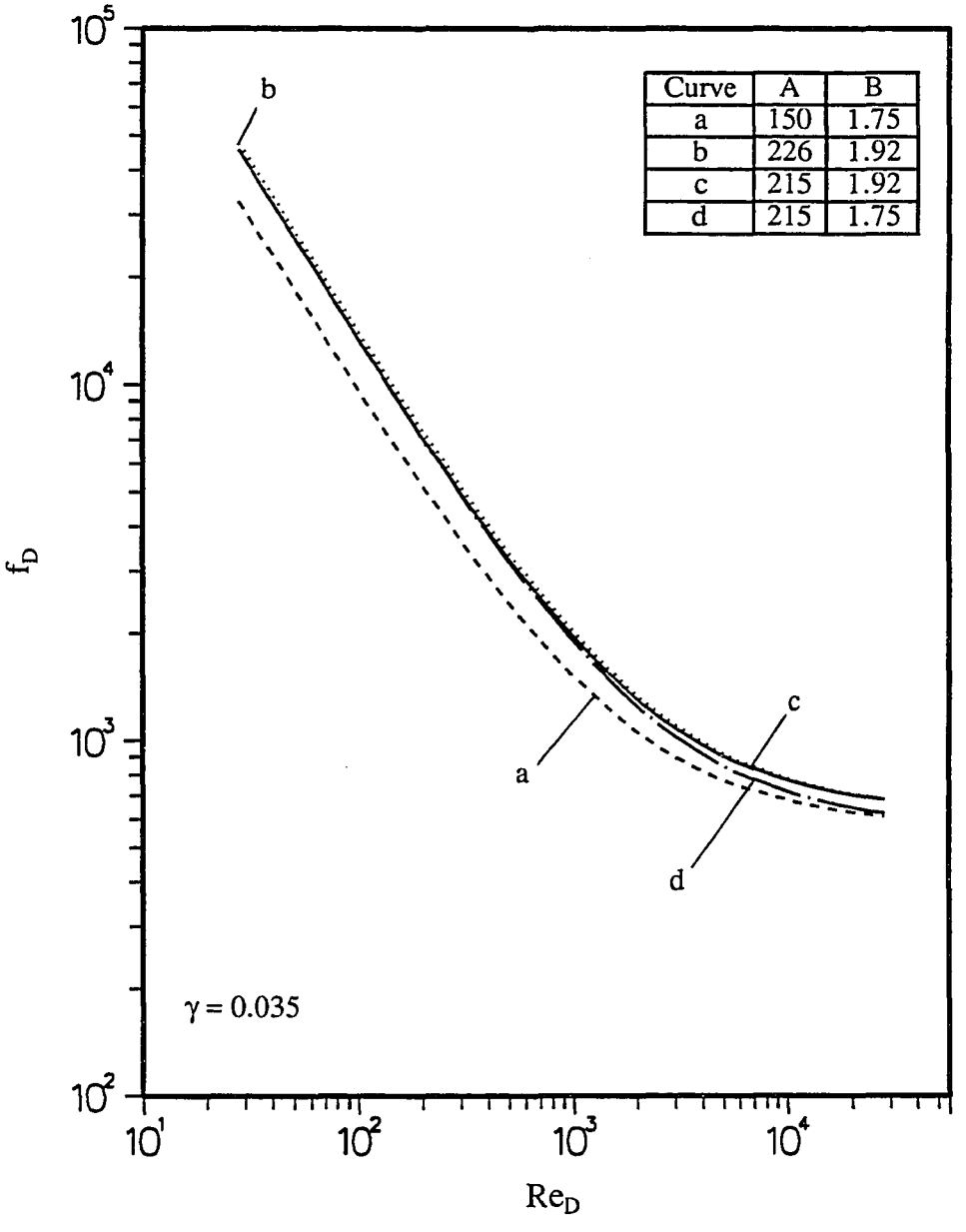

Figure 15. Effects of A and B on the dimensionless pressure drop for flow in a packed tube

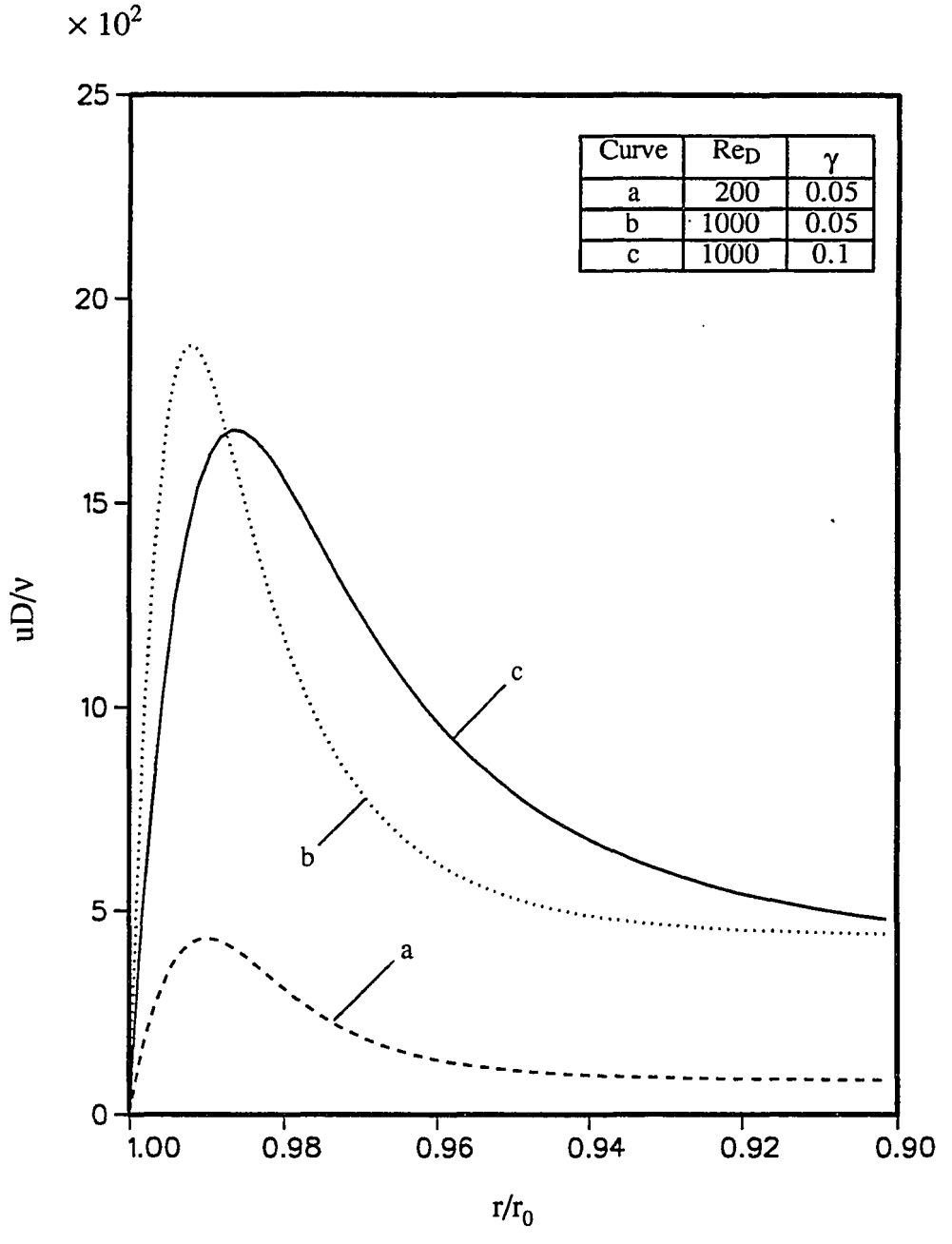

Figure 16. Effects of γ and Re_D on the axial velocity distribution for flow in a packed tube

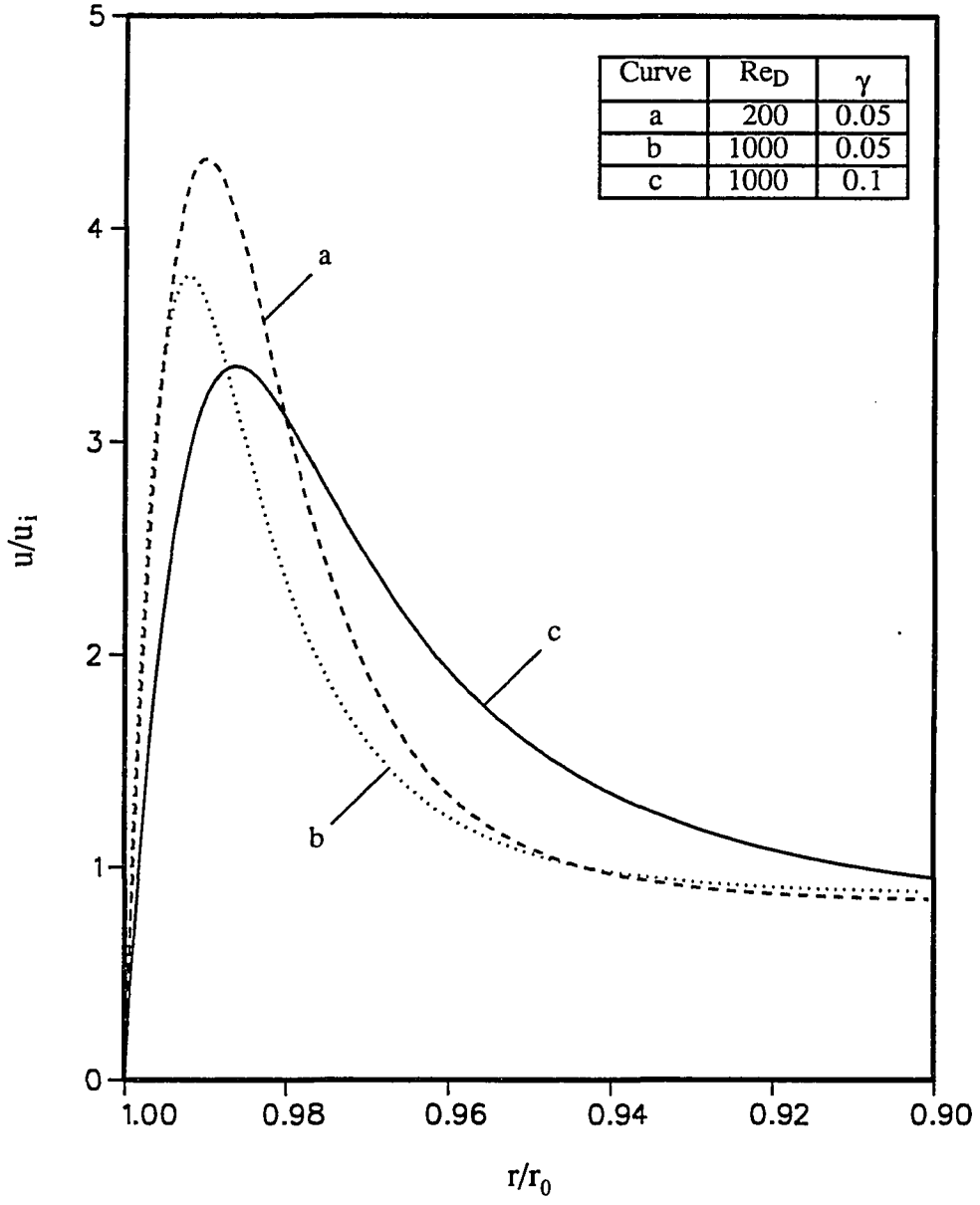

Figure 17. Effects of γ and Re_D on the axial velocity distribution for flow in a packed tube

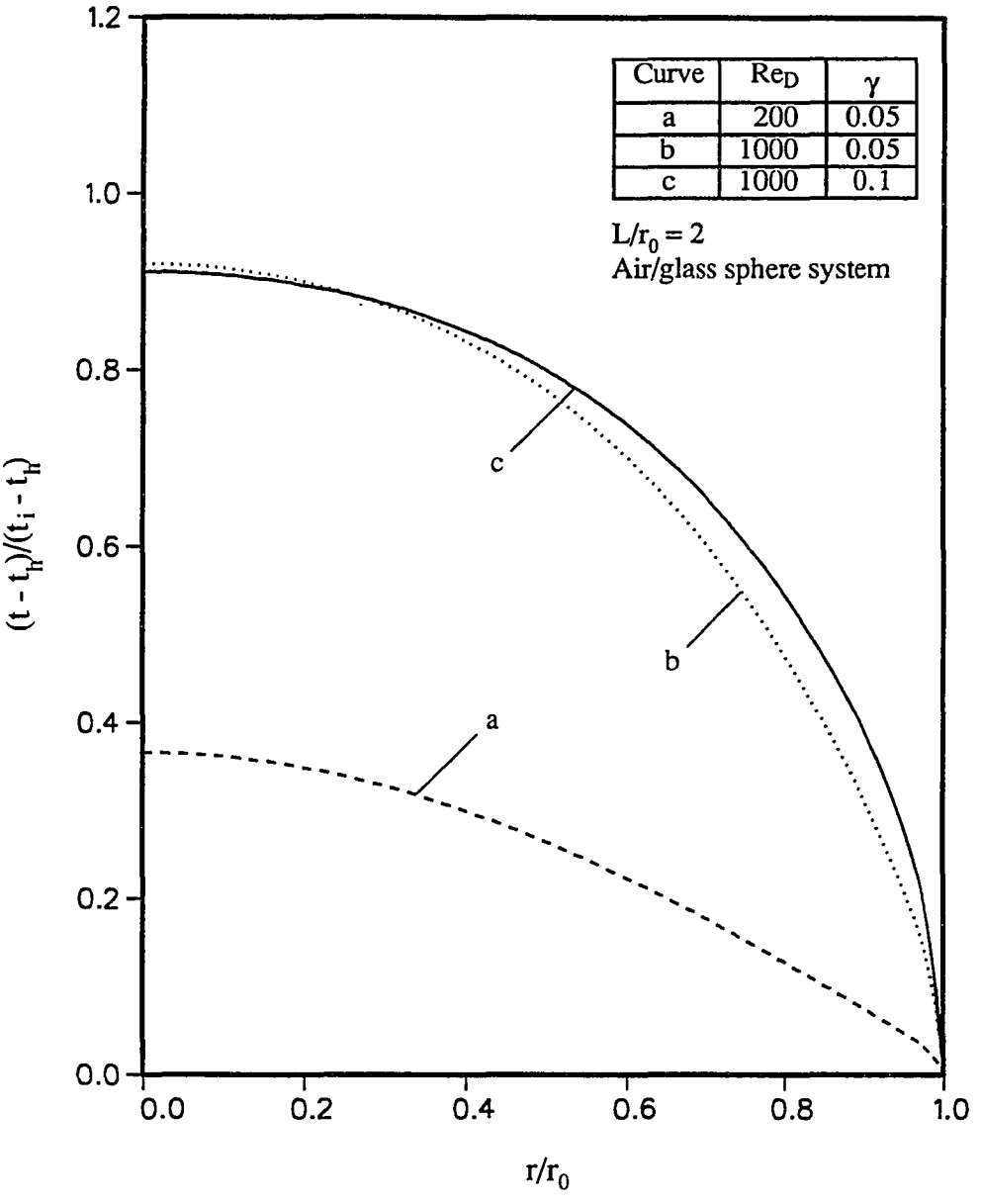

Figure 18. Effects of γ and Re_D on the dimensionless temperature distribution for forced convection in a packed tube

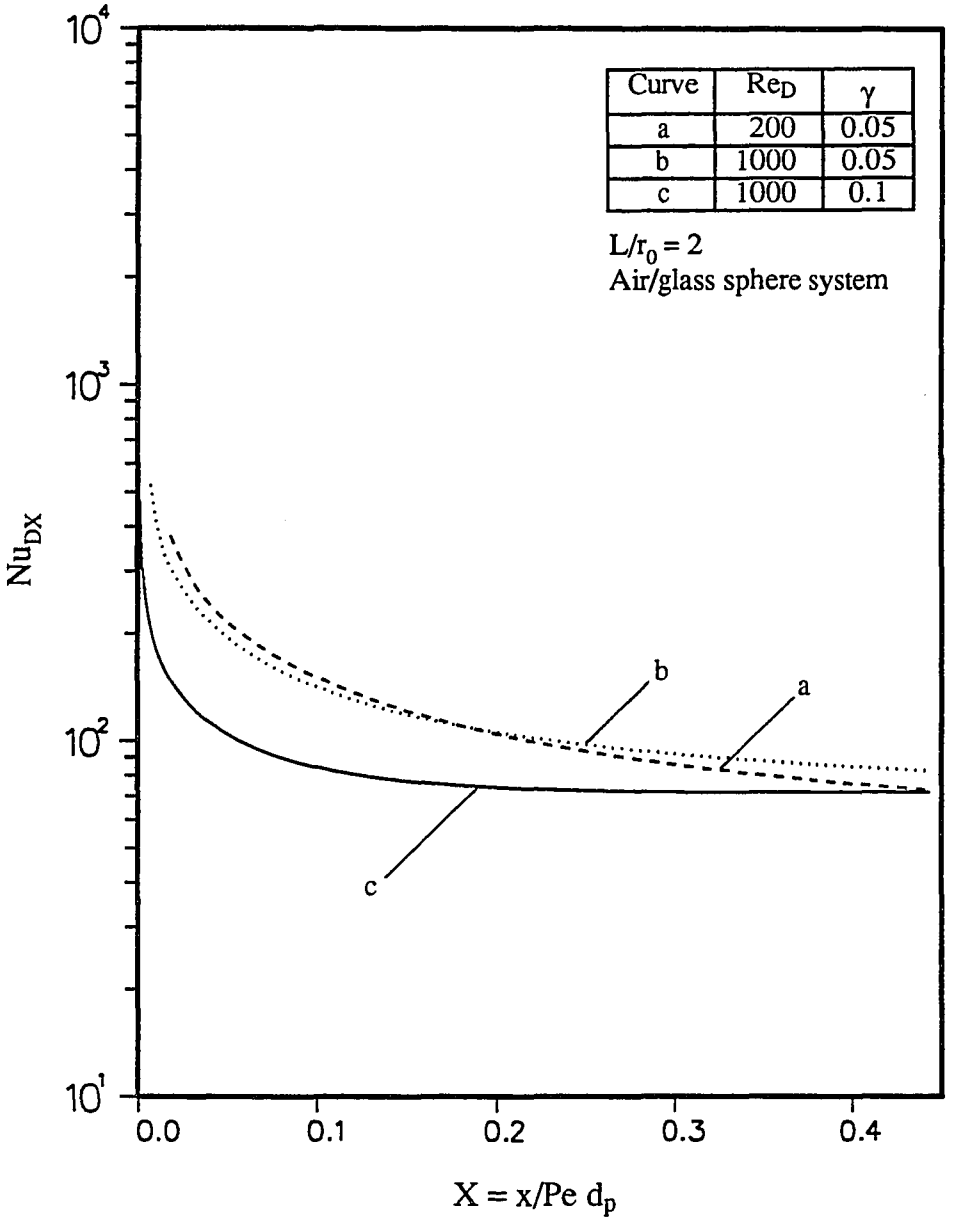

Figure 19. Effects of γ and Re_D on the local Nusselt number for forced convection in a packed tube

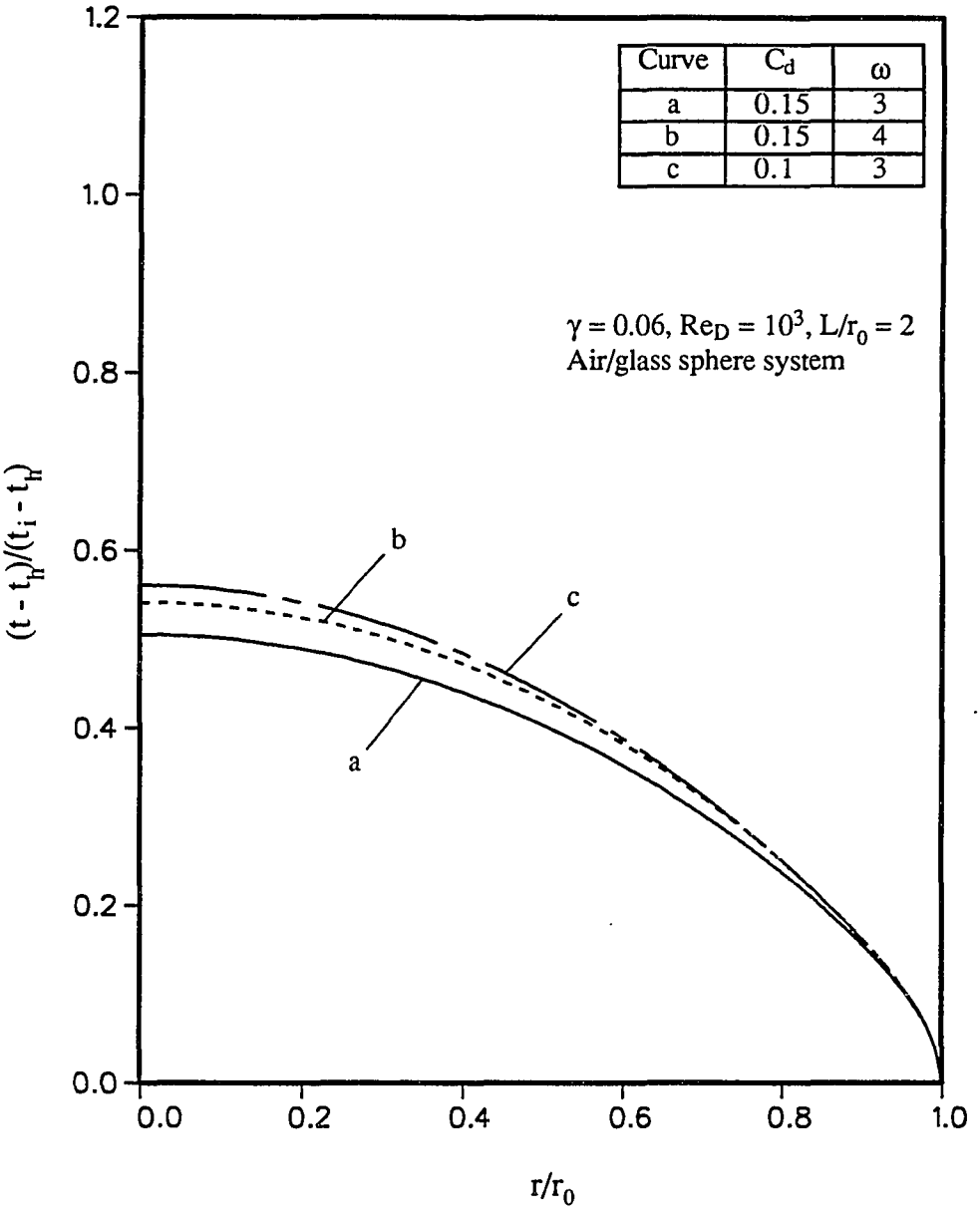

Figure 20. Effects of C_d and ω on the dimensionless temperature distribution for forced convection in a packed tube

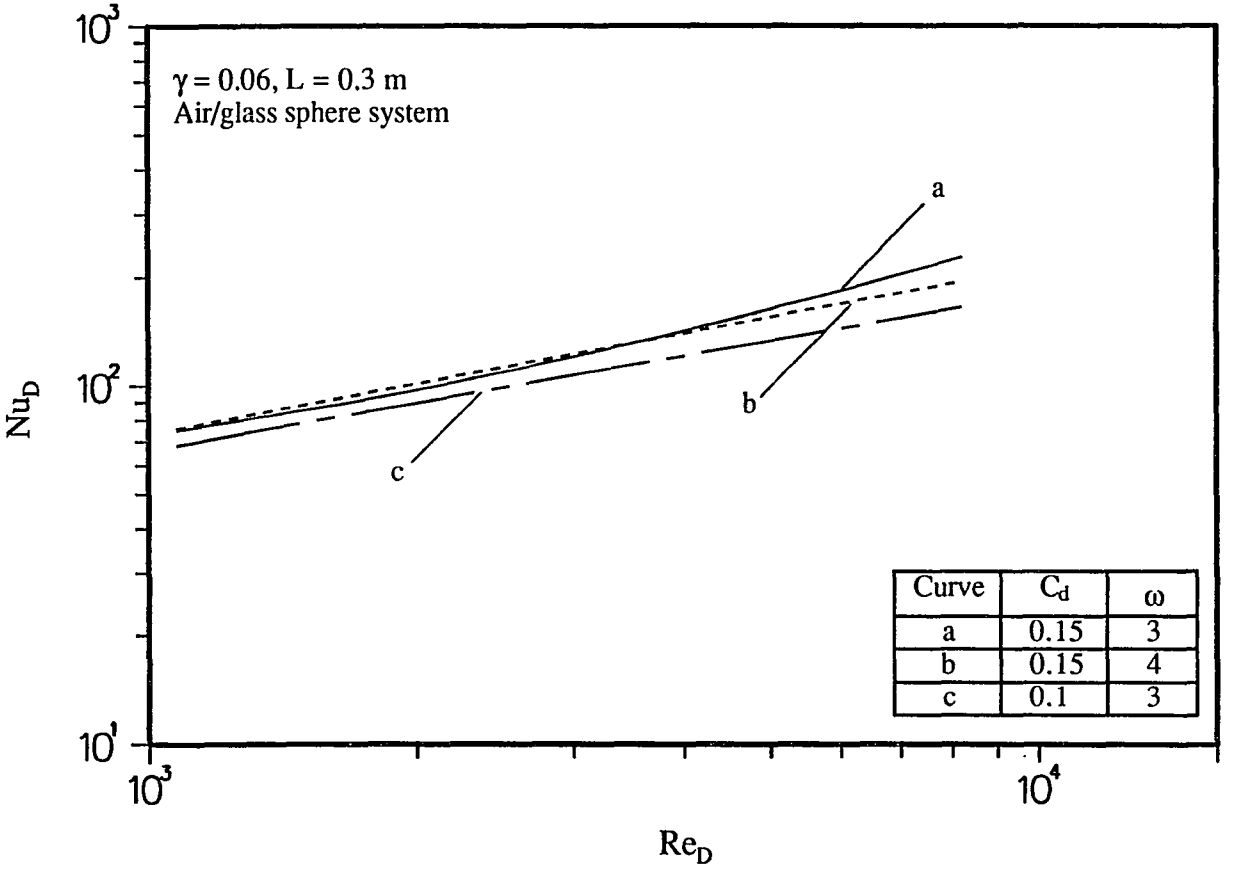

Figure 21. Effects of C_d and ω on the average Nusselt number for forced convection in a packed tube

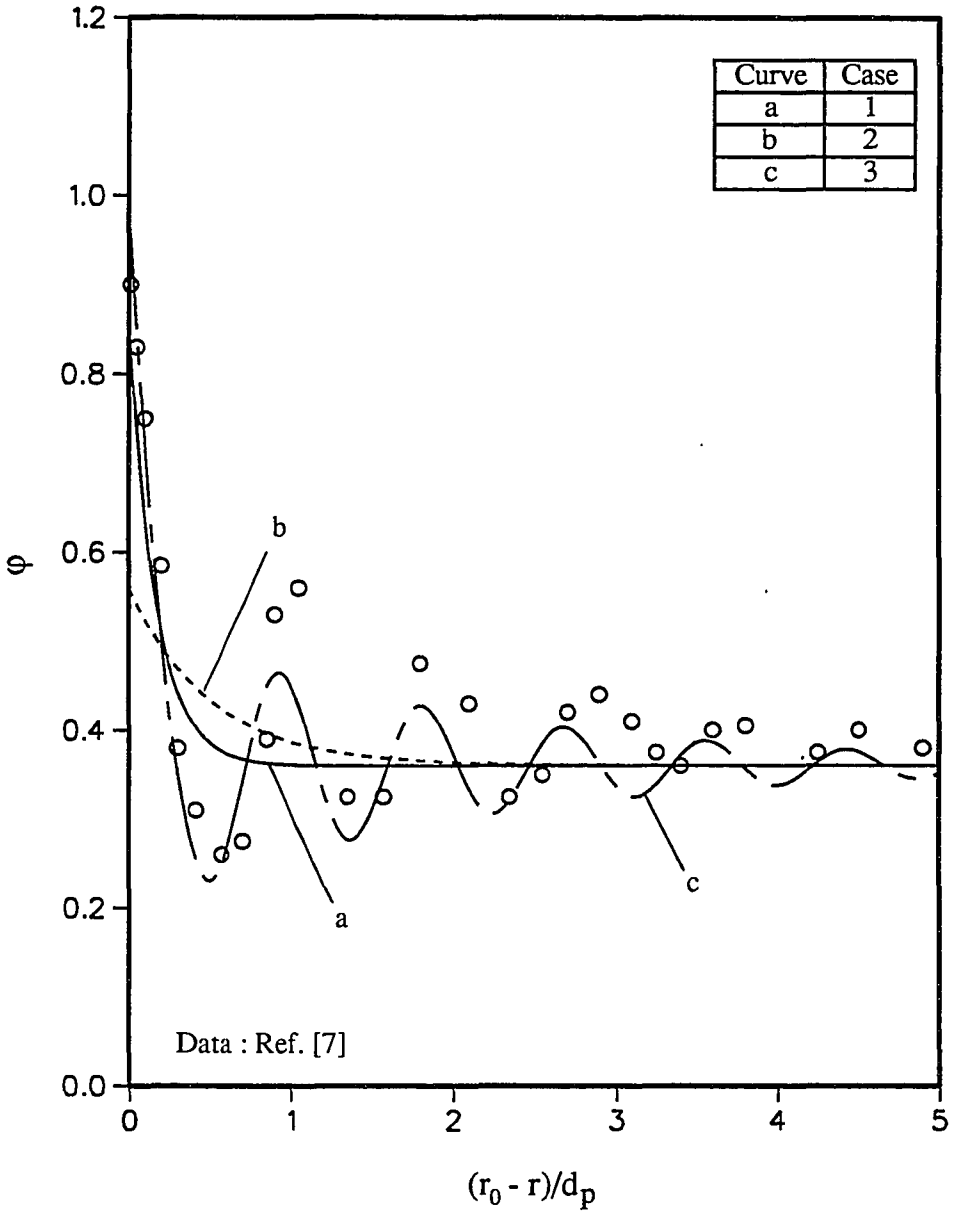

Figure 22. Porosity variation in a packed tube

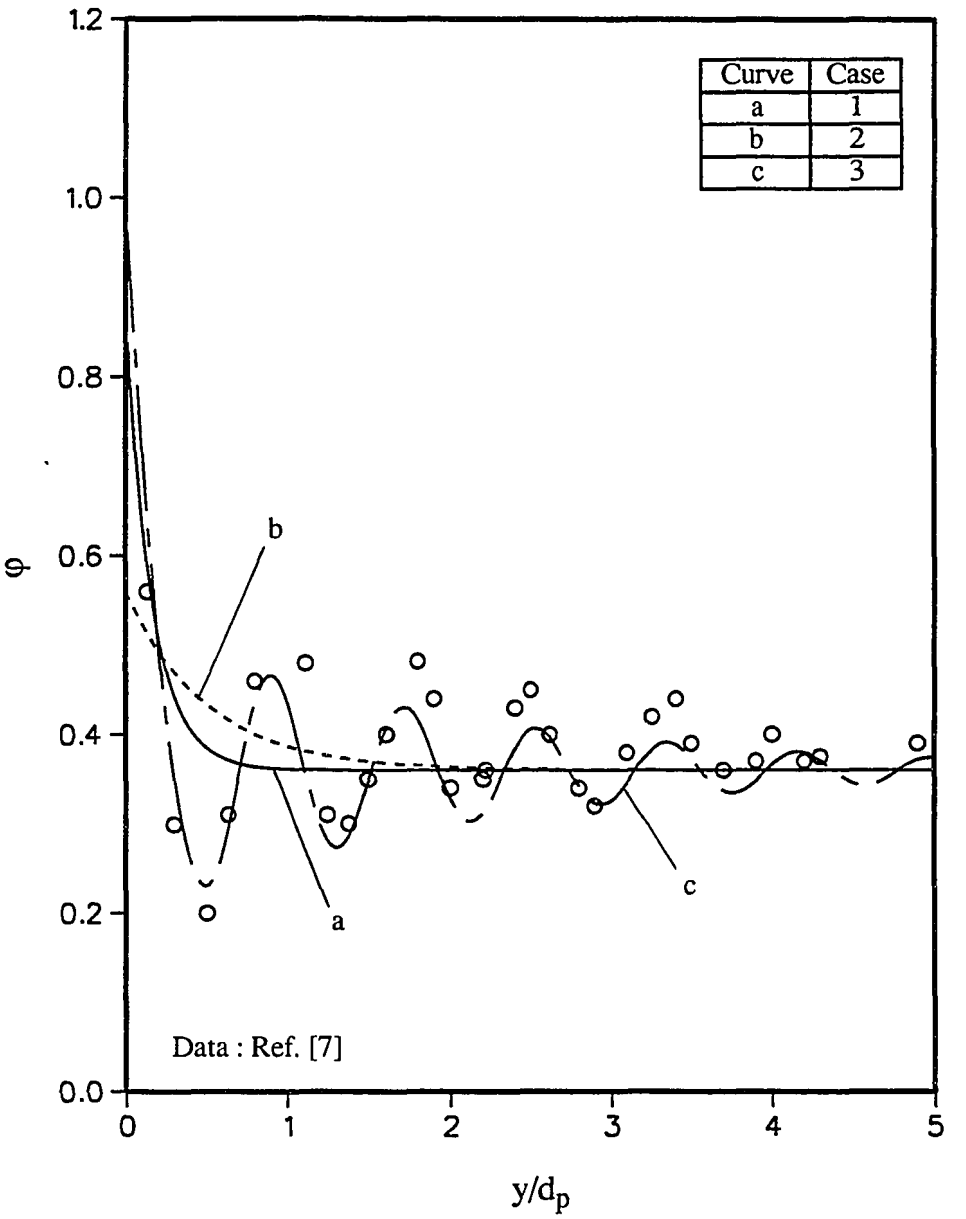

Figure 23. Porosity variation in a packed channel

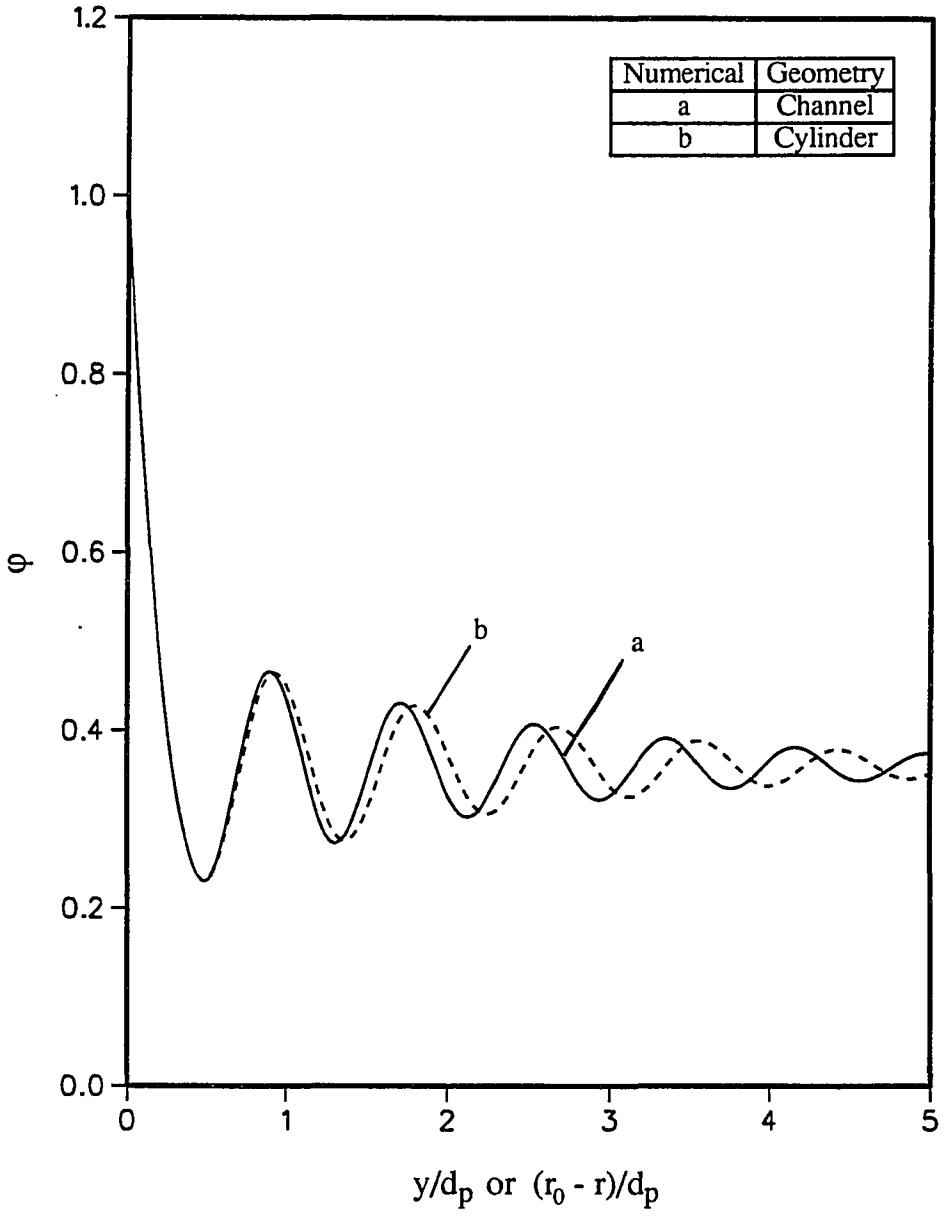

Figure 24. Comparison of the oscillating porosity function for a packed tube and a packed channel

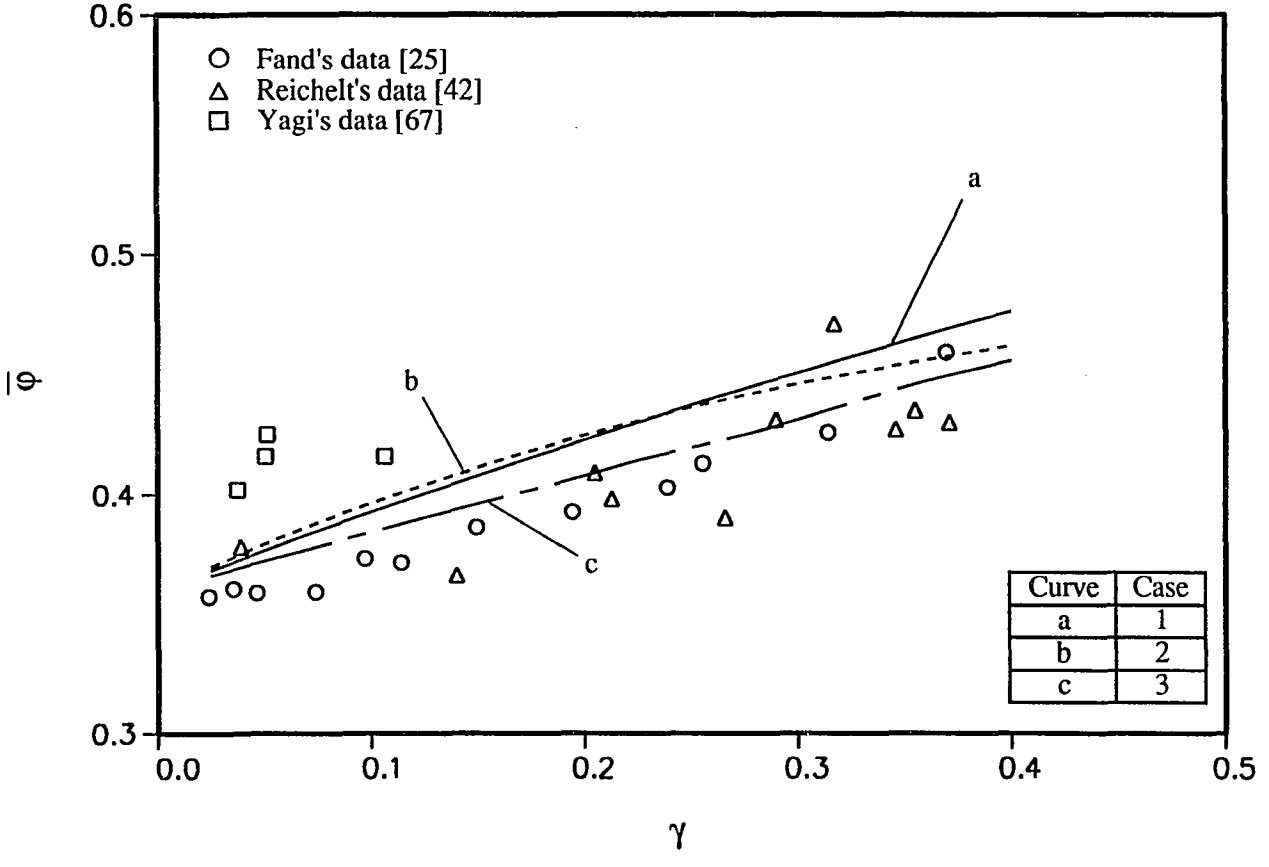

Figure 25. Comparison of the computed and observed average bed porosity

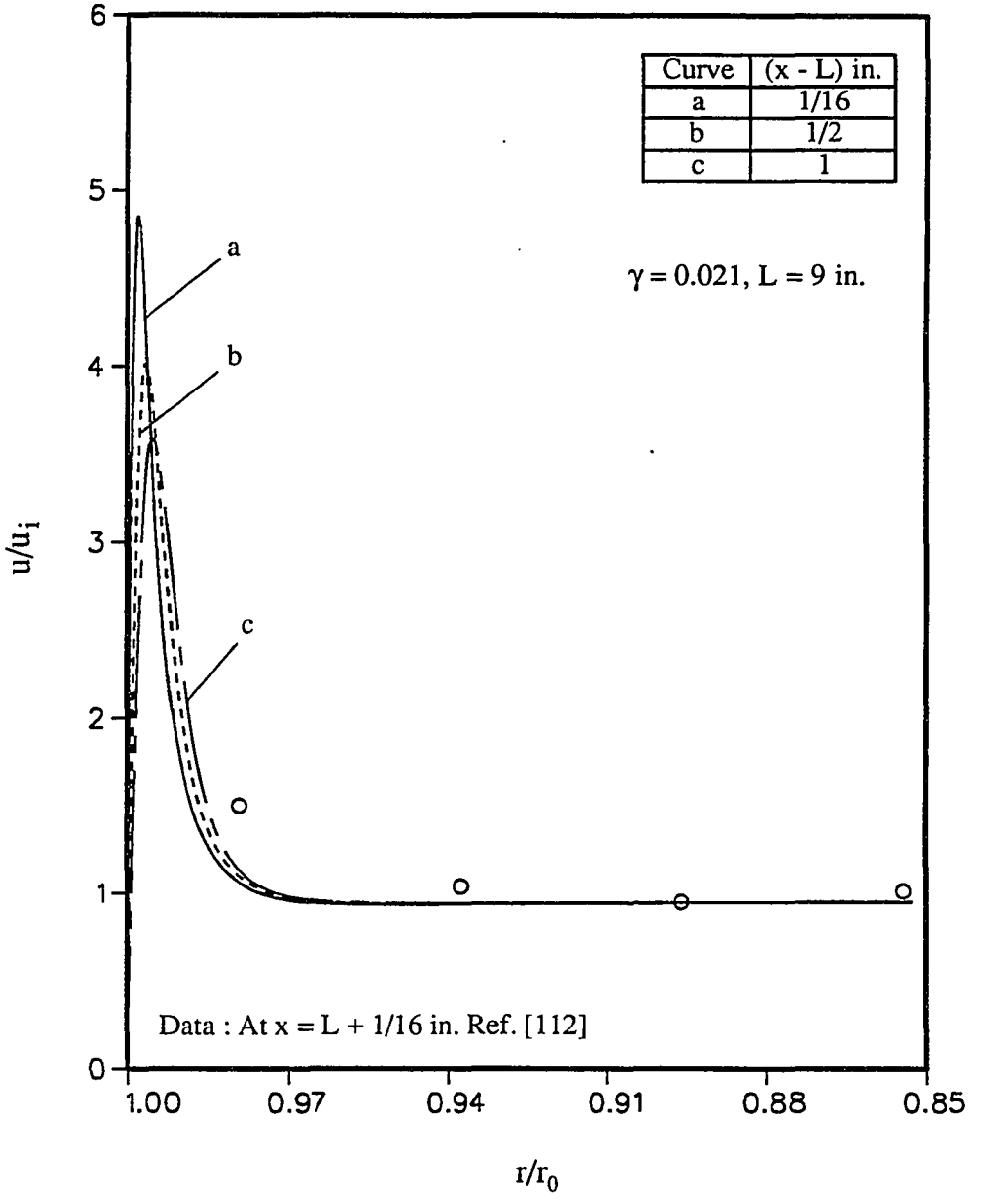

Figure 26. Comparison of the computed axial velocity profiles and Price's data for flow in a packed tube at $Re_d = 1005$

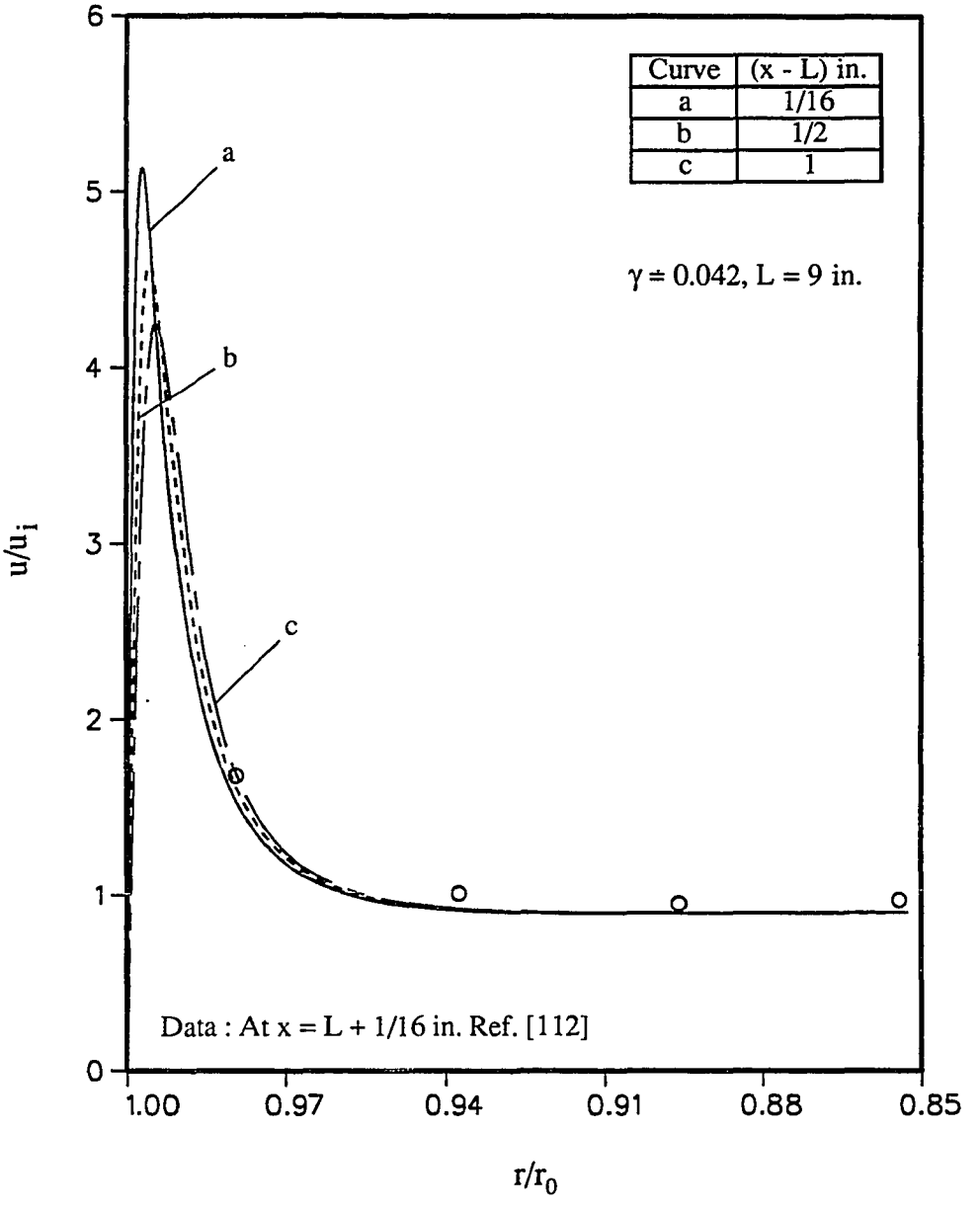

Figure 27. Comparison of the computed axial velocity profiles and Price's data for flow in a packed tube at $Re_d = 1470$

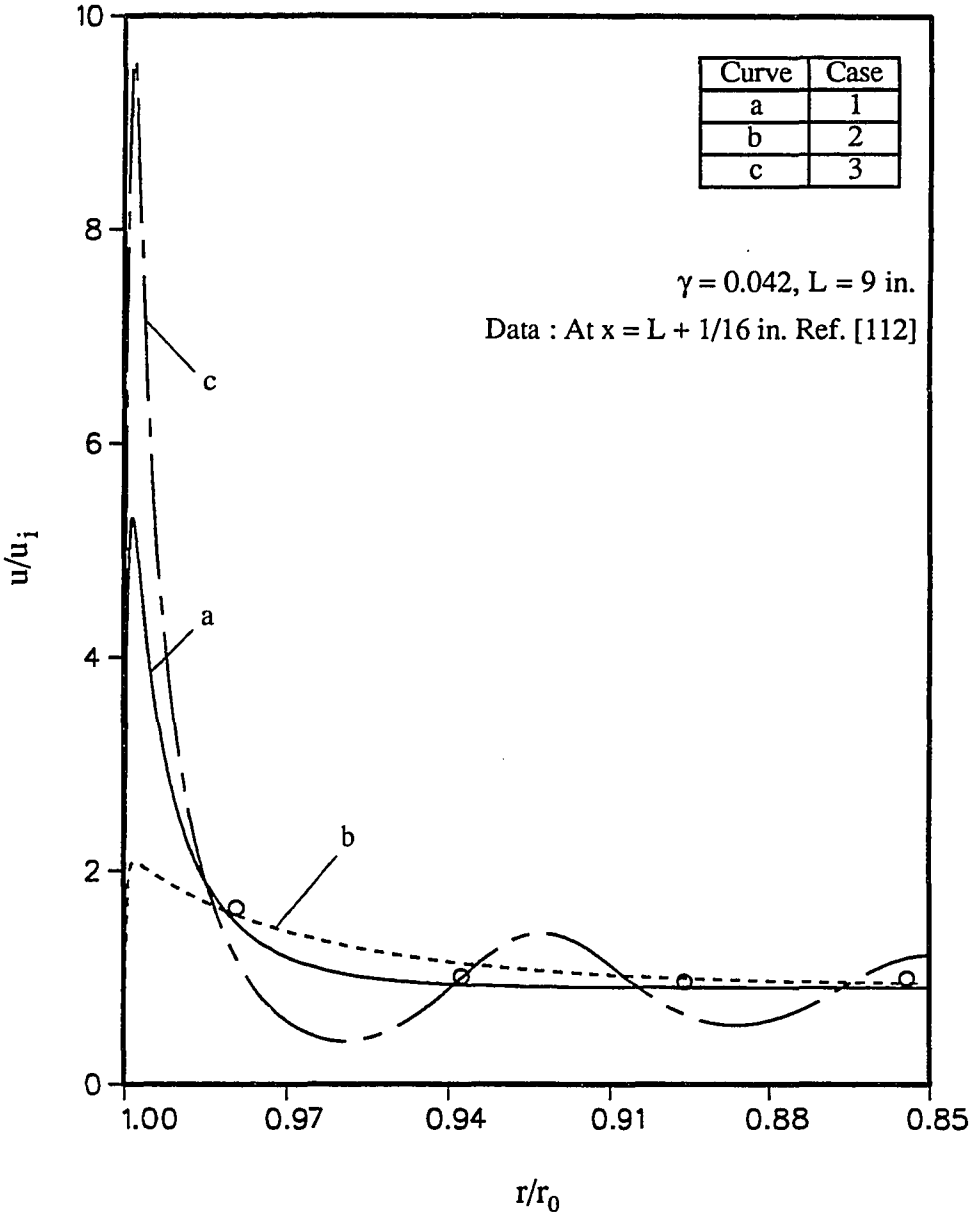

Figure 28. Effect of the porosity functions on the axial velocity distribution for flow in a packed tube at $Re_d = 4350$

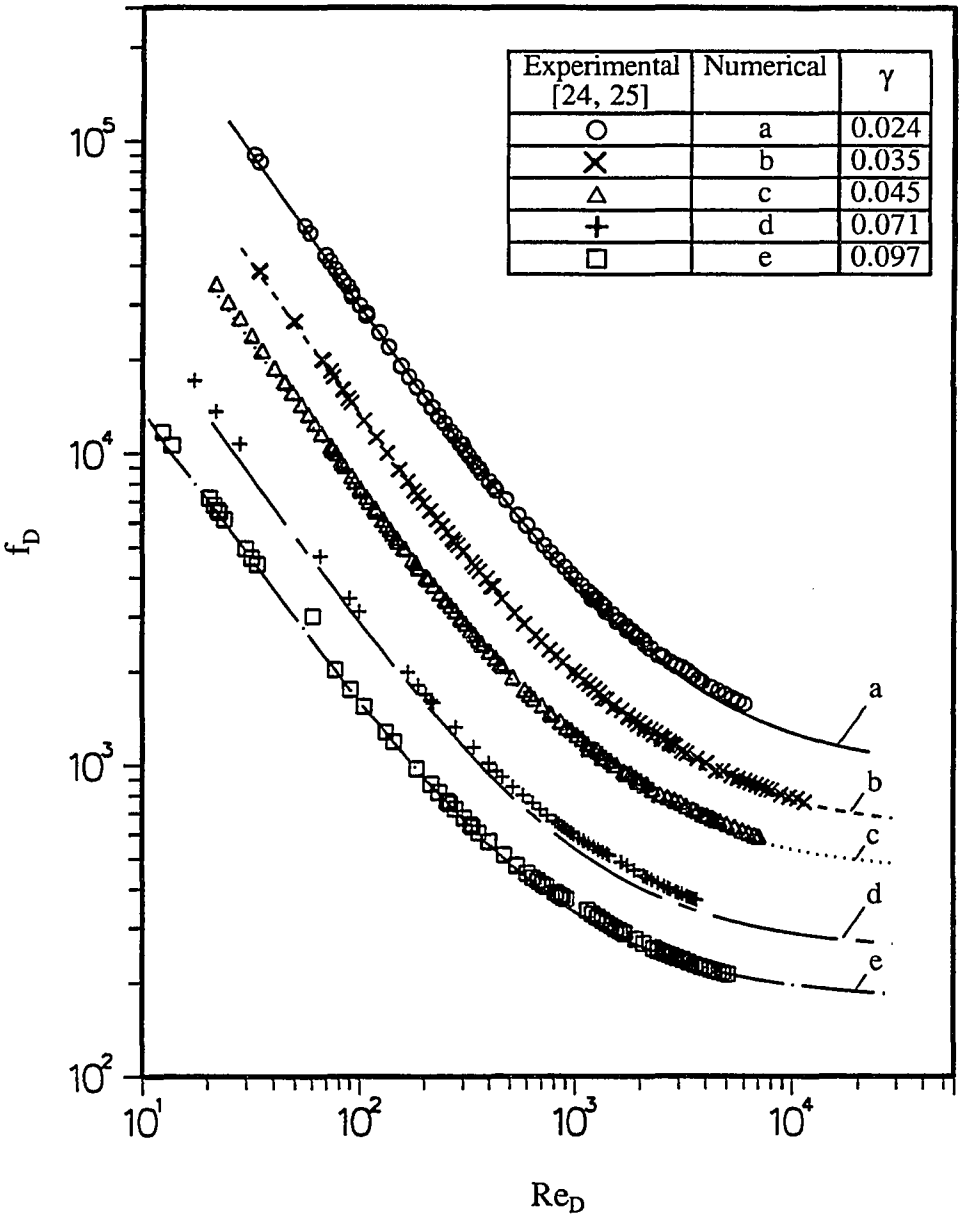

Figure 29. Comparison of the computed dimensionless pressure drop and Fand's data for flow in a packed tube

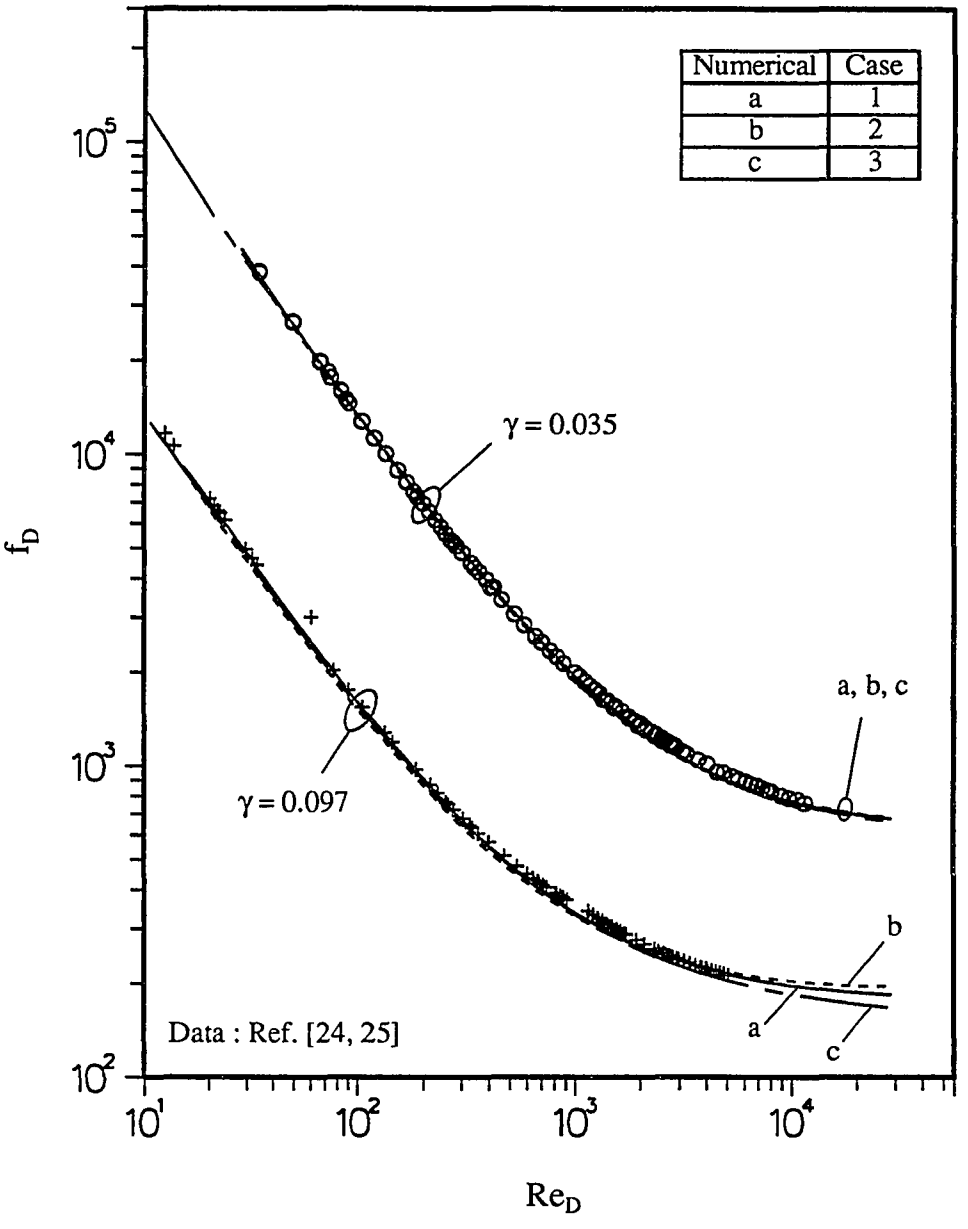

Figure 30. Effect of the porosity functions on the dimensionless pressure drop for flow in a packed tube

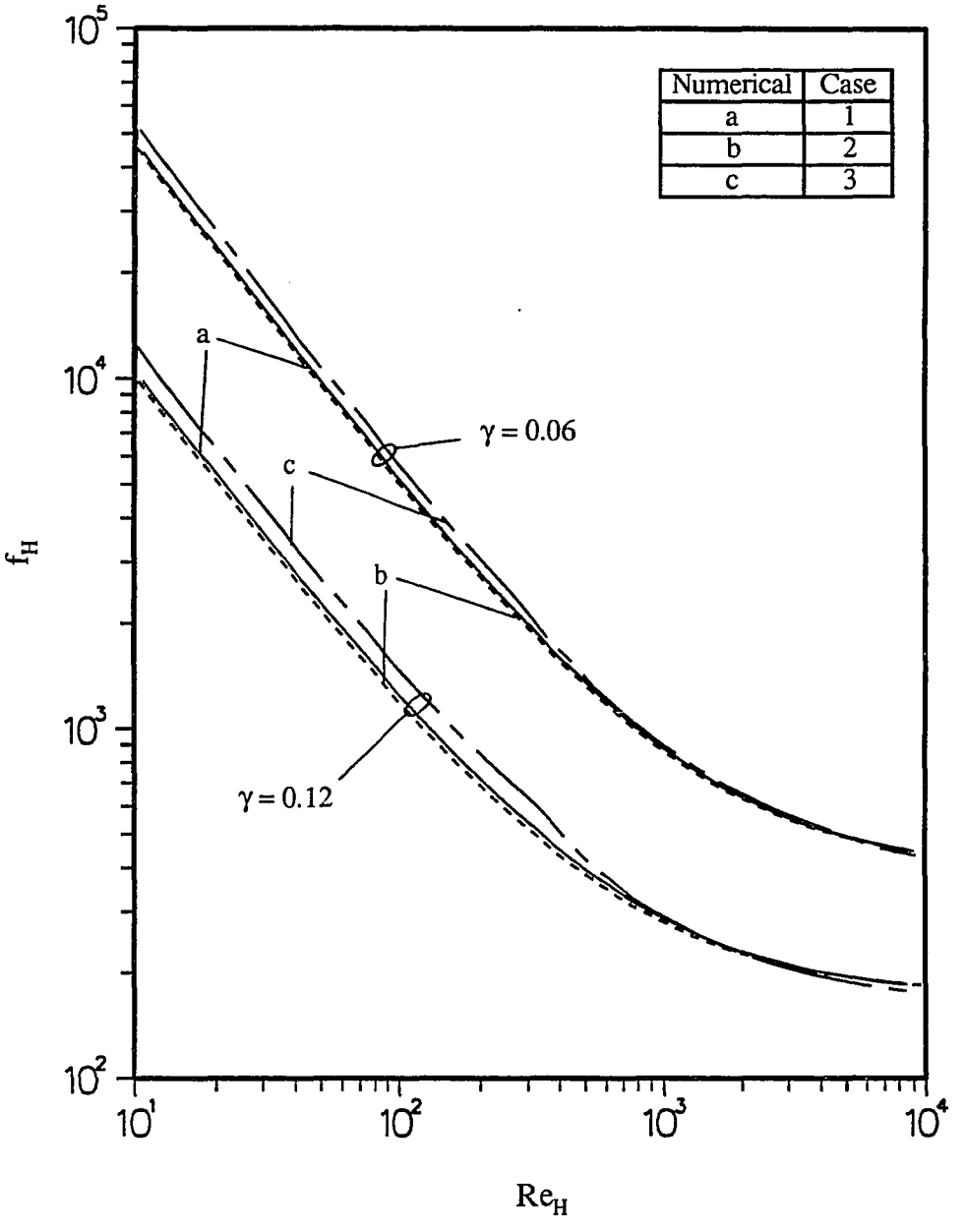

Figure 31. Effect of the porosity functions on the dimensionless pressure drop for flow in a packed channel

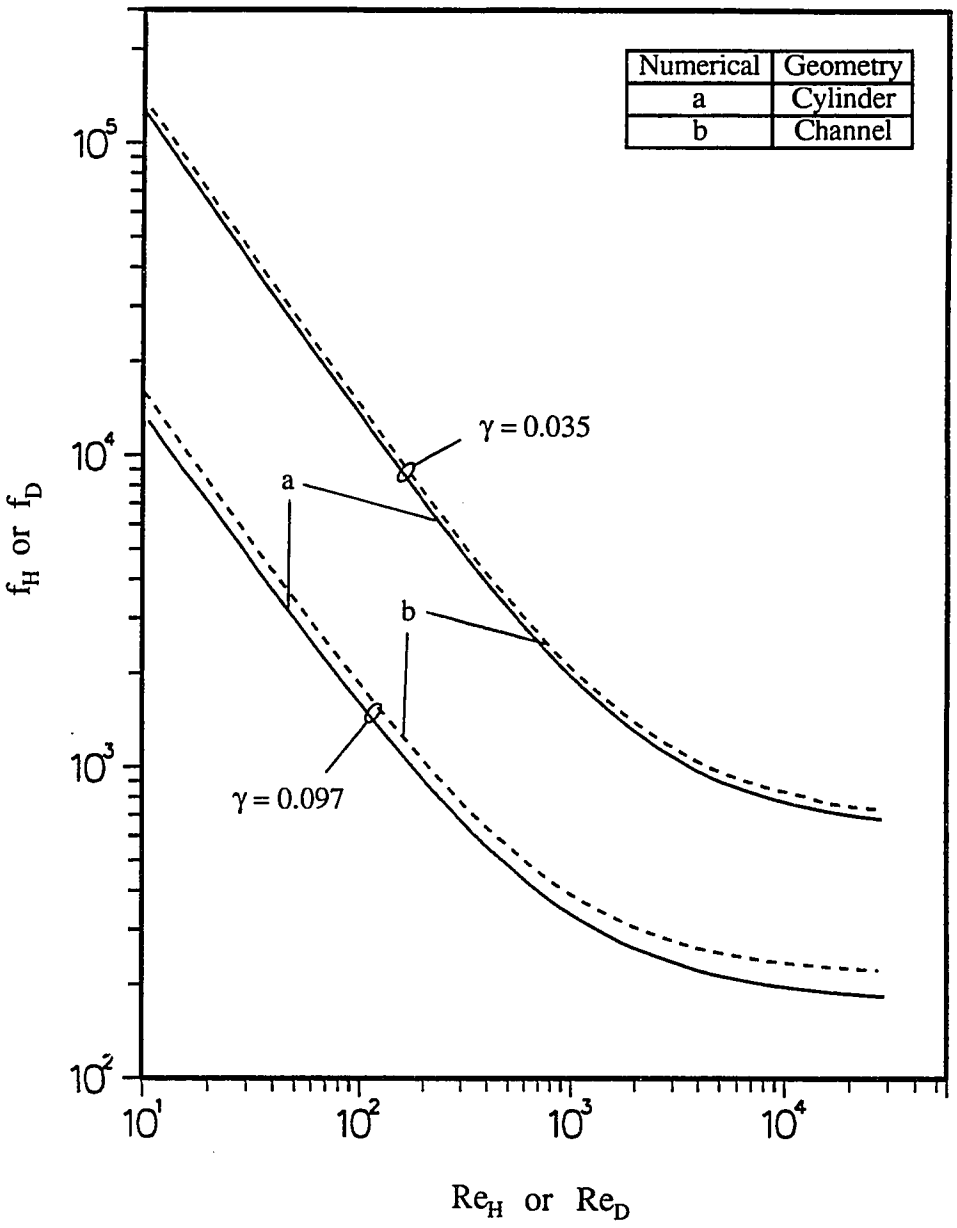

Figure 32. Comparison of the computed dimensionless pressure drop in a packed tube and a packed channel

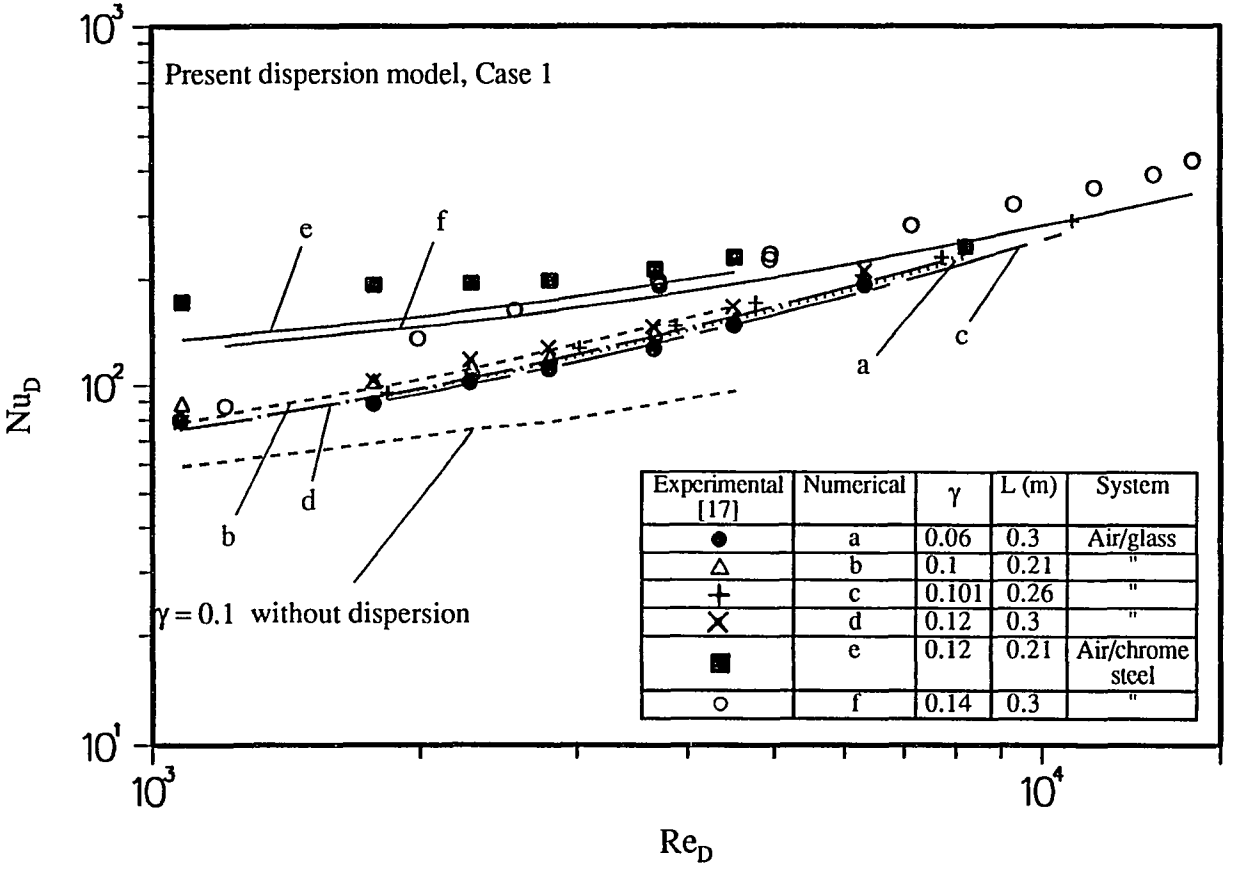

Figure 33. Comparison of the predicted average Nusselt number and Verschoor & Schuit's data for forced convection in a packed tube

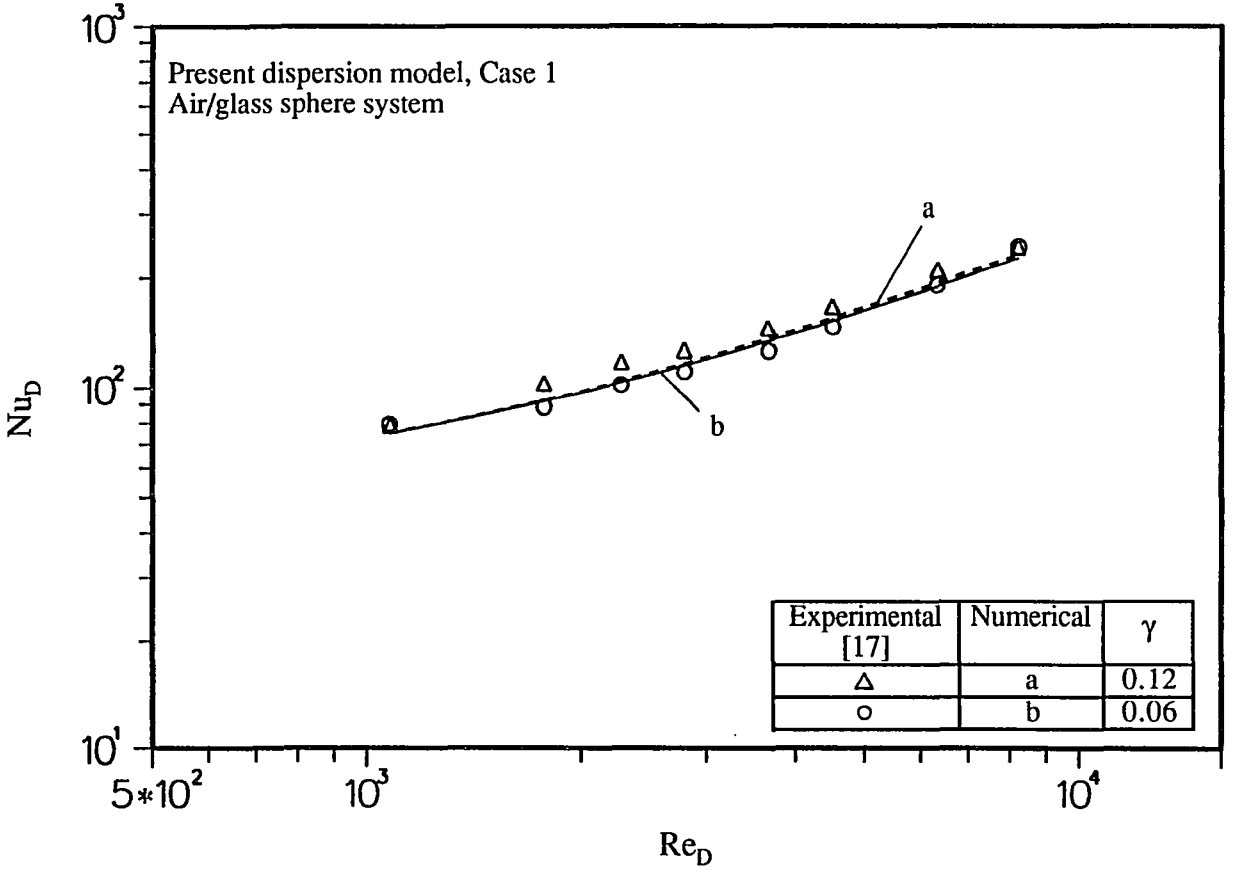

Figure 34. Effect of γ on the average Nusselt number for forced convection in a packed tube (L = 0.3 m)

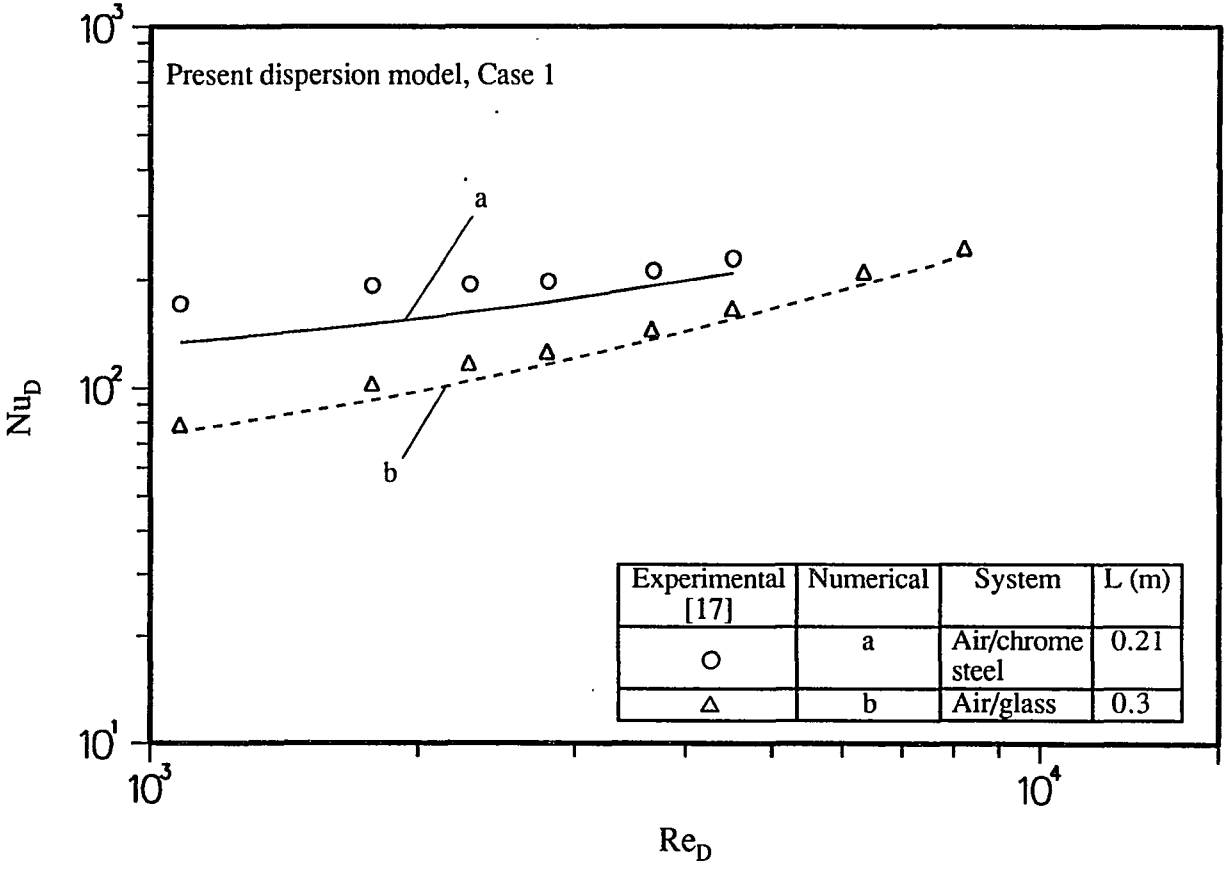

Figure 35. Effect of λ on the average Nusselt number for forced convection in a packed tube ($\gamma = 0.12$)

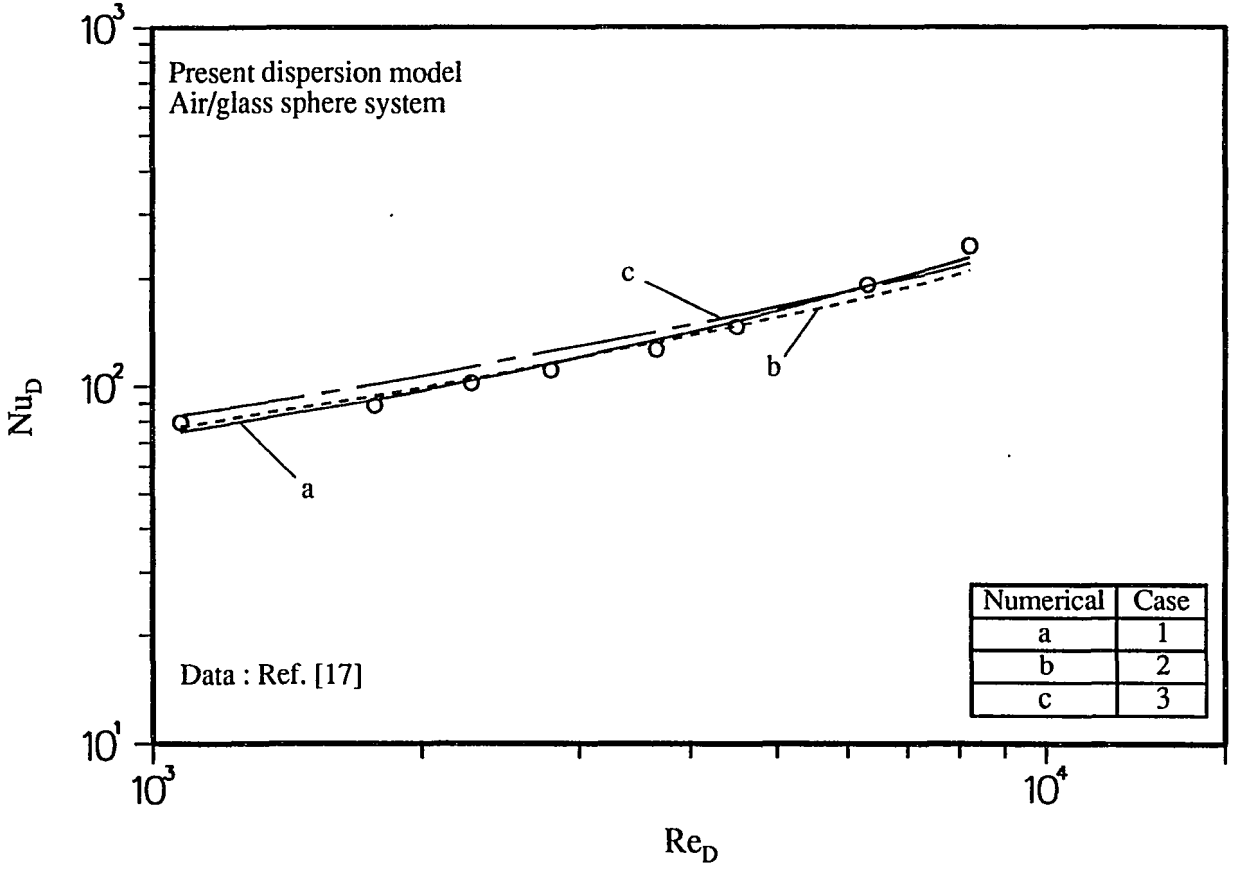

Figure 36. Effect of the porosity functions on the average Nusselt number for forced convection in a packed tube ($\gamma = 0.06$, L = 0.3 m)

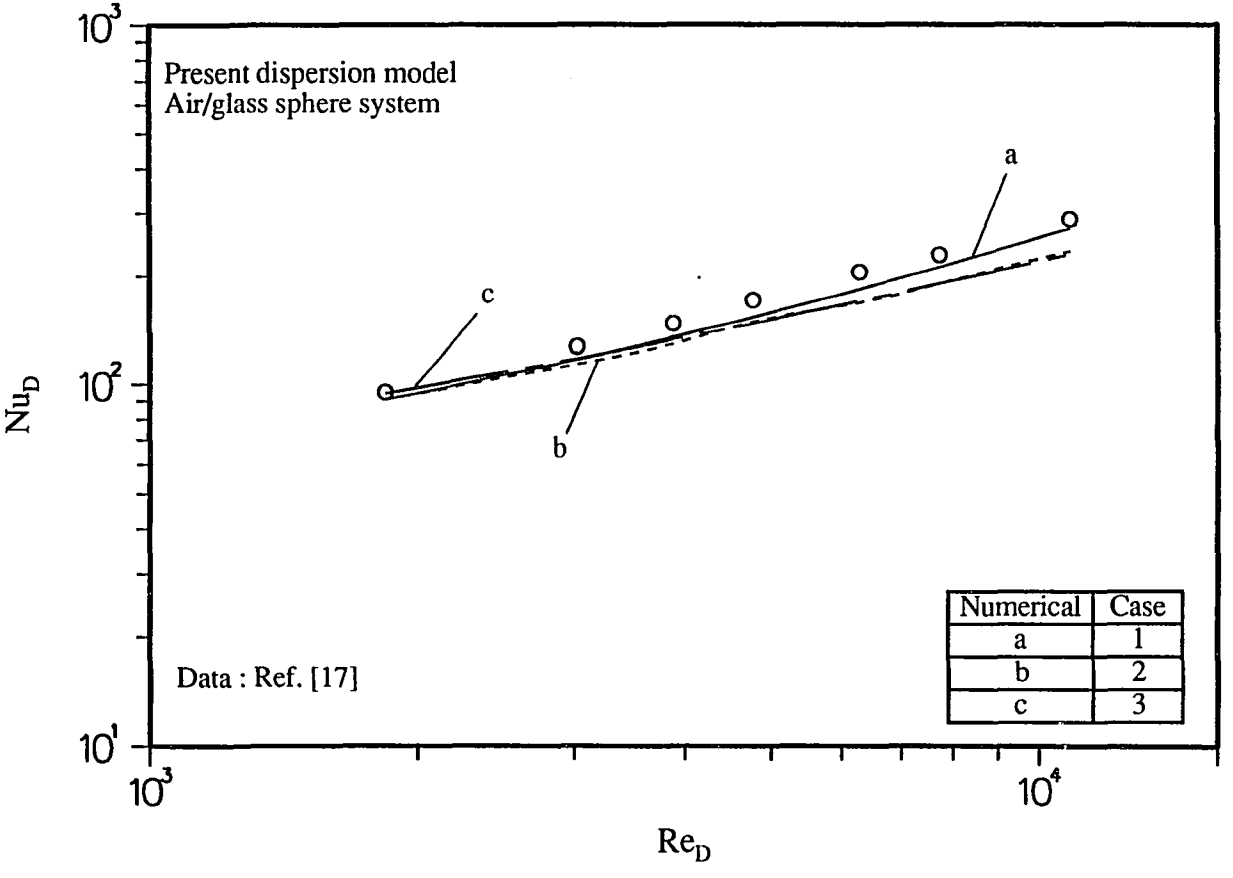

Figure 37. Effect of the porosity functions on the average Nusselt number for forced convection in a packed tube ($\gamma = 0.101$, L = 0.26 m)

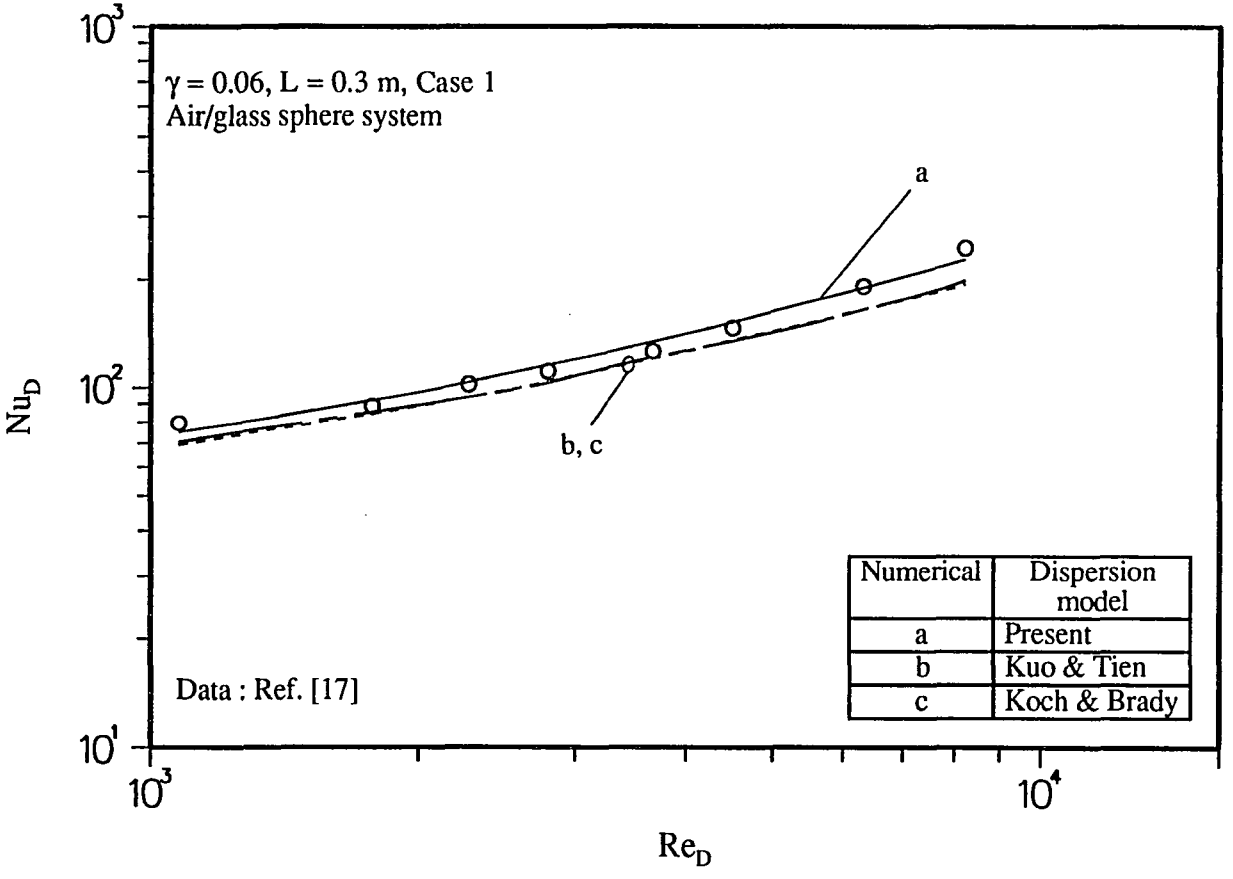

Figure 38. Comparison of the average Nusselt number using different dispersion models for forced convection in a packed tube

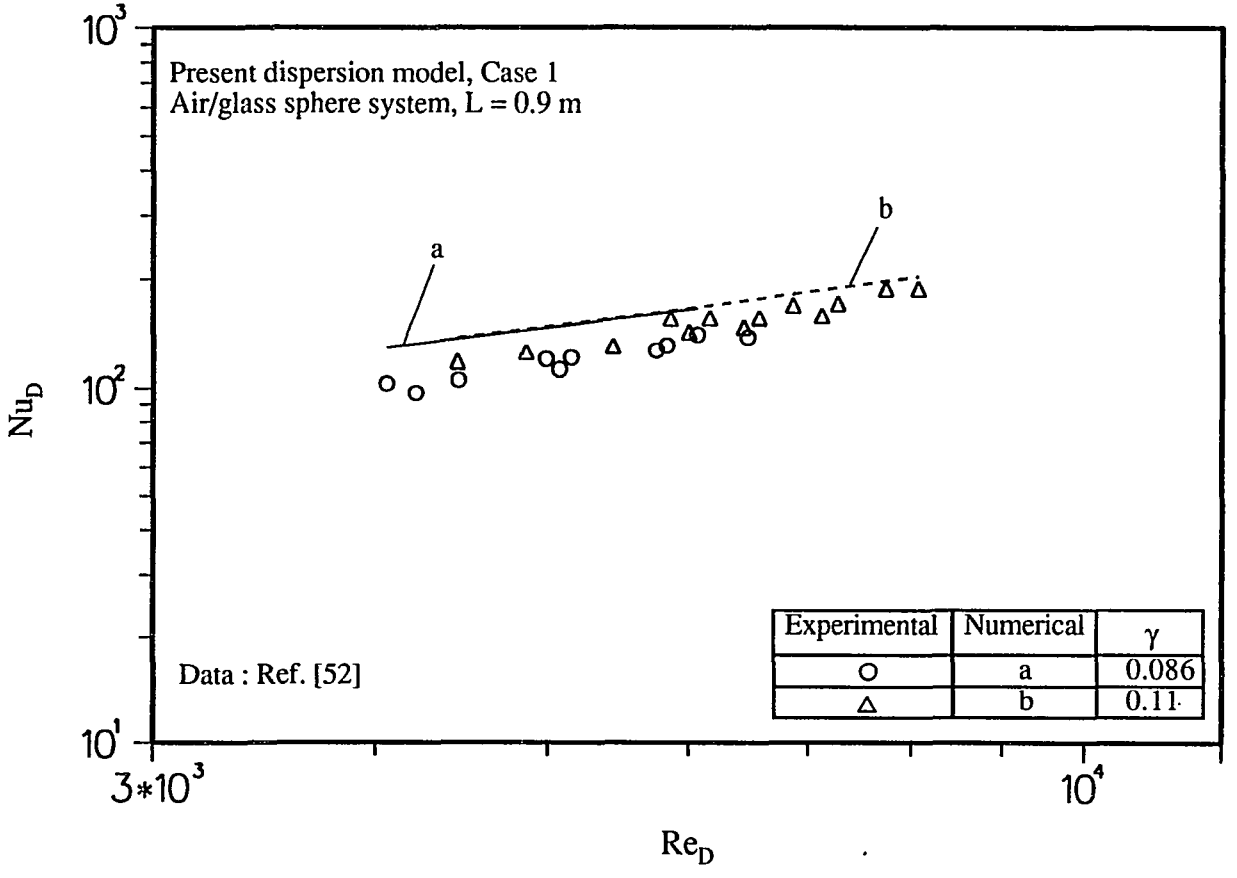

Figure 39. Comparison of the predicted average Nusselt number and Leva's data for forced convection in a packed tube

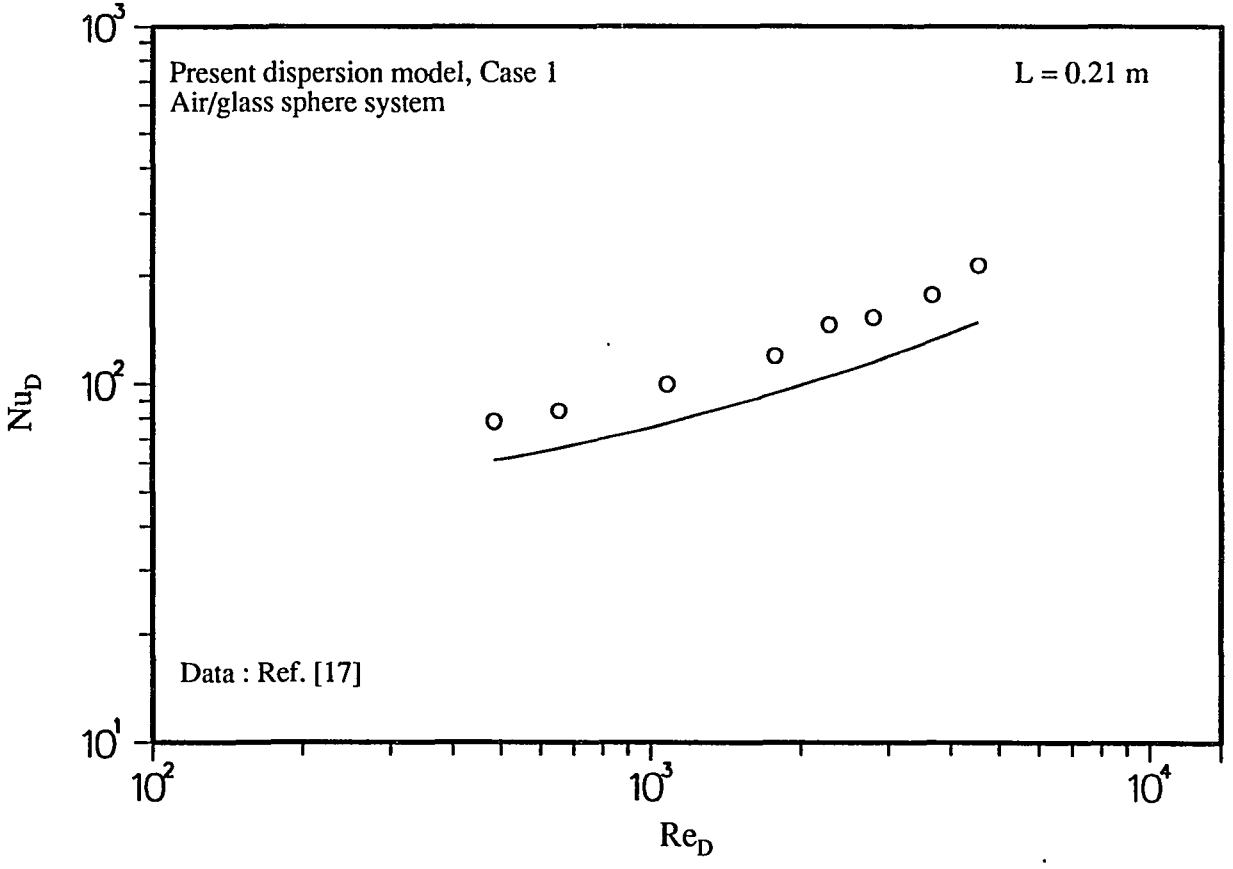

Figure 40. Comparison of the predicted and observed average Nusselt number for forced convection in a packed tube for $\gamma = 0.151$

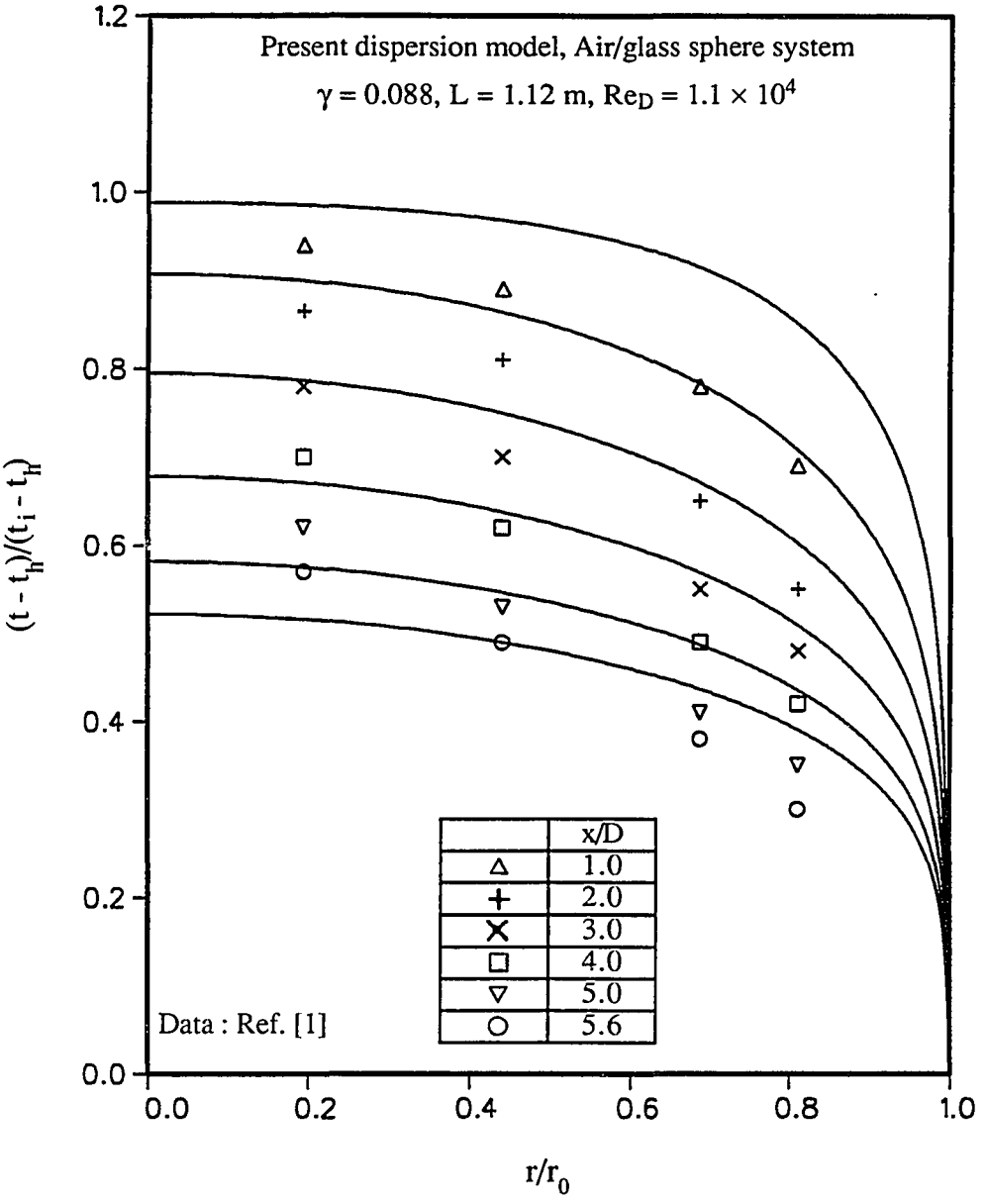

Figure 41. Comparison of the computed (Case 1) temperature distribution and Plautz & Johnstone's data for forced convection in a packed tube

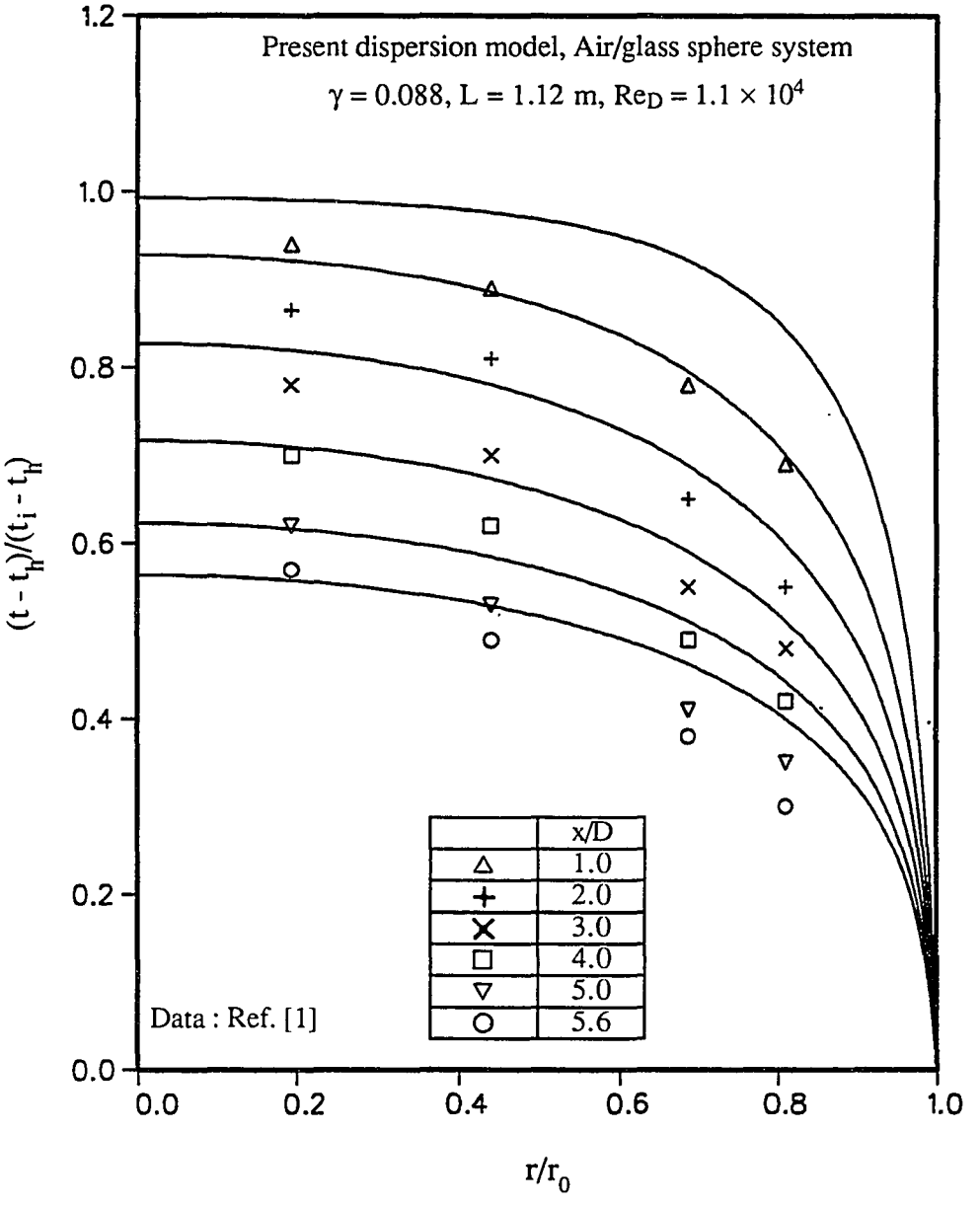

Figure 42. Comparison of the computed (Case 2) temperature distribution and Plautz & Johnstone's data for forced convection in a packed tube

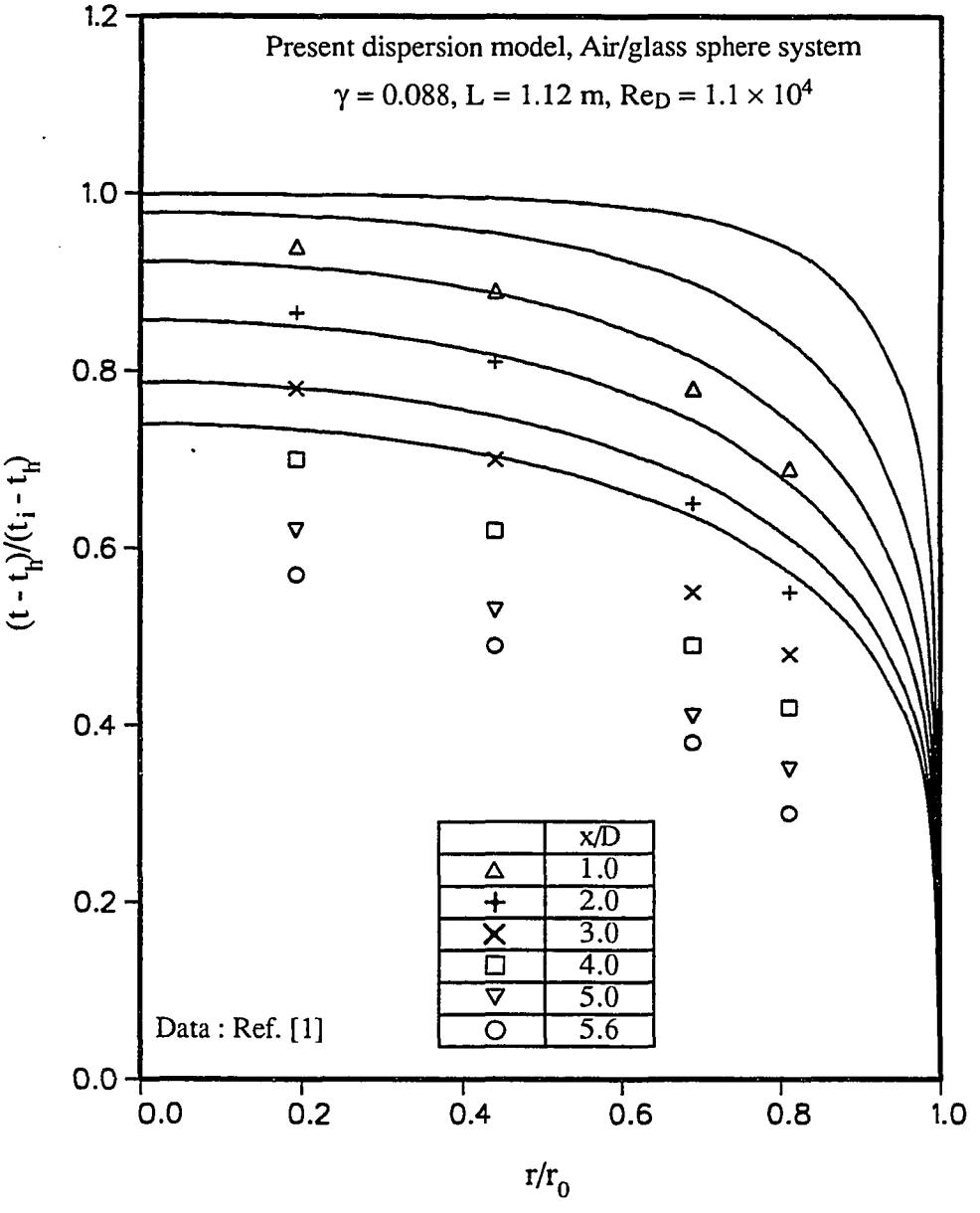

Figure 43. Comparison of the computed (Case 3) temperature distribution and Plautz & Johnstone's data for forced convection in a packed tube

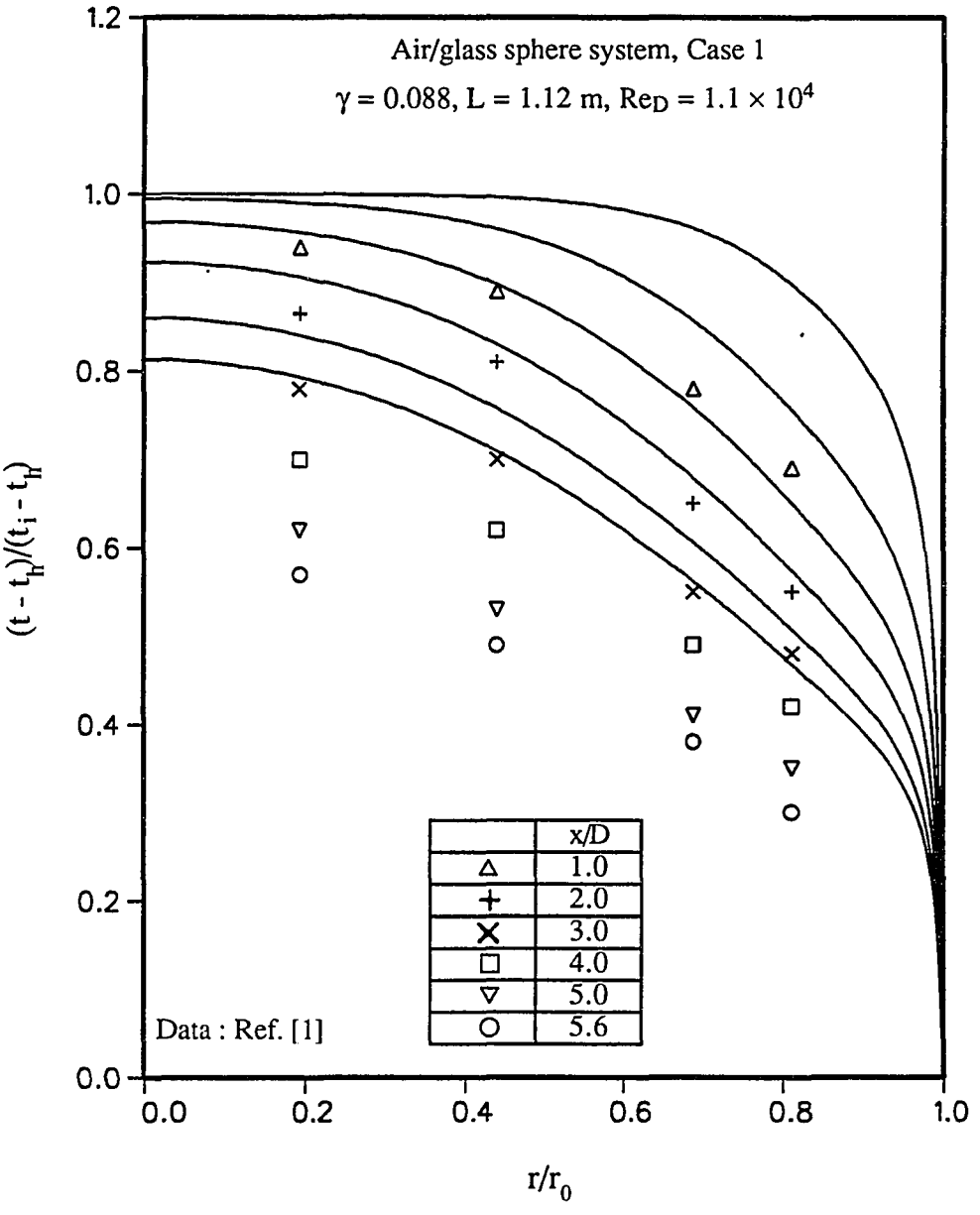

Figure 44. Comparison of the computed temperature distribution based on Kuo & Tien's dispersion model and Plautz & Johnstone's temperature data for forced convection in a packed tube

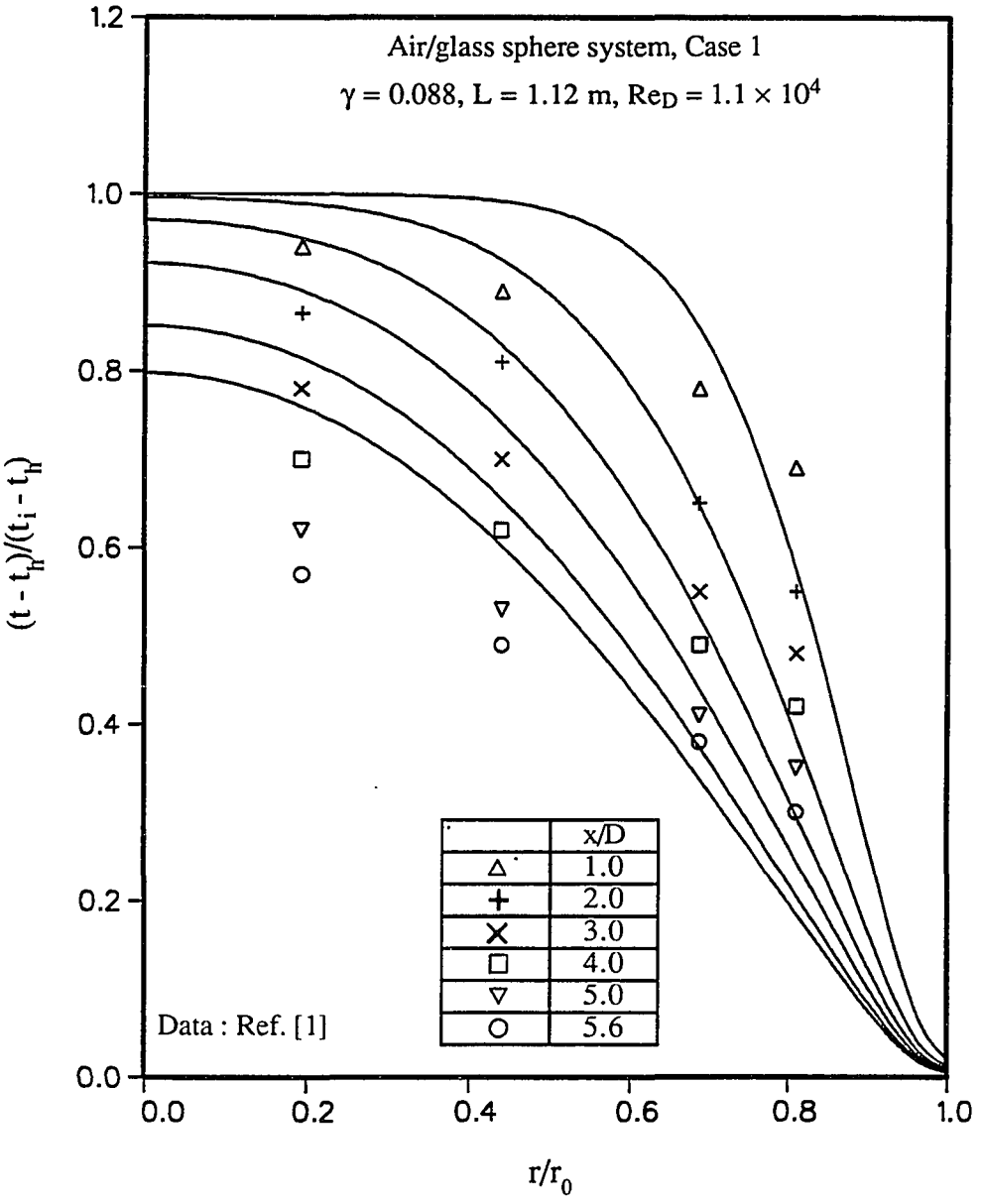

Figure 45. Comparison of the computed temperature distribution based on Koch & Brady's dispersion model and Plautz & Johnstone's temperature data for forced convection in a packed tube

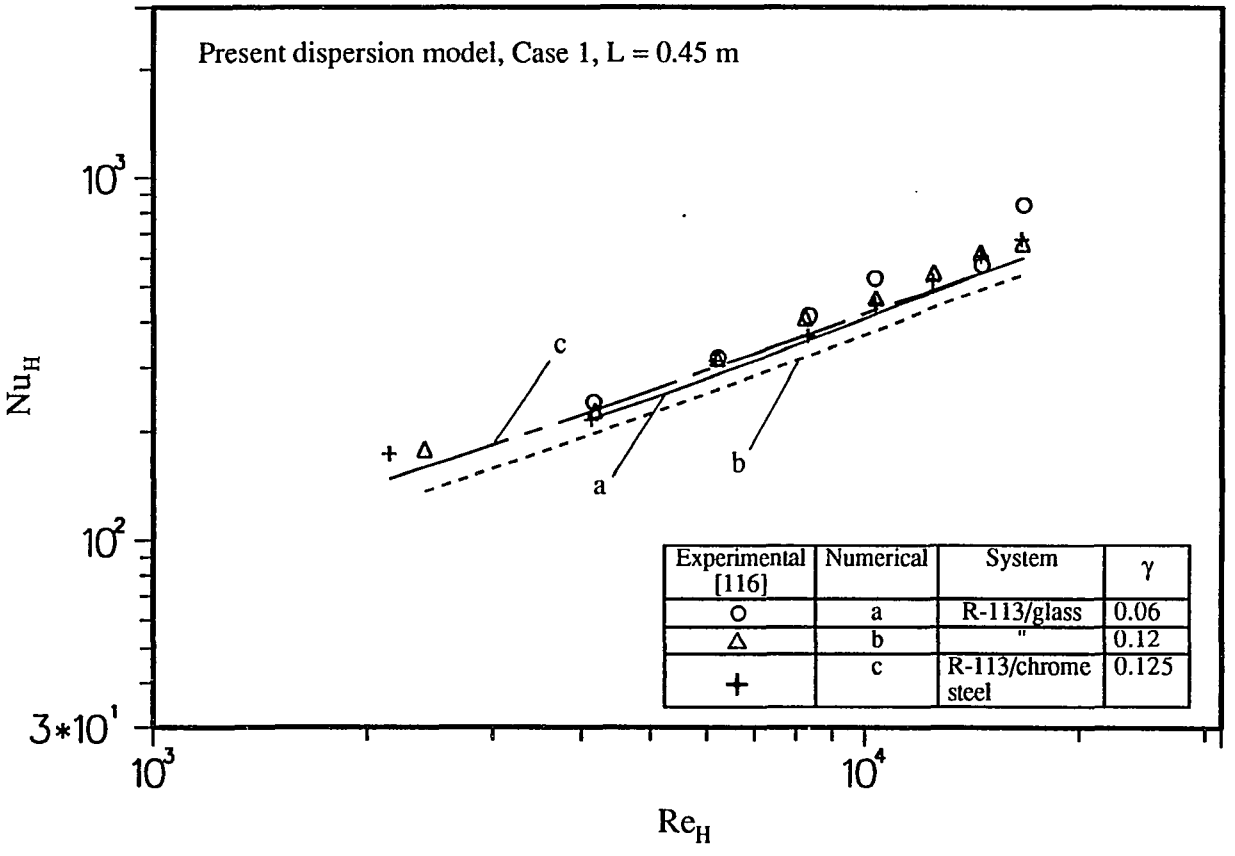

Figure 46. Comparison of the predicted and observed average Nusselt number corresponding to Cai's experiments for forced convection in a packed channel

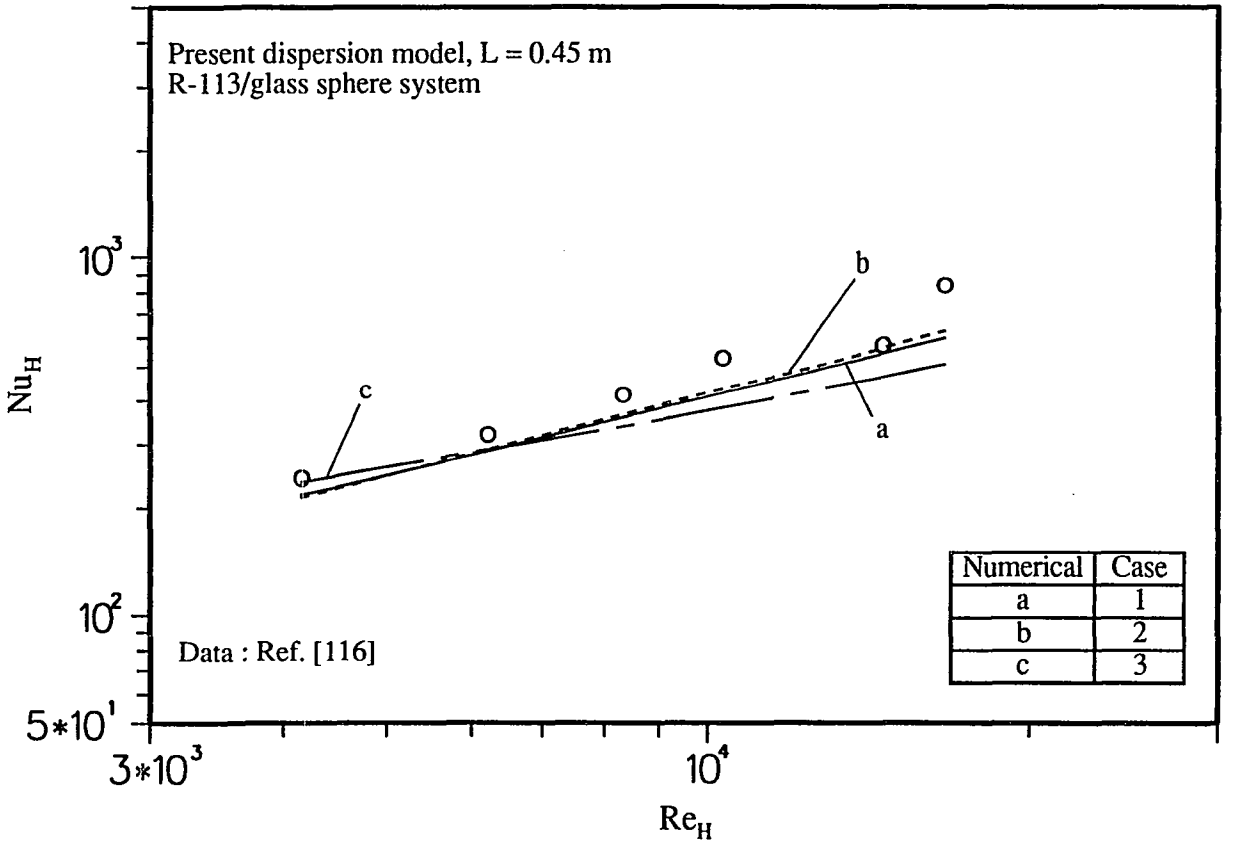

Figure 47. Effect of the porosity functions on the average Nusselt number for forced convection in a packed channel ($\gamma = 0.06$)

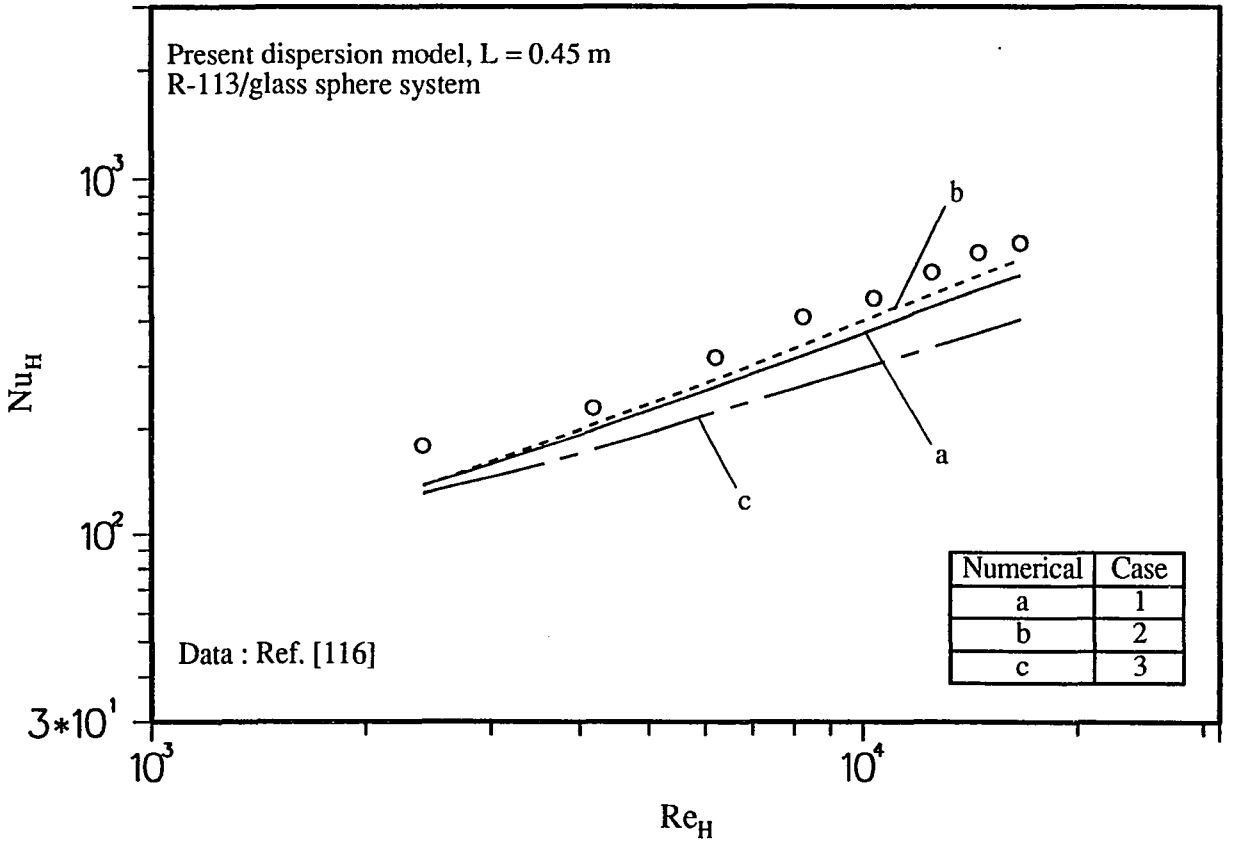

Figure 48. Effect of the porosity functions on the average Nusselt number for forced convection in a packed channel ($\gamma = 0.12$)

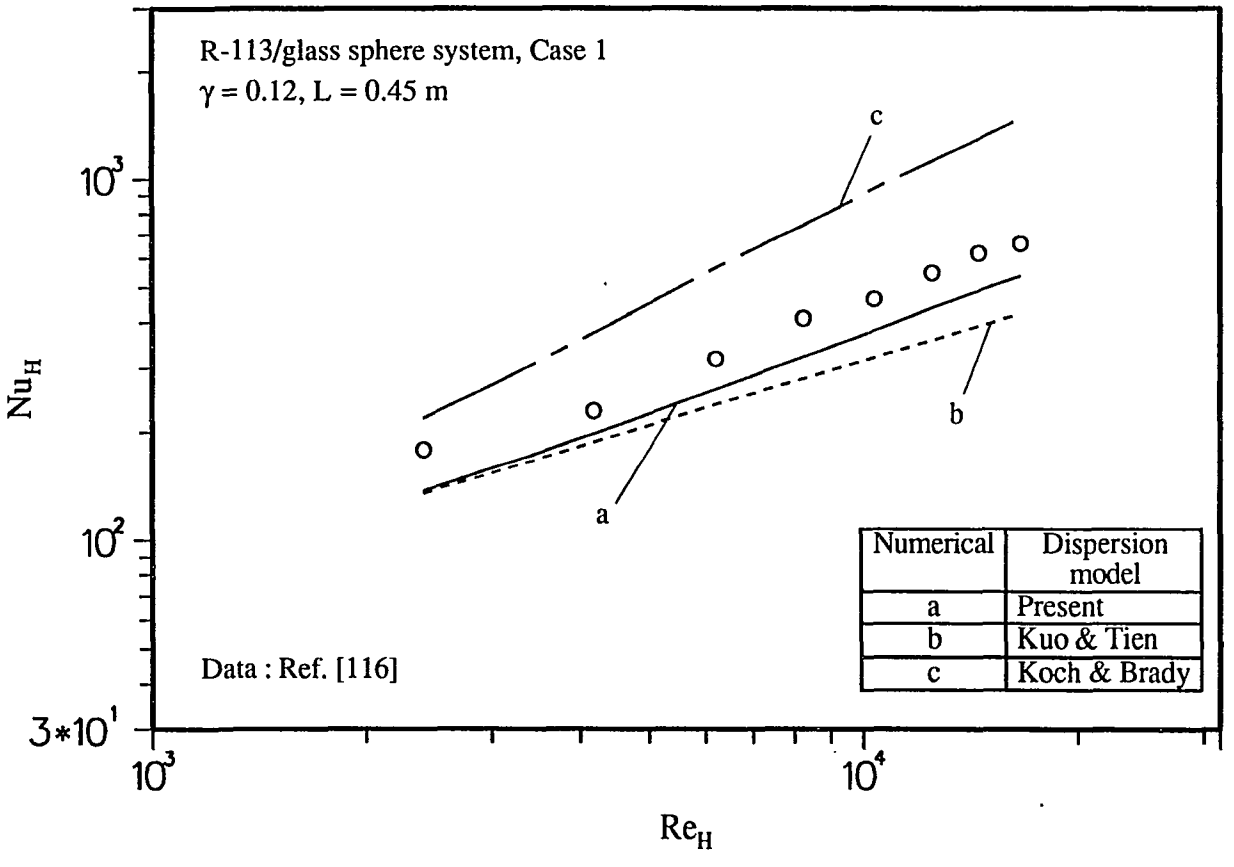

Figure 49. Comparison of the average Nusselt number using different dispersion models and Cai's experiments for forced convection in a packed channel

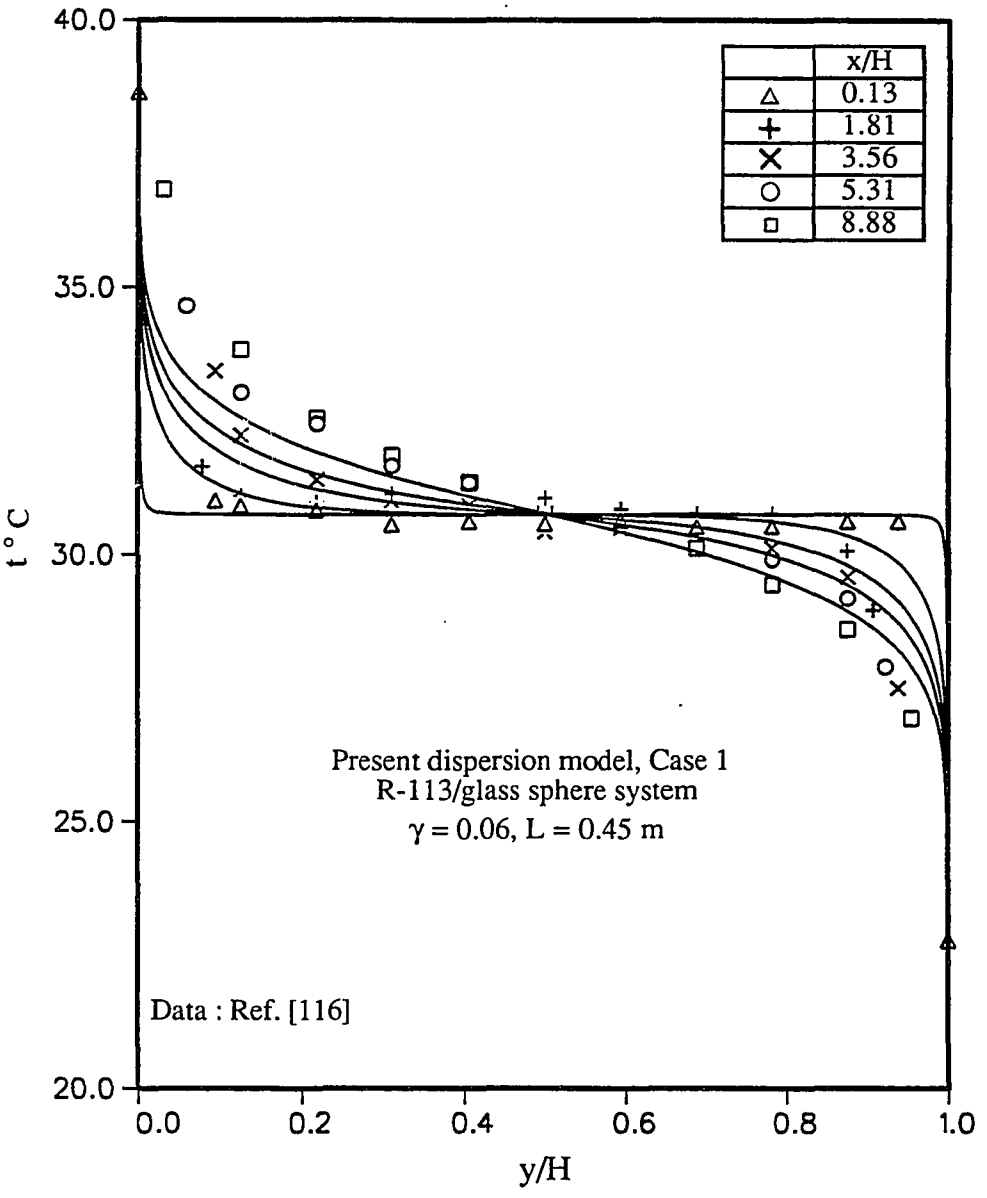

Figure 50. Comparison of the computed temperature distribution and Cai's data for forced convection in a packed channel at $Re_H = 4161$

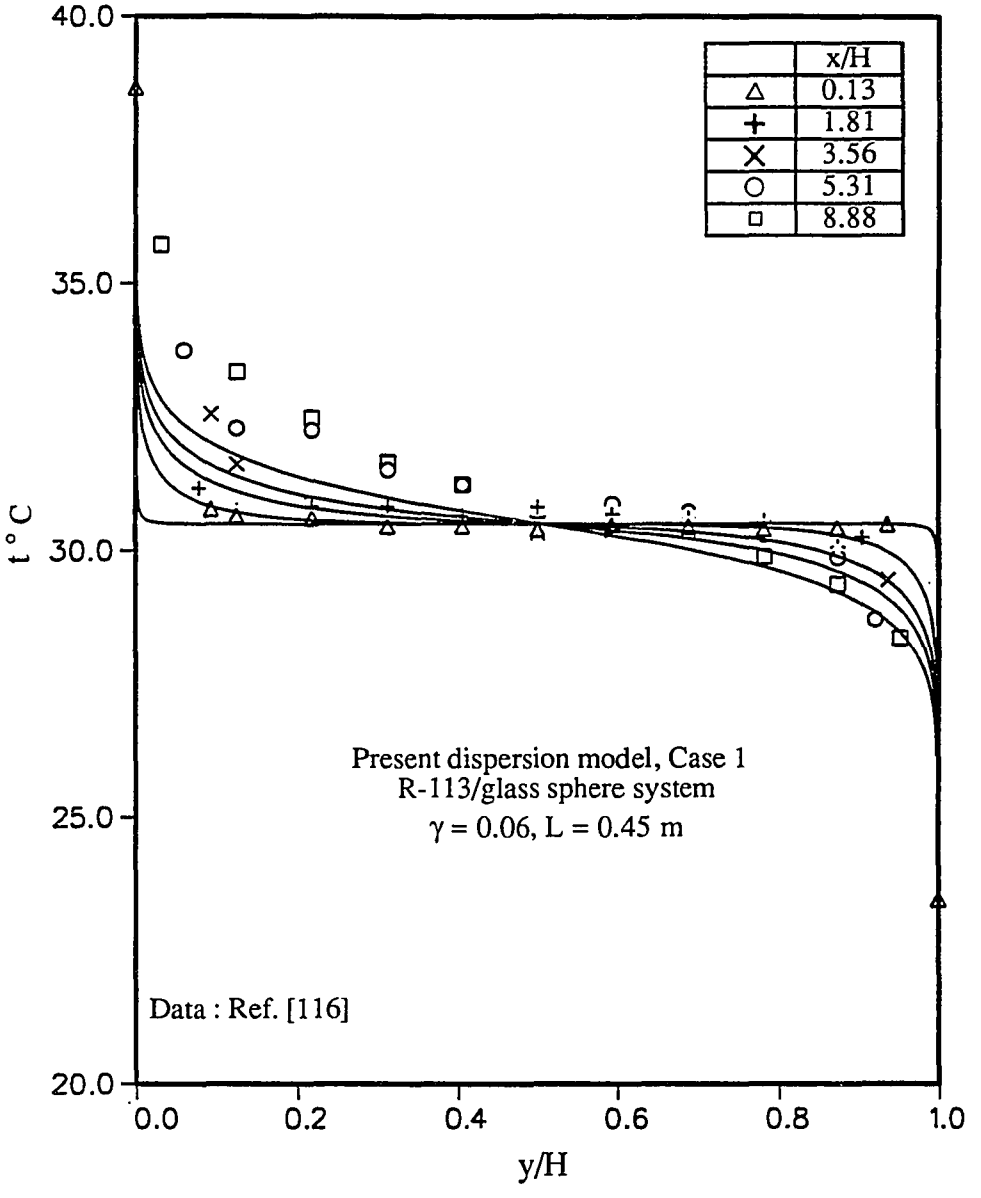

Figure 51. Comparison of the computed temperature distribution and Cai's data for forced convection in a packed channel at $Re_H = 16685$

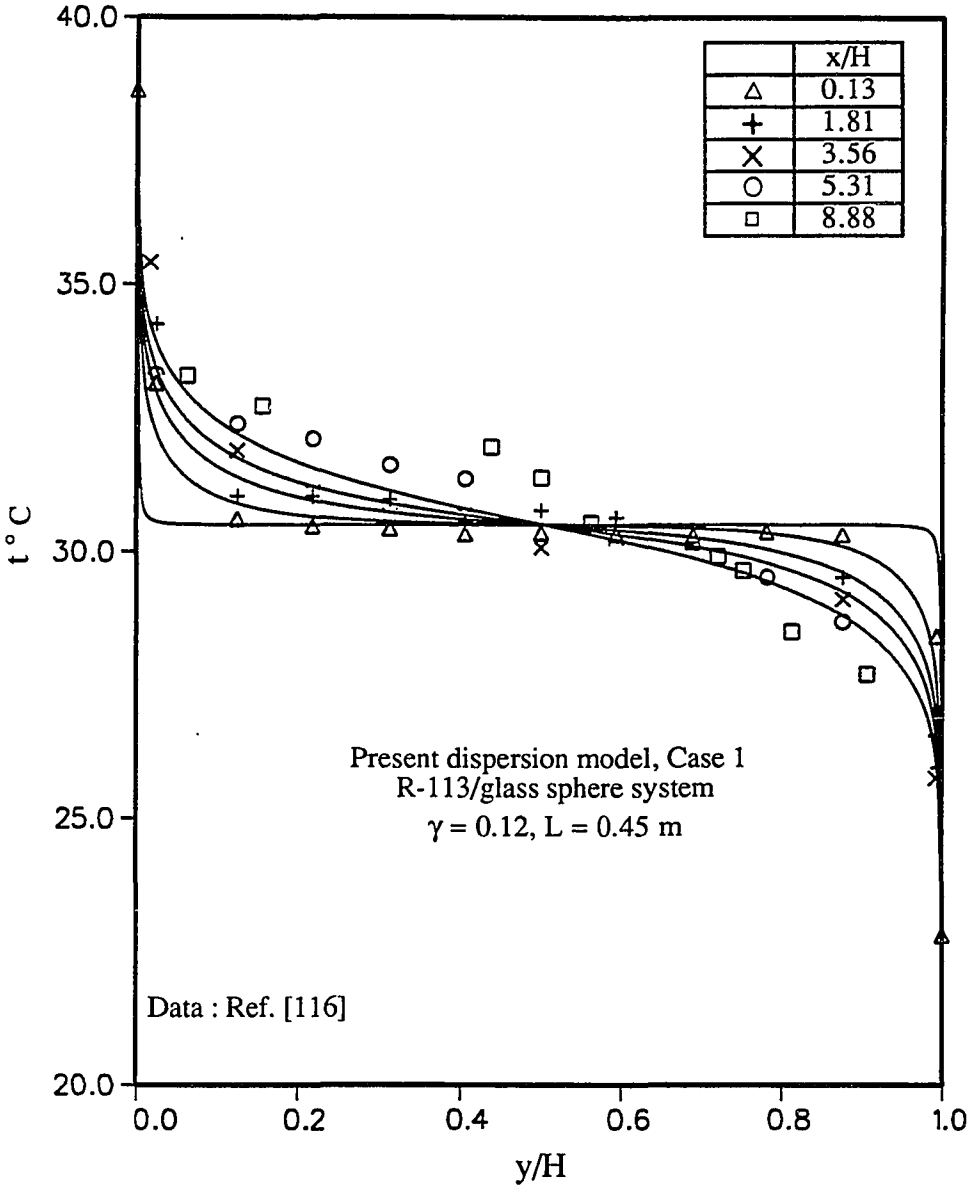

Figure 52. Comparison of the computed temperature distribution and Cai's data for forced convection in a packed channel at $Re_H = 2407$

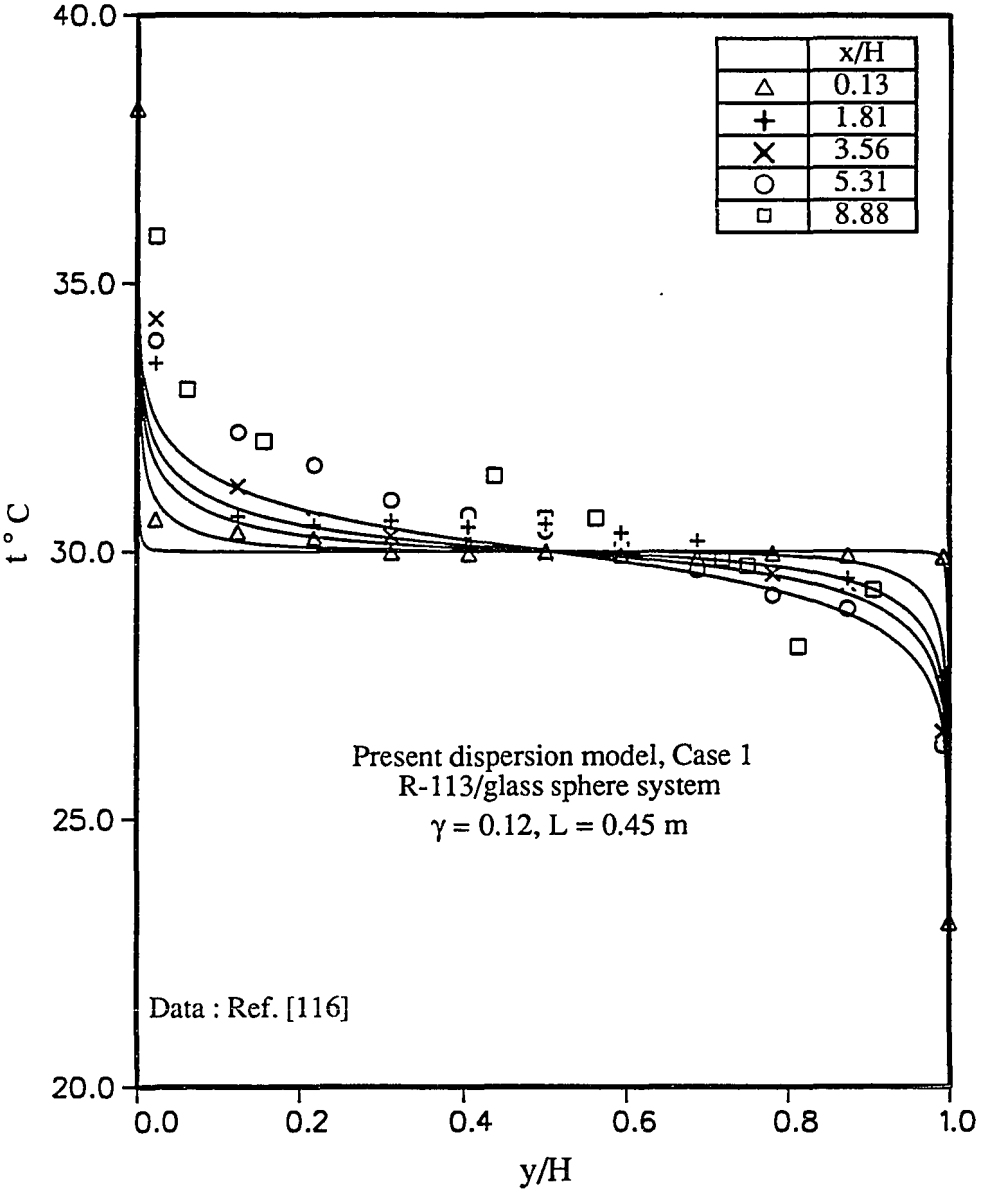

Figure 53. Comparison of the computed temperature distribution and Cai's data for forced convection in a packed channel at $Re_H = 8228$

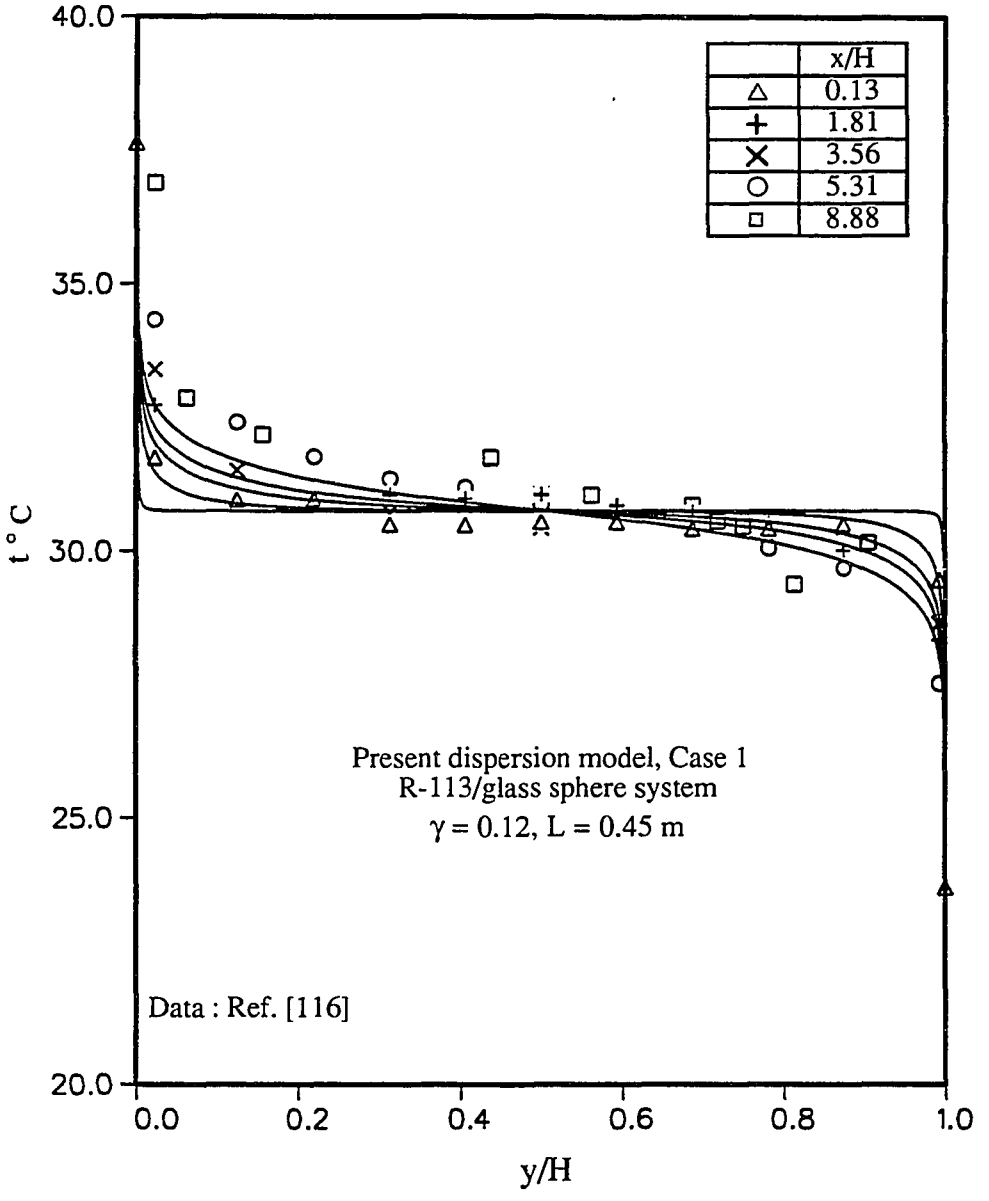

Figure 54. Comparison of the computed temperature distribution and Cai's data for forced convection in a packed channel at $Re_H = 16613$

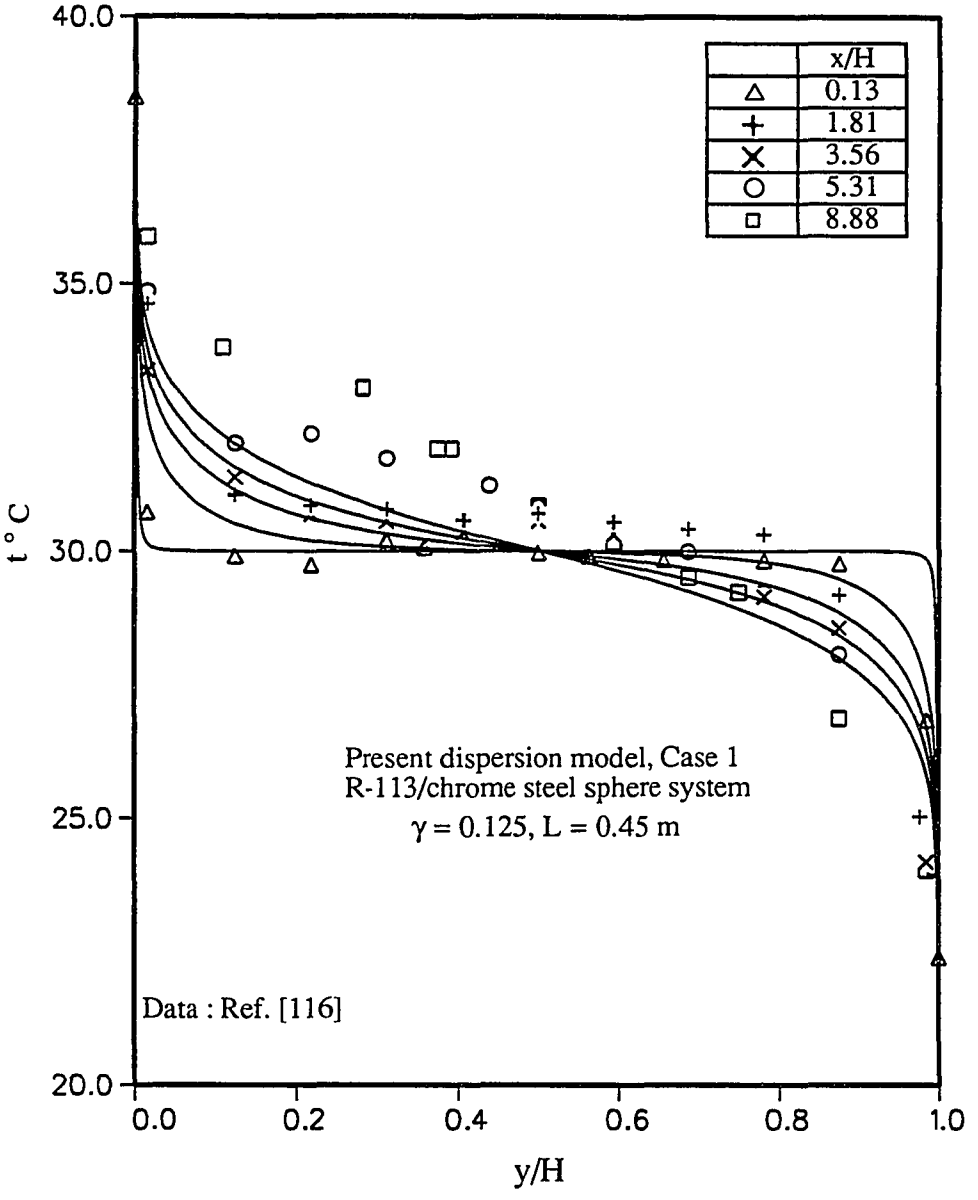

Figure 55. Comparison of the computed temperature distribution and Cai's data for forced convection in a packed channel at $Re_H = 2148$

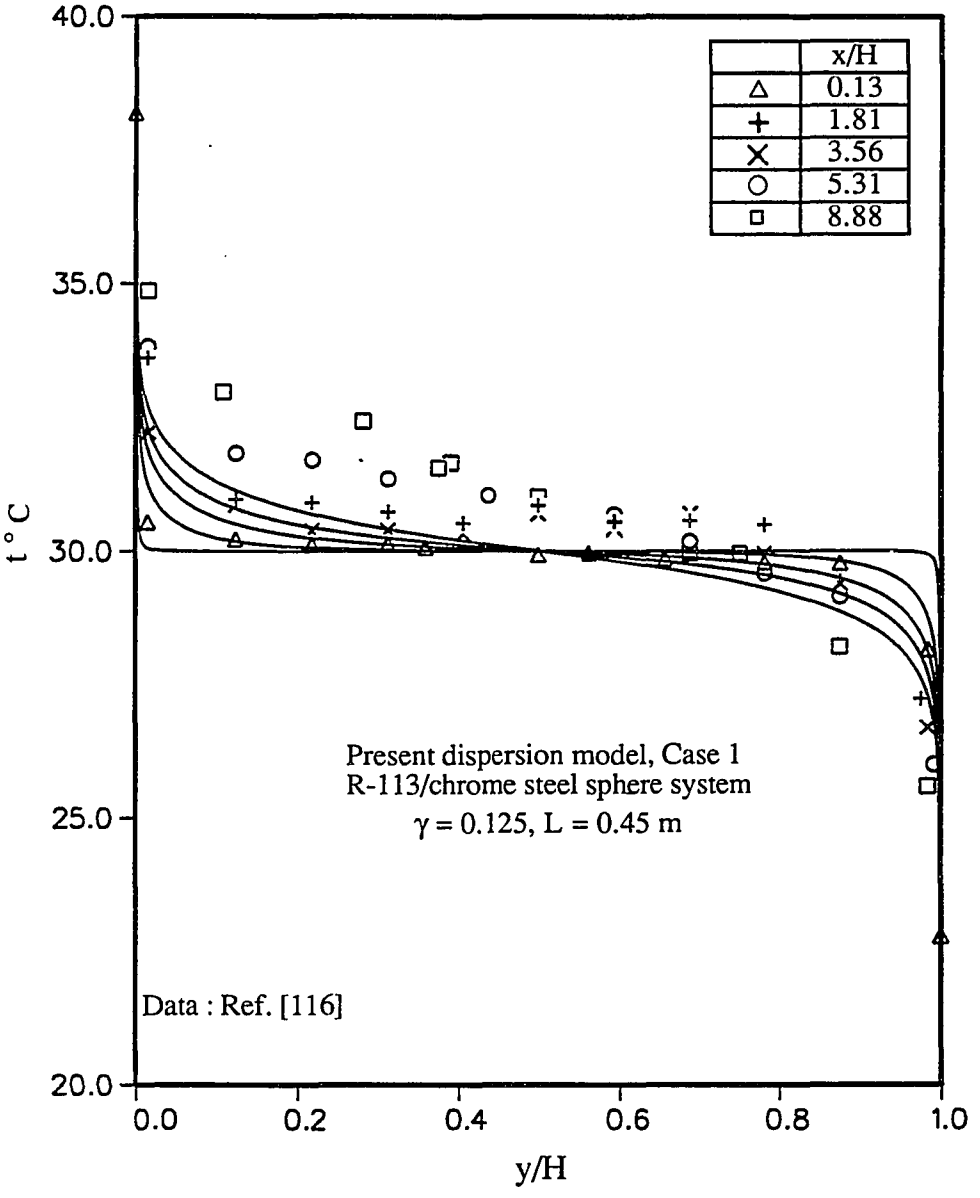

Figure 56. Comparison of the computed temperature distribution and Cai's data for forced convection in a packed channel at $Re_H = 8301$

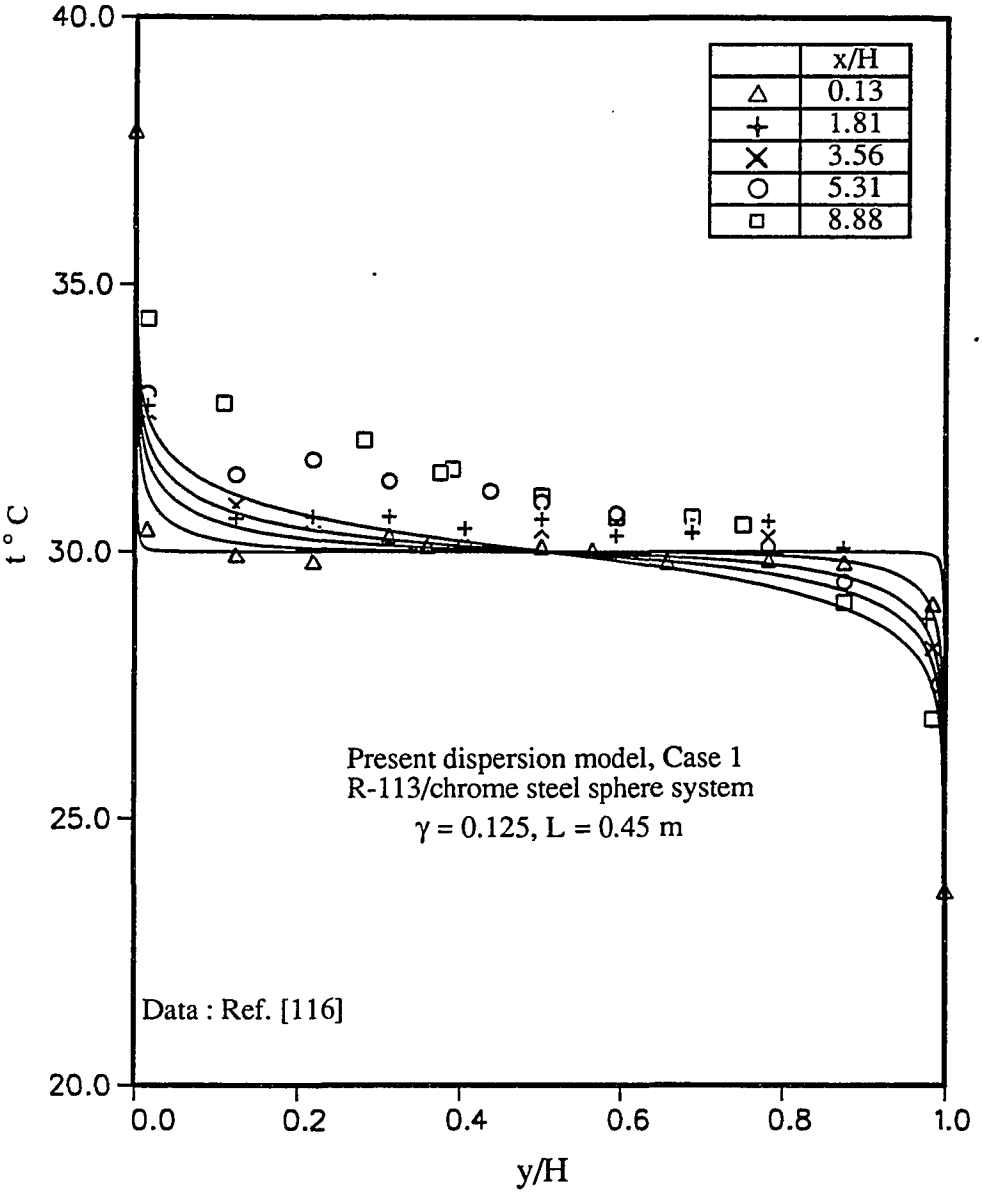

Figure 57. Comparison of the computed temperature distribution and Cai's data for forced convection in a packed channel at $Re_H = 16571$

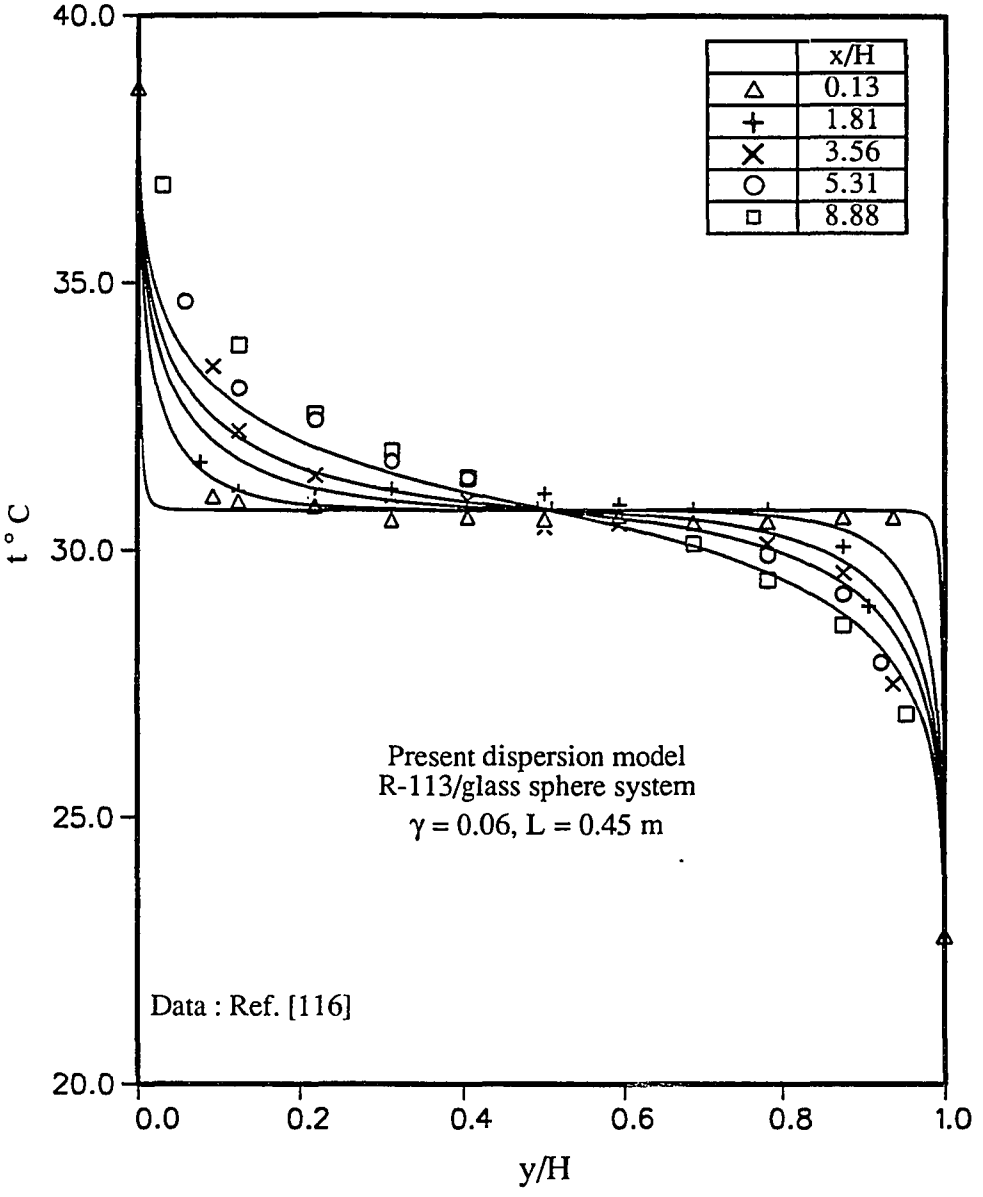

Figure 58. Effect of porosity function (Case 2) on the temperature distribution for forced convection in a packed channel at $Re_H = 4161$

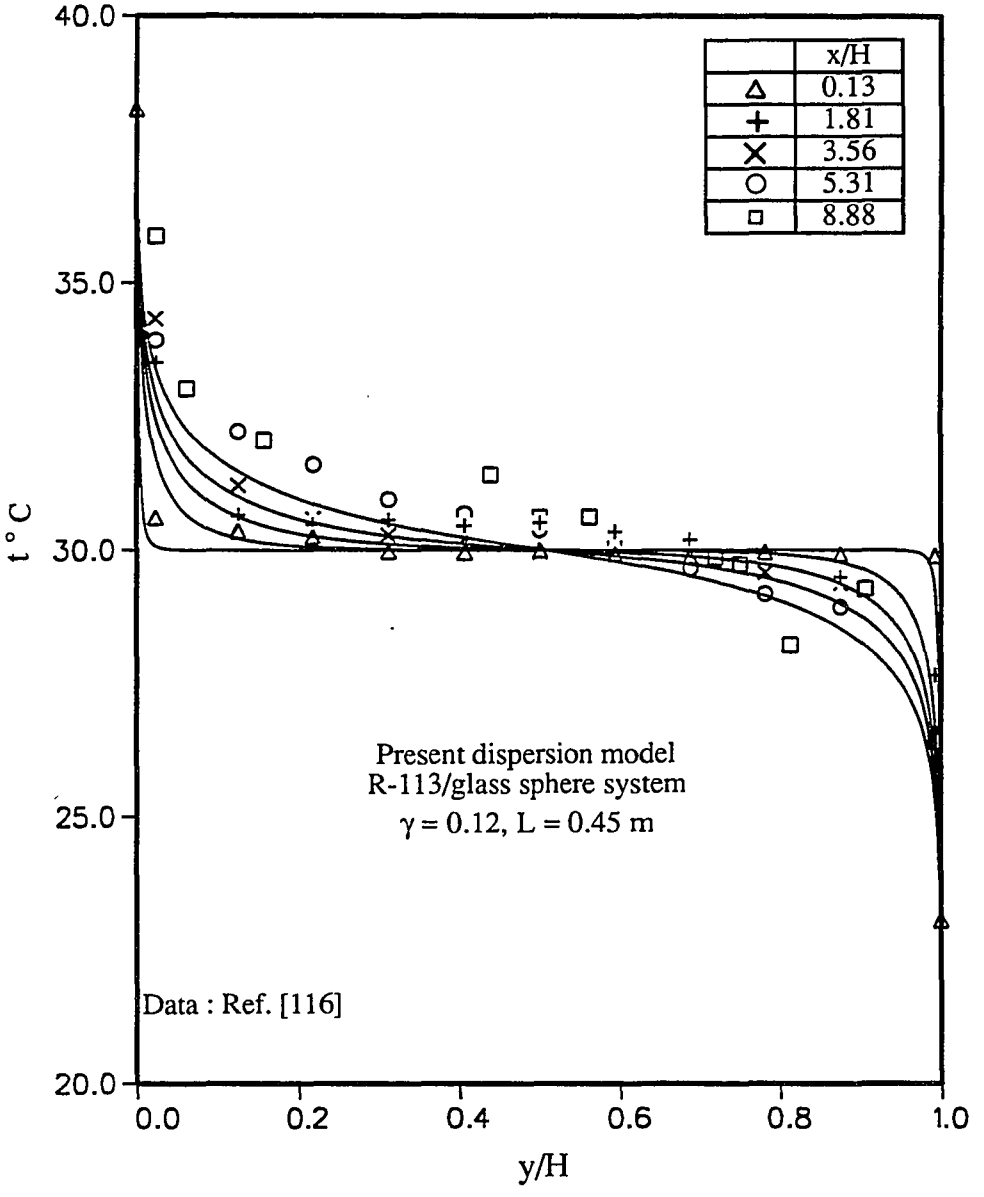

Figure 59. Effect of porosity function (Case 2) on the temperature distribution for forced convection in a packed channel at $Re_H = 8228$

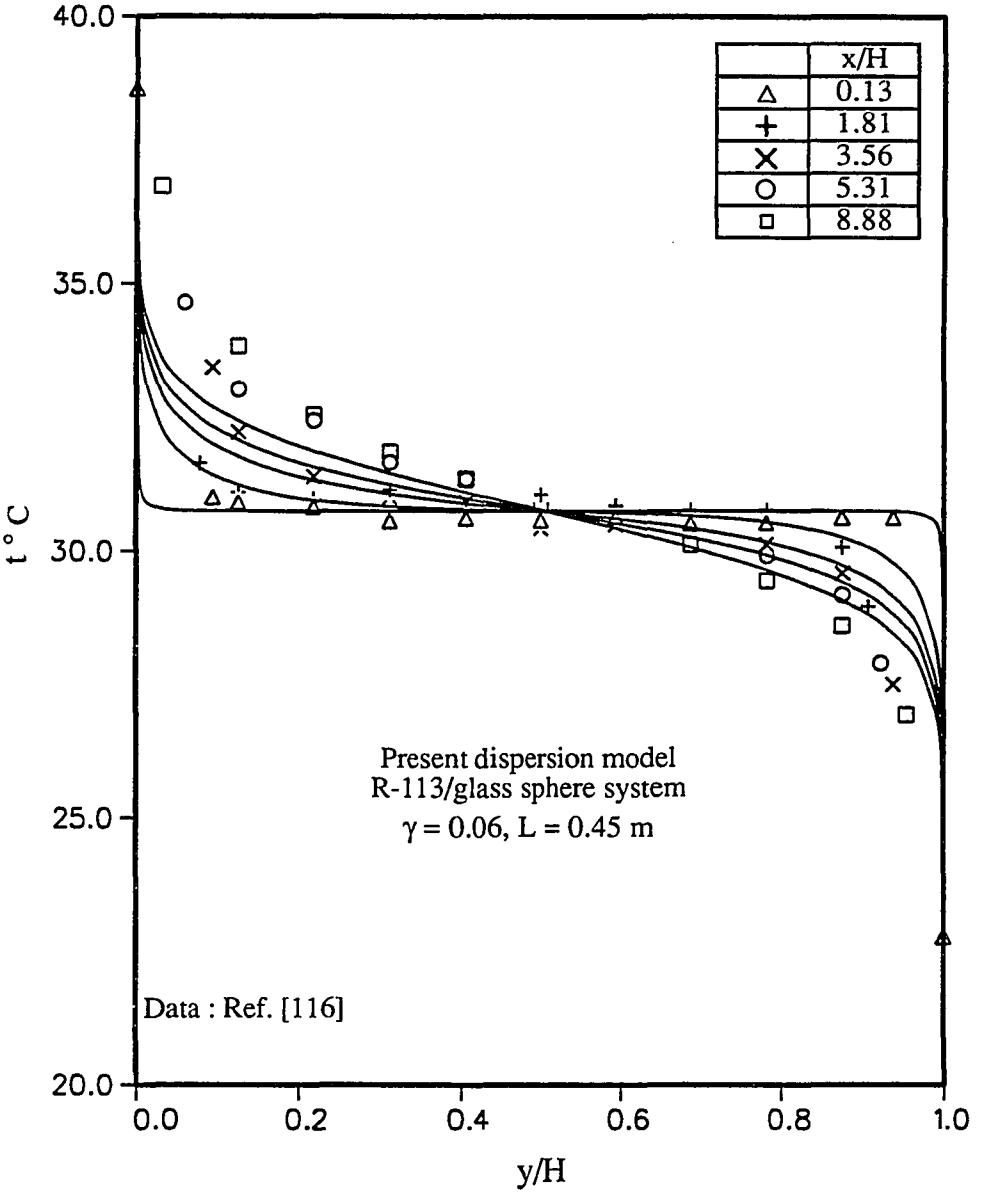

Figure 60. Effect of porosity function (Case 3) on the temperature distribution for forced convection in a packed channel at $Re_H = 4161$

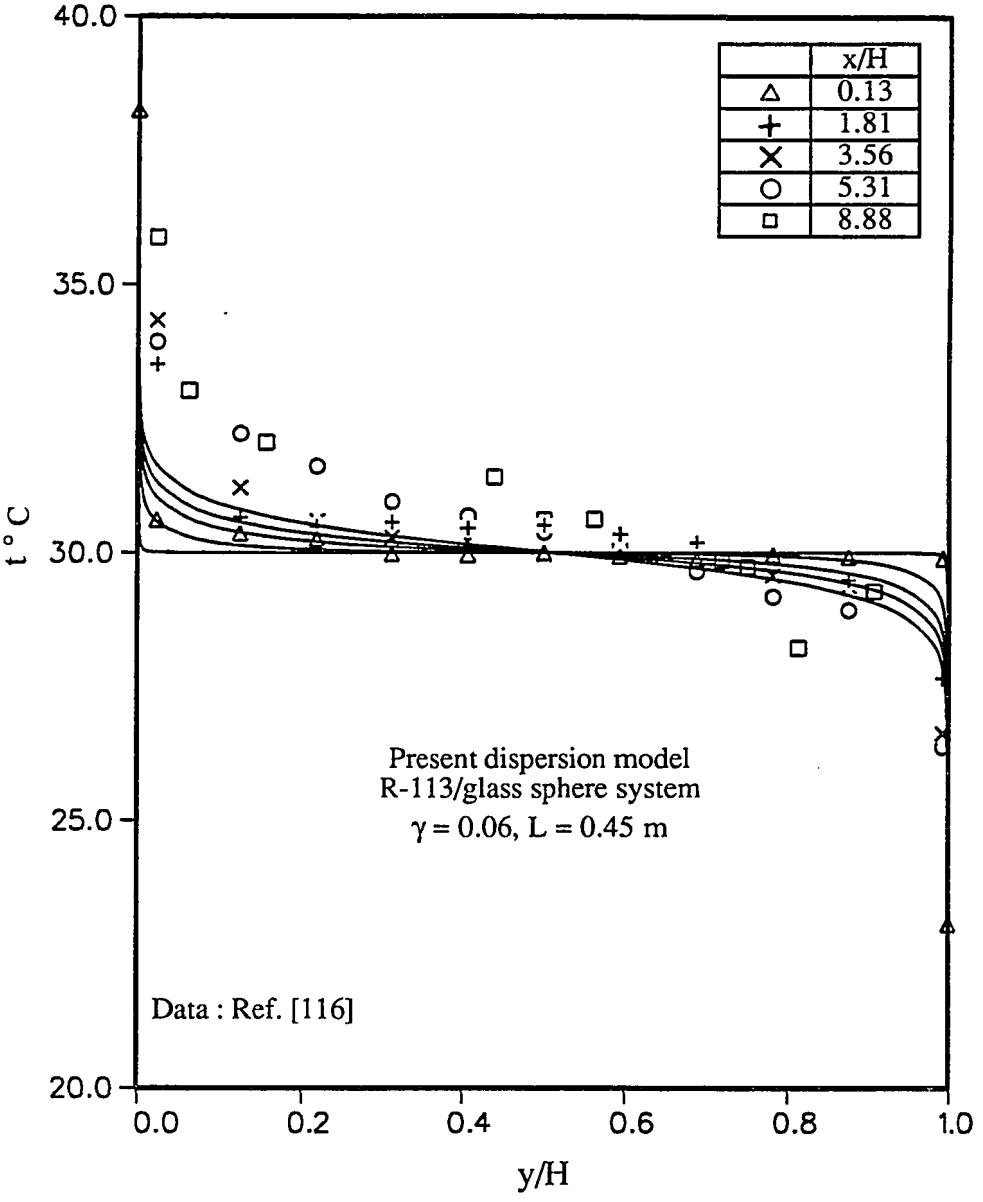

Figure 61. Effect of porosity function (Case 3) on the temperature distribution for forced convection in a packed channel at $Re_H = 8228$

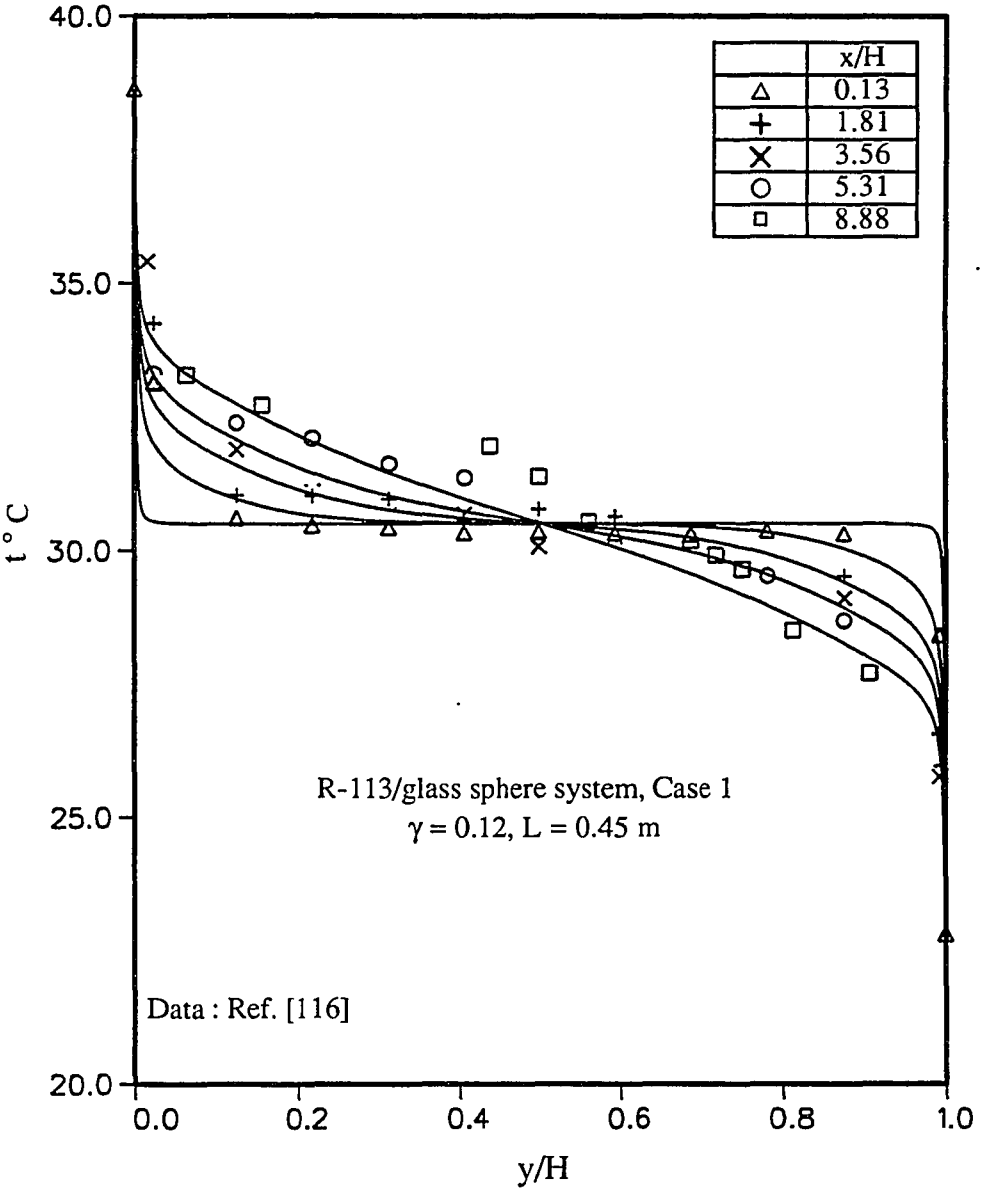

Figure 62. Temperature distribution for forced convection in a packed channel based on Kuo & Tien's dispersion model (Re_H = 2407)

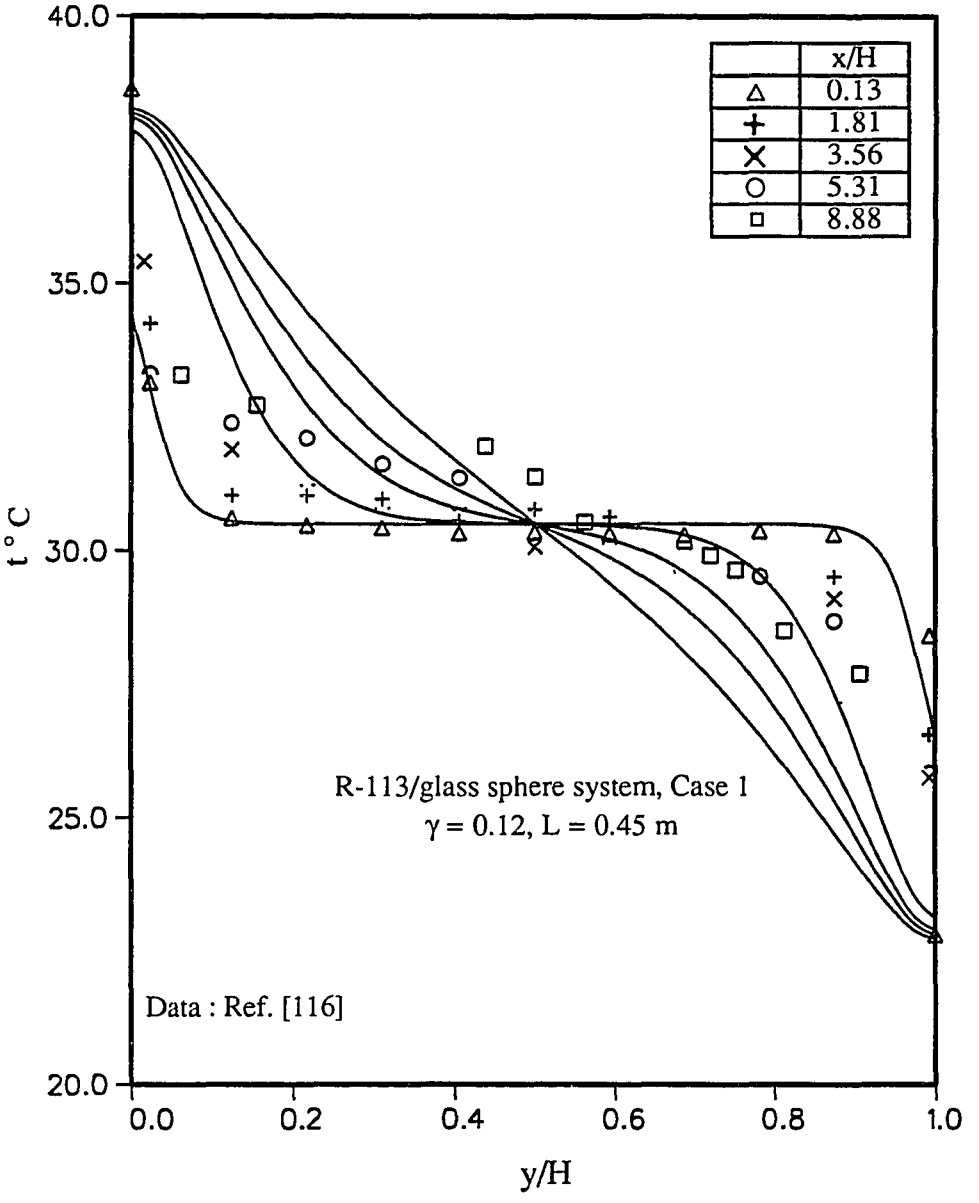

Figure 63. Temperature distribution for forced convection in a packed channel based on Koch & Brady's dispersion model ($Re_H = 2407$)

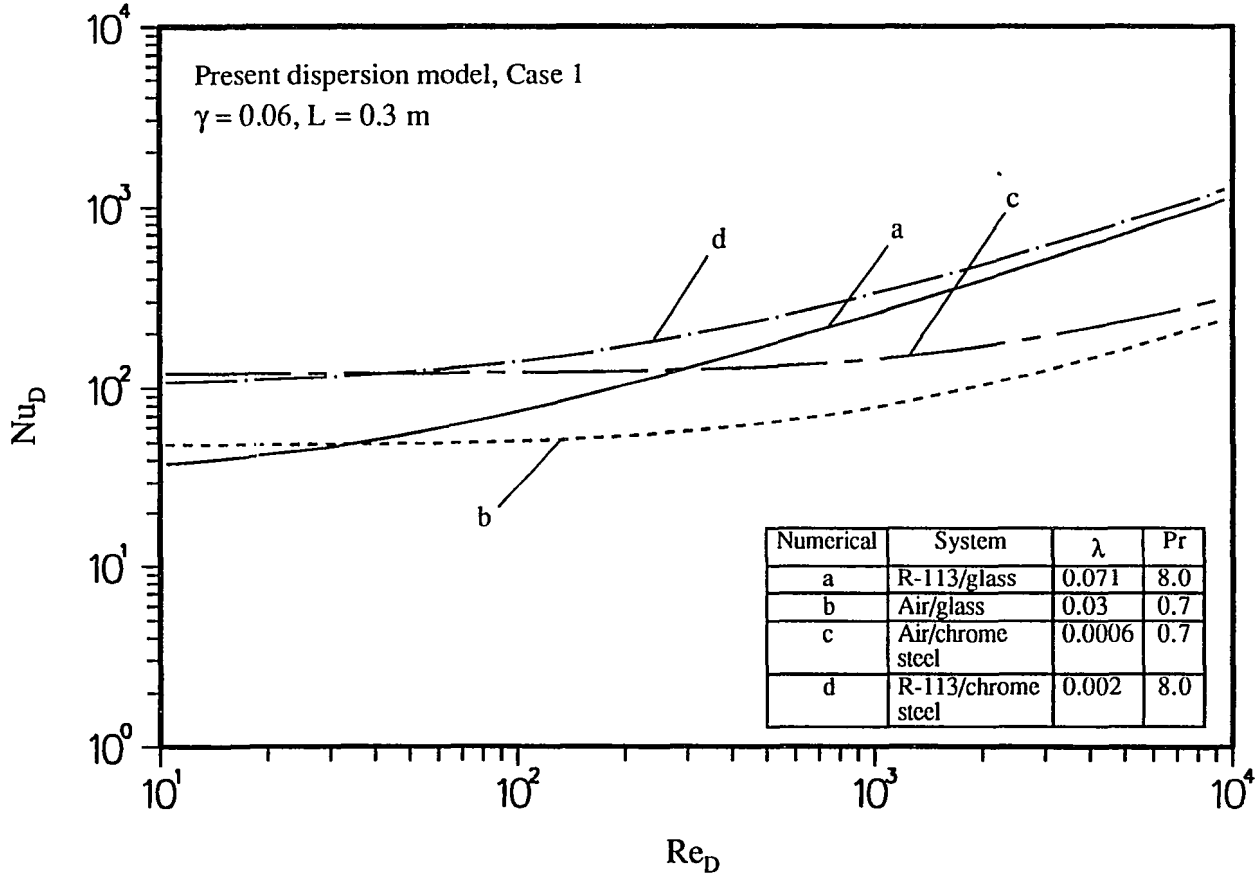

Figure 64. Effects of Pr and λ on the average Nusselt number for forced convection in a packed tube

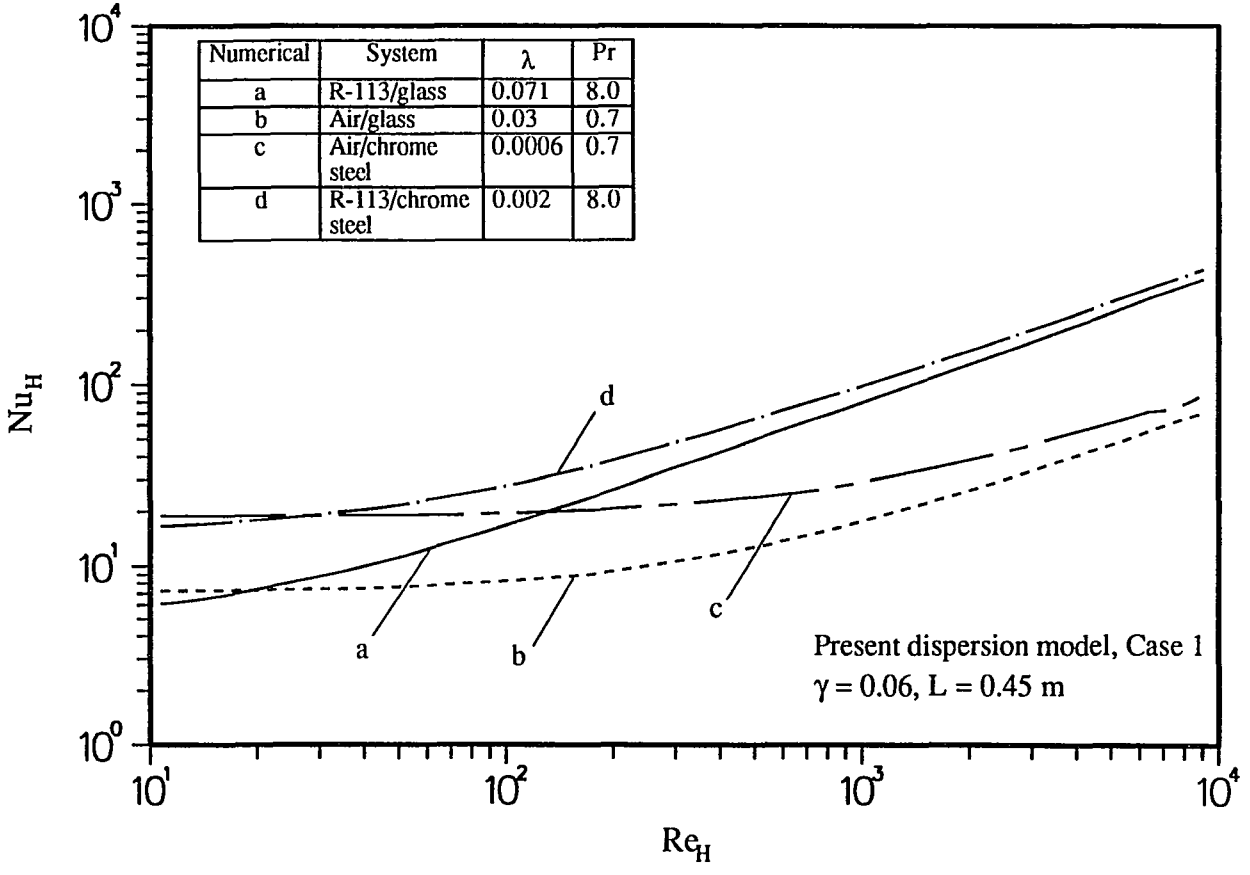

Figure 65. Effects of Pr and λ on the average Nusselt number for forced convection in a packed channel

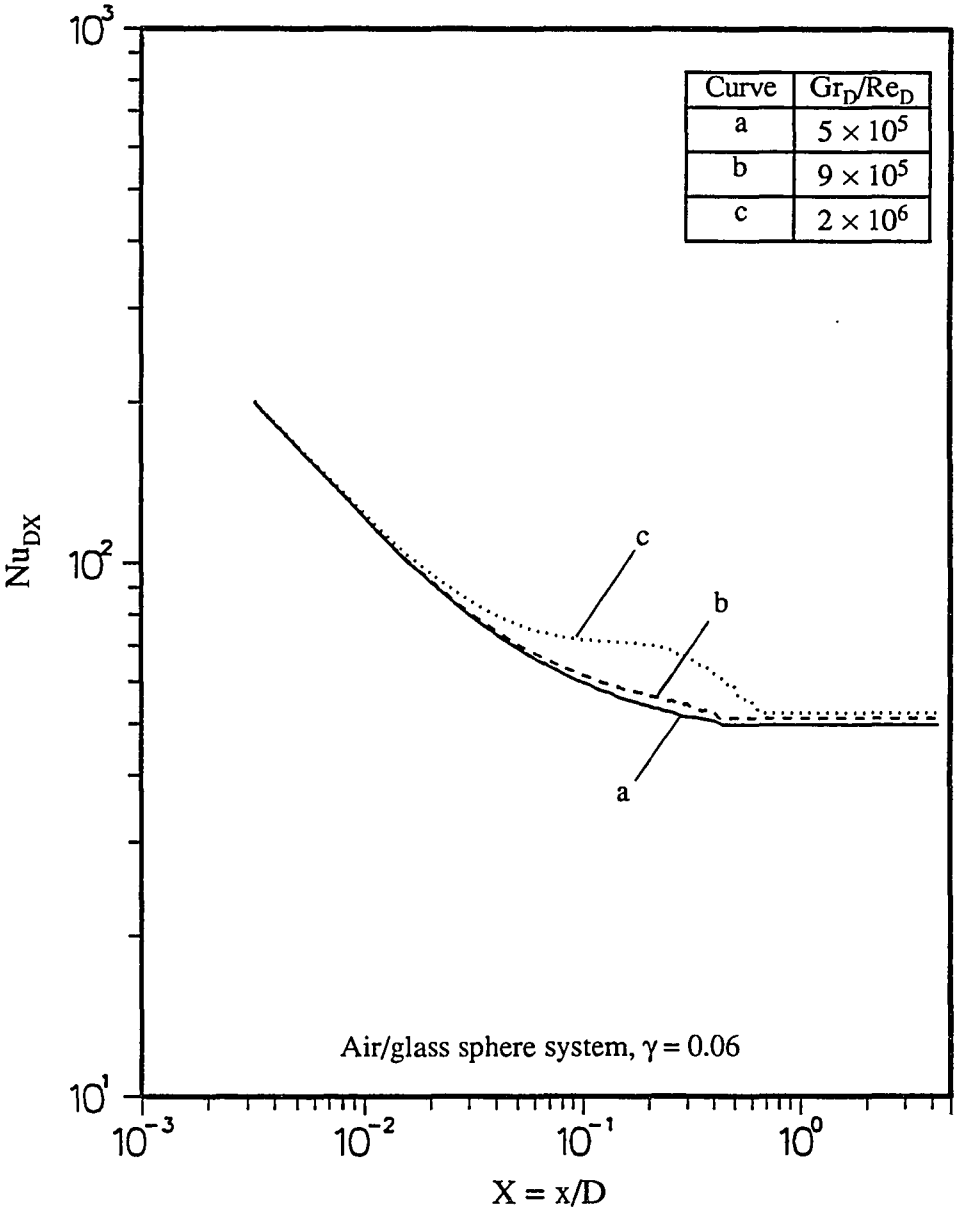

Figure 66. Effect of Gr_D/Re_D on the local Nusselt number for mixed convection in a packed tube

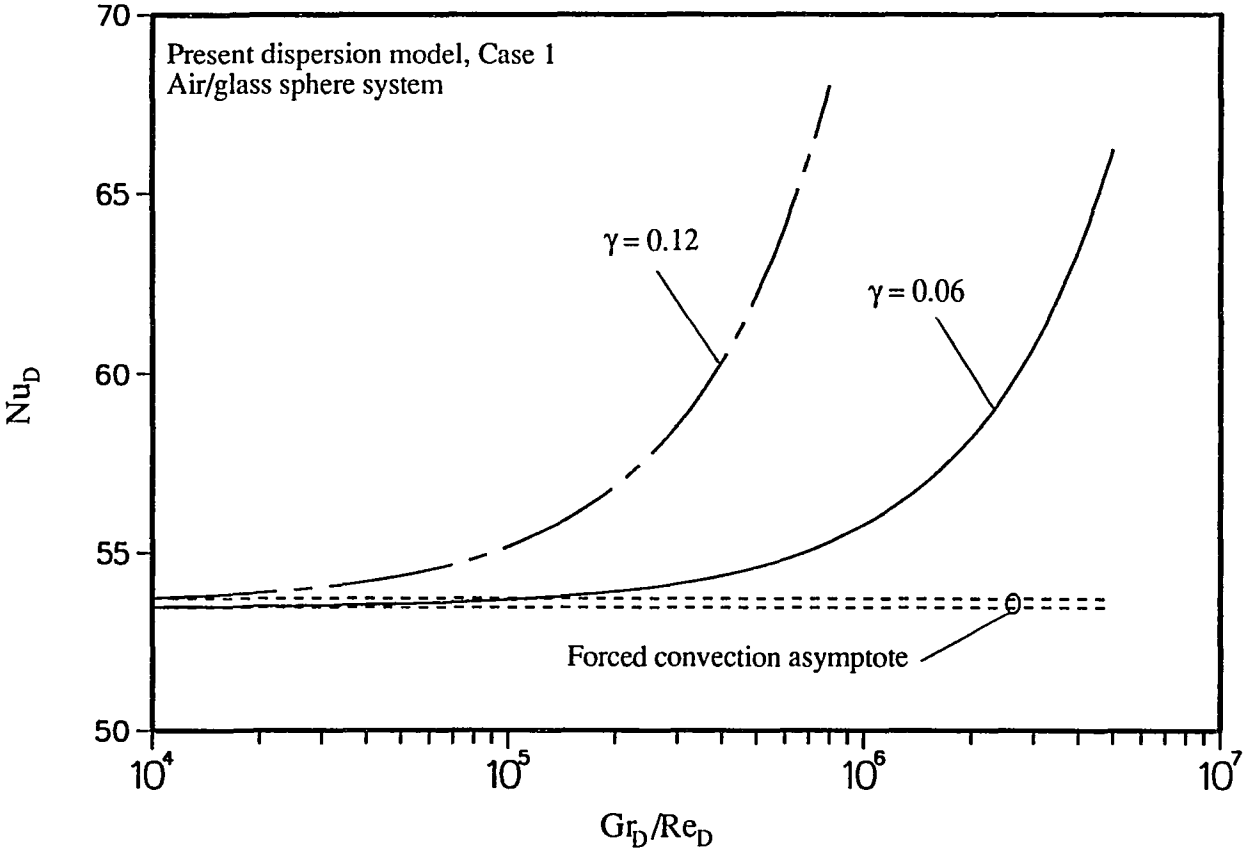

Figure 67. Variation of average Nusselt number for mixed convection in a packed tube

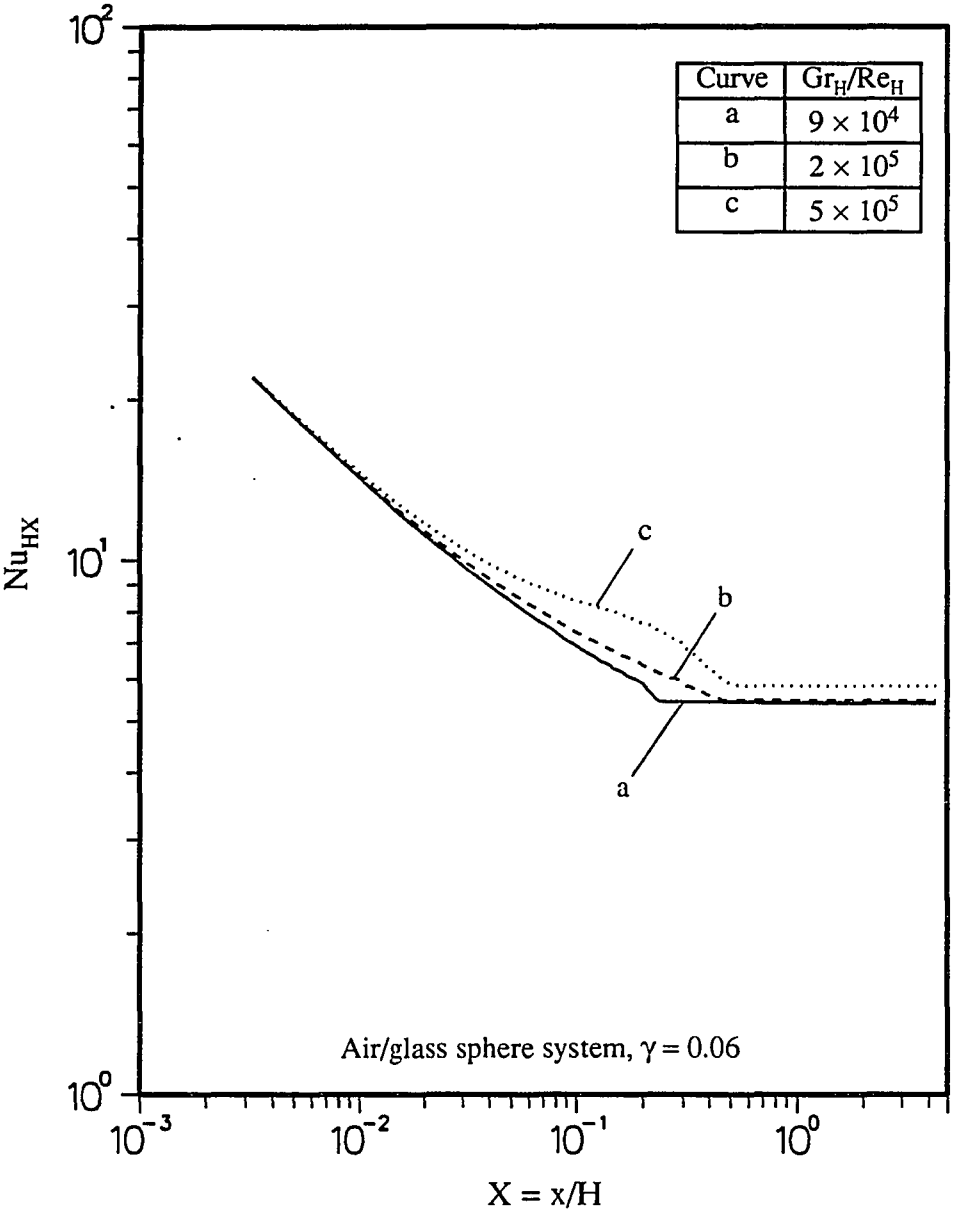

Figure 68. Effect of Gr_H/Re_H on the local Nusselt number for mixed convection in a packed channel

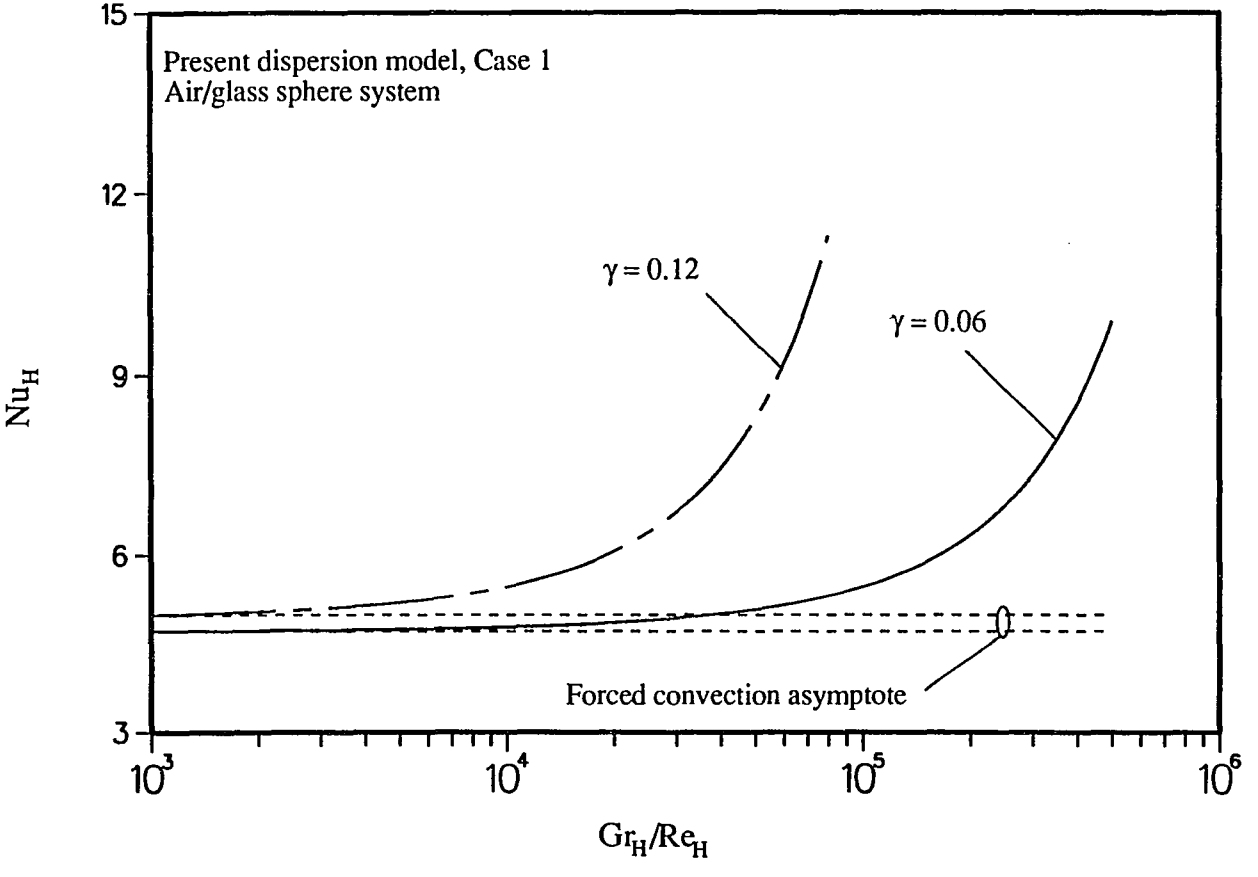

Figure 69. Variation of average Nusselt number for mixed convection in a packed channel

REFERENCES

1. D. A. Plautz and H. F. Johnstone, Heat and mass transfer in packed beds, *A.I.Ch.E. Jl.* **1**, 193-199 (1955).
2. K. J. Schroder, U. Renz and K. Elgeti, Forschungsberichte des Landes Nordrhein-Westfalen, Nr. 3037 (1981).
3. H. Martin, Low Peclet number particle-to-fluid heat and mass transfer in packed beds, *Chem. Engng. Sci.* **33**, 913-919 (1978).
4. P. Cheng and W. J. Minkowycz, Free convection about a vertical flat plate embedded in a porous medium with application to heat transfer from a dike, *J. Geoph. Res.* **82**, 2040-2044 (1977).
5. C. E. Schwartz and J. M. Smith, Flow distribution in packed beds, *Ind. Engng. Chem.* **45**, 1209-1218 (1953).
6. W. W. Schertz and K. B. Bischoff, Thermal and material transport in non-isothermal packed beds, *A.I.Ch.E. Jl.* **15**, 597-604 (1969).
7. R. F. Benenati and C. B. Brosilow, Void fraction distribution in packed beds, *A.I.Ch.E. Jl.* **8**, 359-361 (1962).
8. P. Cheng and D. Vortmeyer, Transverse thermal dispersion and wall channeling in a packed bed with forced convective flow, *Chem. Engng. Sci.* **43**, 2523-2532 (1988).
9. P. Cheng and C. T. Hsu, Fully-developed forced convective flow through an annular packed-sphere bed with wall effects, *Int. J. Heat Mass Transfer* **29**, 1843-1853 (1986).

10. P. Cheng and C. T. Hsu, Application of Van Driest's mixing length theory to transverse thermal dispersion in forced convective flow through a packed bed, *Int. Commun. Heat Mass Transfer* **13**, 613-625 (1986).

11. P. Cheng and W. Zhu, Effects of radial thermal dispersion on fully-developed forced convection in cylindrical packed tubes, *Int. J. Heat Mass Transfer* **30**, 2373-2383 (1987).

12. H. C. Brinkman, A calculation of the viscous force extended by a flowing fluid on a dense swarm of particles, *Appl. Scient. Res.* **A1**, 27-34 (1947).

13. K. Vafai and C. L. Tien, Boundary and inertia effects on flow and heat transfer in porous media, *Int. J. Heat Mass Transfer* **24**, 195-203 (1981).

14. K. Vafai, Convective flow and heat transfer in variable-porosity media, *J. Fluid Mech.* **147**, 233-259 (1984).

15. P. Cheng, C. T. Hsu and A. Chowdhury, Forced convection in the entrance region of a packed channel with asymmetric heating, *ASME J. Heat Transfer* **110**, 946-954 (1988).

16. A. Chowdhury and P. Cheng, Thermally developing flows in packed tubes and channels, *Proc. of the Int. Conf. on Mechanics of Two-Phase Flows*, 421-427 (1989).

17. H. Verschoor and G. C. A. Schuit, Heat transfer to fluids flowing through a bed of granular solids, *Appl. Scient. Res.* **A2**, 97-119 (1952).

18. P. H. Forchheimer, *Z. Ver. Dtsch. Ing.* **45**, 1782-1788 (1901).

19. D. Vortmeyer and J. Schuster, Evaluation of steady flow profiles in rectangular and circular packed beds, *Chem. Engng. Sci.* **38**, 1691-1699 (1983).

20. B. C. Chandrasekhara and D. Vortmeyer, Flow model for velocity distribution in fixed porous beds under isothermal conditions, *Warme-und Stoffubertrangung* **12**, 105-111 (1979).

21. K. Vafai, R. L. Alkire and C. L. Tien, An experimental investigation of heat transfer in variable porosity media, *ASME J. Heat Transfer* **107**, 642-647 (1985).

22. M. L. Hunt and C. L. Tien, Non-Darcian convection in cylindrical packed beds, *Proc. 2nd ASME/JSME Thermal Engng. Joint Conf.*, Vol. 2, 433-438 (1987).

23. S. Ergun, Fluid flow through packed columns, *Chem. Engng. Prog.* **48**, 89-94 (1952).

24. R. M. Fand, B. Y. K. Kim, A. C. C. Lam and R. T. J. Phan, Resistance to flow of fluids through simple and complex porous media whose matrices are composed of randomly packed spheres, *ASME J. Fluids Engng.* **109**, 268-274 (1987).

25. R. M. Fand and R. Thinakaran, The influence of the wall on flow through pipes packed with spheres, *ASME J. Fluids Engng.* **112**, 84-88 (1990).

26. G. Lauriat and V. Prasad, Natural convection in a vertical porous cavity : A numerical study for Brinkman-extended Darcy formulation, *ASME J. Heat Transfer* **109**, 688-696 (1987).

27. S. V. Patankar, *Numerical heat transfer and fluid flow*, McGraw-Hill, Washington D. C. (1980).

28. P. Zehner and E. U. Schluender, Waermeleitfahigkeit von schuettungen bei massigen temperaturen, *Chemie-Ingr-Tech* **42**, 933-941 (1970).

29. P. Cheng, Wall effects on fluid flow and heat transfer in porous media, *Proc. 2nd ASME/JSME Thermal Engng. Joint Conf.* **2**, 297-303 (1987).

30. Wang and Longwell, Laminar flow in the inlet section of parallel plates, *A.I.Ch.E. Jl.* **10**, 323-329 (1964).

31. J. Beck, Design of packed catalytic reactors, *Adv. Chem. Engng.* **3**, 203-270 (1962).

32. A. P. Colburn, Heat transfer and pressure drop in empty, baffled and packed tubes, *Ind. Engng. Chem.* **23**, 910-923 (1931).

33. G. M. Chrysler and R. E. Simons, An experimental investigation of the forced convection heat transfer characteristics of Fluorocarbon liquid flowing through a packed-bed for immersion cooling of microelectronic heat source, *ASME Symp. HTD* **131**, 21-27 (1990).

34. R. E. Simons, K. P. Moran, V. W. Antonetti and R. C. Chu, *Proc. Natl. Elect. Packaging and Prod. Conf. (NEPCON)* , (1982).

35. T. Mizuno, M. Okano, Y. Matsue and T. Watari, *Proc. Int. Symp. on Cooling Tech. for Elect. Equip.*, 110-125 (1987).

36. N. Yamamoto, Y. Udagawa and M. Suzuki, Cooling system for FACOM M-780 large scale computers, *Proc. Int. Symp. on Cooling Tech. for Elect. Equip.*, 96-109 (1987).

37. R. C. Chu and U. P. Hwang, Dielectric fluidized cooling system, *IBM Technical Disclosure Bulletin* **20**, No. 2, 678-679 (1977).

38. G. F. Froment and K. B. Bischoff, *Chemical reactor analysis design*, John Wiley and Sons, New York (1979).

39. N. Wakao and S. Kaguei, *Heat and mass transfer in packed beds*, Gordon and Breach Science Pub., New York (1982).

40. G. P. Willhithnam, H. E. Hodlscher and G. S. Laddha, Effective thermal conductivities in packed beds, *AIChE J.* **7**, 249 (1960).

41. P. Cheng, Heat transfer in Geothermal systems, *Advances in Heat Transfer* **14**, 1-105 (1978).

42. W. Reichelt, Zur Berechmeng des Druckverlustes emphasig durchstromter Kuger-ung Zyhnderschuthungen, *Chemie. Ing. Tech.* **44** (1972).

43. K. Vafai and C. L. Tien, Boundary and inertia effects on convective mass transfer in porous media , *Int. J. Heat Mass Transfer* **25**, 1183-1190 (1982).

44. Y. Cohen and A. B. Metzner, Wall effects in laminar flow of fluids through packed beds, *AIChE J.* **27**, 705-715 (1981).

45. C. T. Hsu and P. Cheng, Thermal dispersion in a porous medium, *Int. J. Heat Mass Transfer* **33**, 1587-1597 (1990).

46. M. A. Combarnous and S. A. Bories, Hydrothermal convection in saturated porous media, *Advances in Hydroscience* **10**, 231-307 (1975).

47. I. Catton, Natural convection in porous media, *Natural convection : Fundamentals and applications*, Hemisphere, New York (1985).

48. P. J. Burns, C. C. Chow and C. L. Tien, Convection in a vertical slot filled with porous insulation, *Int. J. Heat Mass Transfer* **20**, 919-926 (1977).

49. A. Hadim and L. C. Burmeister, Onset of convection in a porous medium with internal heat generation and downward flow, *A.I.A.A. Jl. Thermophysics Heat Transfer* (in press).

50. D. Poulikakos and K. J. Renken, Forced convection in a channel filled with porous medium, including the effects of flow inertia, variable porosity and Brinkman friction, *ASME J. Heat Transfer* **109**, 880-888 (1987).

51. K. J. Renken and D. Poulikakos, Experiments on forced convection from a horizontal heated plate in a packed bed of glass spheres, *ASME J. Heat Transfer* **111**, 59-65 (1989).

52. M. Leva, Heat transfer to gases through packed tubes : general correlation for smooth spherical particles, *Ind. Engng. Chem.* **39**, 857-862 (1947).

53. M. Leva and M. Grummer, Heat transfer to gases through packed tubes : effect of particle characteristics, *Ind. Engng. Chem.* **40**, 415-419 (1948).

54. R. E. Hall and J. M. Smith, Design of gas-solid catalytic reactors, *Chem. Engng. Prog.* **45**, 459-470 (1949).

55. D. G. Bunell, H. B. Irvin, R. W. Olson and J. M. Smith, Effective thermal conductivity in gas-solid systems, *Ind. Engng. Chem.* **41**, 1977-1981 (1949).

56. C. A. Coberly and W. R. Marshall Jr., Temperature gradients in gas streams flowing through fixed granular beds, *Chem. Engng. Prog.* **47**, 141-150 (1951).

57. W. Brotz, Untersuchungen uber warmeleitung, stofftransport und druckabfall indurchstromten schuttgutern, *Chem. Ing. Technik* **23**, 408-416 (1951).

58. M. E. Aerov and N. N. Umnik, Coefficient of thermal conductivity in a granular stratum, *J. Tech. Physics (USSR)* **21**, 1364 (1951).

59. J. M. Campbell and R. L. Huntington, Heat transfer and pressure drop in fixed beds of spherical and cylindrical solids, *Petrol. Ref.* **31**, 123 (1952).

60. T. J. Hanrattry, Nature of wall heat transfer coefficient in packed beds, *Chem. Engng. Sci.* **5**, 209-214 (1954).

61. J. H. Quinton and J. A. Storrow, Heat transfer to air flowing through packed tubes, *Chem. Engng. Sci.* **5**, 245-257 (1956).

62. S. S. Kwong and J. M. Smith, Radial heat transfer in packed beds, *Ind. Engng. Chem.* **49**, 849-903 (1957).

63. S. Yagi and D. A. Kunii, Studies on effective thermal conductivities in packed beds, *A.I.Ch.E. Jl.* **3**, 373-379 (1957).

64. D. Thoenes Jr. and H. Kramers, Thermal conductivity of packed sphere systems,*Chem. Engng. Sci.* **8**, 271 (1958).

65. S. Yagi and N. Wakao, Heat and mass transfer from wall to fluid in packed beds, *A.I.Ch.E. Jl.* **5**, 79-85 (1959).

66. S. Yagi, D. Kunii and N. Wakao, Radially effective thermal conductivities in packed beds, *Int. Dev. Heat Transfer*, Part iv, 742-749 (1961).

67. S. Yagi, D. Kunii and K. Endo, Heat transfer in packed beds through which water is flowing, *Int. J. Heat Mass Transfer* **7**, 333-339 (1964).

68. J. J. Gelperin and A. M. Kagan, Study of heat transfer in gas flow in tubes packed with granular materials, *A.R.C.H.E. Symp. Series*, 308-321 (1966).

69. D. Kunii, M. Suzuki and N. Ono, Heat transfer from wall surface to packed beds at high Reynolds number, *J. Chem. Engng. of Japan* **1**, 21-26 (1968).

70. R. D. Hawthorn, G. H. Ackerman and A. C. Nixon, A mathematical model of a packed-bed heat exchanger reactor for dehydrogenation of methylcyclohexane : comparison of predictions with experimental results, *A.I.Ch.E. Jl.* **14**, 69-76 (1968).

71. J. M. Valstar, PhD Thesis, Delft, Netherlands (1969).

72. J. B. Agnew and O. E. Potter, Heat transfer properties of packed tubes of small diameter, *Trans. Inst. Chem. Engrs.* **48**, T15-20 (1970).

73. A. P. De Wasch and G. F. Fremont, Heat transfer in packed beds, *Chem. Engng. Sci.* **27**, 567-576 (1972).

74. W. F. Olbrich and O. E. Potter, Heat transfer in small diameter packed beds, *Chem. Engng. Sci.* **27**, 1723-1732 (1972).

75. W. Hennecke and E. U. Schlunder, The wall heat transfer coefficient in packed beds, in *Heat exchangers : Design and theory sourcebook*, Scripta Book Co., Washington (1974).

76. D. J. Gunn and M. Khalid, Thermal dispersion and wall heat transfer in packed beds, *Chem. Engng. Sci.* **30**, 261-267 (1975).

77. A. G. Dixon and W. R. Paterson, Heat transfer in packed beds of low tube/particle diameter ratio, *A.C.S. Symp. Series* **65**, 238-253 (1978).

78. J. D. Gabor, Heat transfer to particle beds with gas flows less than or equal to that required for incipient fluidization, *Chem. Engng. Sci.* **25**, 979-984 (1970).

79. S. Yagi and D. Kunii, Studies on heat transfer near wall surface packed beds, *A.I.Ch.E. Jl.* **6**, 97-104 (1960).

80. R. F. Baddour and C. Y. Yoon, Local radial effective conductivity and wall effect in packed beds, *Chen. Engng. Prog. Symp. Series* **57**, 35-50 (1961).

81. D. Kunii and M. Suzukii, Heat transfer between wall surface and packed solids, *Proc. 3rd Int. Heat Transfer Conf.* **4**, 344-352 (1966).

82. R. E. Chao, R. A. Caban and M. M. Irizarry, Wall heat transfer to chemical reactors, *Canadian J. Chem. Engng.* **51**, 67-70 (1973).

83. W. R. Paterson and J. J. Carberry, Fixed bed catalytic reactor modelling, *Chem. Engng. Sci.* **38**, 175-180 (1977).

84. P. Cheng, Combined free and forced convection flow about inclined surfaces in porous media, *Int. J. Heat Mass Transfer* **20**, 807-814 (1977).

85. P. Cheng, Mixed convection about a horizontal cylinder and a sphere in a fluid saturated porous medium, *Int. J. Heat Mass Transfer* **25**, 1245-1247 (1982).

86. P. Ranganathan and R. Viskanta, Mixed convection boundary layer flow along a vertical surface in a porous medium, *Num. Heat Transfer* **7**, 305-317 (1984).

87. W. J. Minkowycz, P. Cheng and R. N. Hirschberg, Nonsimilar boundary layer analysis of mixed convection about a horizontal heated surface in a fluid-saturated porous medium, *Int. Comm. Heat Mass Transfer* **11**, 127-141 (1984).

88. R. M. Islam and K. Nandakumar, Multiple solutions for buoyancy-induced flow in saturated porous media for large Peclet numbers, *ASME J. Heat Transfer* **108**, 866-871 (1986).

89. M. Haajizadeh and C. L. Tien, Combined natural and forced convection in a horizontal porous channel, *Int. J. Heat Mass Transfer* **27**, 799-813 (1984).

90. M. Kaviany, Laminar flow through a porous channel bounded by isothermal parallel plates, *Int. J. Heat Mass Transfer* **28**, 851-858 (1984).

91. V. Prasad, F. C. Lai and F. A. Kulack, Mixed convection in horizontal porous layers heated from below, *A.S.M.E. Publication 86-HT-16* (1986).

92. D. A. Anderson, *Computational Fluid Mechanics and Heat Transfer*, McGraw-Hill, Washington (1984).

93. D. C. Reda, Mixed convection in a liquid-saturated porous medium, *ASME J. Heat Transfer* **110**, 147-154 (1988).

94. F. C. Lai, V. Prasad and F. A. Kulaki, Aiding and opposing mixed convection in a vertical porous layer with a finite wall heat source, *Int. J. Heat Mass Transfer* (in press).

95. A. Hadim and S. Govindarajan, Development of laminar mixed convection in a vertical porous channel, *Symbolic Computations in Fluid Mechanics and Heat Transfer,* ASME, New York, HTD **105**, 145-153 (1988).

96. C. Beckermann, R. Viskanta and S. Ramadyani, A numerical study of non-Darcian natural convection in a vertical enclosure with a porous medium, *Num. Heat Transfer* **10**, 557-570 (1986).

97. V. Prasad and A. Tuntomo, Inertia effects on natural convection in a vertical porous cavity, *Num. Heat Transfer* **11**, 295-320 (1987).

98. C. T. Hsu and P. Cheng, Closure schemes of the macroscopic energy equation for convective heat transfer in porous media, *Int. Commun. Heat Mass Transfer*, **15**, 689-703 (1988).

99. K. Vafai, Analysis of the channeling effect in variable porosity media, *J. Energy Resources Tech.* **108**, 131-139 (1986).

100. T. Cebeci and P. Bradshaw, *Physical and computational aspect of convective heat transfer*, Springer-Vertag, New York (1984).

101. H. B. Keller, *A new difference scheme for parabolic problems in numerical solutions of partial differential equations,* J Bramble, ed., Academic Press, New York (1970).

102. M. Kaviany, Boundary layer treatment of forced convection heat transfer from a semi-infinite flat plate embedded in porous media, *ASME J. Heat Transfer* **109**, 345-349 (1987).

103. J. Bear, Modelling Transport Phenomena in Porous Media, *NATO ASI Proceedings on Convective Heat and Mass Transfer in Porous Media*, 1-65 (1990).

104. F. C. Lai, F. A. Kulacki and V. Prasad, Mixed convection in horizontal porous layers : Effect of thermal boundary conditions, paper presented at the *ASME Winter Annual Meeting*, Boston (1987).

105. S. Yagi and D. Kunii, Studies of heat transfer near wall surface in packed beds, *A.I.Ch.E. Jl.* **6**, 97-104 (1960).

106. I. F. Macdonald, M. S. El-Sayed, K. Mow and F. A. L. Dullien, Flow Through porous media - the Ergun's equation revisited, *Ind. Engng. Chem. Fund.* **18**, 199-208 (1979).

107. M. S. Khader and J. S. Goodling, Effective thermal conductivity of grannular materials in cylindrical beds, *16th Int. Thermal Conductivity Conference*, Chicago, IL, (1979).

108. M. L. Hunt and C. L. Tien, Effects of thermal dispersion on forced convection in fibrous media, *Int. J. Heat Mass Transfer* **31**, 301-309 (1988).

109. J. C. Slattery, *Momentum, Energy and Mass Transfer in Continua* , Kreiger Press, New York (1978).

110. R. G. Carbonell and S. Whitaker, Heat and mass transfer in porous media, in Fundamentals of Transport Phenomena in Porous Media , J. Bear and M. Y. Corapcioglu, eds., *NATO ASI Series* (1984).

111. J. J. Lerou and G. F. Froment, Velocity, temperature and conversion profiles in fixed bed catalytic reactors, *Chem. Engng. Sci.* **32**, 853-861 (1977).

112. J. Price, The distribution of fluid velocities for randomly packed beds of spheres, *Mech. Chem. Engng. Trans., Inst. Engrs.(Australia)* **7**, 7-14 (1968).

113. H. Zhu, Effects of transverse thermal dispersion on fully-developed forced convection in annular and cylindrical packed beds, M. S. Thesis, University of Hawaii at Manoa (1987).

114. C. Y. Wen and L. T. Fan, *Models for Flow Systems and Chemical Reactors* , Marcel Dekker Inc., New York (1975).

115. L. H. S. Roblee, R. M. Baird and J. W. Tiern, Radial porosity variations in packed beds, *A.I.Ch.E. Jl.* **4**, 460-464 (1958).

116. Y. Cai, Forced convection in a packed channel, M.S. Thesis, University of Hawaii at Manoa (1990).

117. W. Aung, Mixed convection in internal flows, *Handbook of Single Phase Forced Convection*, ed. S. Kakac, R. Shah & W. Aung, John-Wiley & Sons, 1-98 (1927).

118. D. Kunii and J. M. Smith, Heat transfer characteristics of porous rocks, *AIChE J.*, **6** No. 1, 71-78 (1960).

119. P. Cheng, Wall effects on fluid flow and heat transfer in porous media, *Proc. 2 nd ASME/JSME Thermal Engng. Joint Conf.*, **2**, 297-303 (1987).

120. P. Cheng, Recent studies of wall effects on fluid flow and heat transfer in packed-sphere beds, *Proc. Indian Congress of Appl. Mech.* (1987).

121. S. M. Kuo and C. L. Tien, Transverse dispersion in packed-sphere beds, *Proc. of the 1988 National Heat Transfer Conference, HTD - 96* **1**, 629-634 (1985).

122. D. L. Koch and J. F. Brady, Dispersion in fixed beds, *J. Fluid Mech.* **154**, 399-427 (1985).

123. V. Prasad and N. Kladias, Non-Darcy natural convection in saturated porous media, *Proc. of the Conference on Convective Heat and Mass Transfer in Porous Media, NATO ASI Series*, 67-116 (1990).

124. E. R. Van Driest, On turbulent flow near a wall, *J. A. S.* **23**, 1007-1036 (1956).

125. W. E. Ranz, Friction and transfer coefficients for single particles and packed beds, *Chem. Engng. Prog.* **48**, 247 (1957).